

17-2-53
P. 106-108

RCA Review

June 1968 Volume 29 No. 2

RADIO CORPORATION OF AMERICA

DAVID SARNOFF, *Chairman of the Board*

ELMER W. ENGSTROM, *Chairman of the Executive Committee of the Board*

ROBERT W. SARNOFF, *President and Chief Executive Officer*

GEORGE E. MORRIS, *Secretary*

ERNEST B. GORIN, *Vice-President and Treasurer*

RCA LABORATORIES

J. HILLIER, *Vice-President*

RCA REVIEW

C. C. FOSTER, *Manager*

R. F. CLAFONE, *Administrator*

PRINTED IN U.S.A.

RCA REVIEW, published quarterly in March, June, September, and December by RCA Laboratories, Radio Corporation of America, Princeton, New Jersey 08540. Entered as second class matter July 3, 1950 under the Act of March 3, 1879. Second-class postage paid at Princeton, New Jersey, and at additional mailing offices. Subscription price in the United States and Canada: one year \$4.00, two years \$7.00, three years \$9.00; in other countries, one year \$4.40, two years \$7.80, three years \$10.20. Single copies up to five years old \$2.00. For copies more than five years old, contact Walter J. Johnson, Inc., 111 Fifth Ave., New York, N. Y. 10003.

JUL 29 1968

RCA REVIEW

a technical journal

Published quarterly by

RCA LABORATORIES

in cooperation with all subsidiaries and divisions of

RADIO CORPORATION OF AMERICA

VOLUME 29

JUNE 1968

NUMBER 2

CONTENTS

	PAGE
R-F Sputtering Processes	149
J. L. VOSSEN AND J. J. O'NEILL, JR.	
Laminated-Ferrite Memories—Review and Evaluation	180
R. SHAHBENDER	
An MOS-Transistor-Driven Laminated-Ferrite Memory	199
I. GORDON, R. L. HARVEY, H. I. MOSS, A. D. ROBBI, J. W. TUSKA, J. T. WALLMARK, AND C. WENTWORTH	
High-Power Frequency Doublers Using Coupled TEM Lines	230
C. SUN	
Multiple-Loop Frequency-Compressive Feedback for Angle-Modulation Detection	252
H. HEINEMANN, A. NEWTON, AND J. FRANKLE	
Double-Stream Interaction in a Thin Semiconductor Layer	270
B. B. ROBINSON AND B. VURAL	
Manipulation of Sculptured Surfaces	281
E. P. HELPERT	
Multispectral Vidicon Camera Study	287
J. J. DISHLER AND D. F. LONGCOY	
RCA Technical Papers	298
Authors	301

© 1968 by Radio Corporation of America
All rights reserved.

RCA REVIEW is regularly abstracted and indexed by *Abstracts of Photographic Science and Engineering Literature*, *Applied Science and Technology Index*, *Bulletin Signalétique des Télécommunications*, *Chemical Abstracts*, *Electronic and Radio Engineer*, *Mathematical Reviews*, and *Science Abstracts* (I.E.E.-Brit.).

RCA REVIEW

BOARD OF EDITORS

Chairman

H. W. LEVERENZ
RCA Laboratories

A. A. BARCO
RCA Laboratories

E. D. BECKEN
RCA Communications, Inc.

G. H. BROWN
Radio Corporation of America

A. L. CONRAD
RCA Service Company

E. W. ENGSTROM
Radio Corporation of America

A. N. GOLDSMITH
Honorary Vice President, RCA

G. B. HERZOG
RCA Laboratories

J. HILLIER
RCA Laboratories

R. S. HOLMES
RCA Medical Electronics

E. C. HUGHES
RCA Electronic Components

E. O. JOHNSON
RCA Electronic Components

H. R. LEWIS
RCA Laboratories

G. F. MAEDEL
RCA Institutes, Inc.

L. S. NERGAARD
RCA Laboratories

H. F. OLSON
RCA Laboratories

K. H. POWERS
RCA Laboratories

J. A. RAJCHMAN
RCA Laboratories

F. D. ROSE
RCA Laboratories

L. A. SHOTLIFF
RCA International Licensing

C. P. SMITH
RCA Laboratories

W. M. WEBSTER
RCA Laboratories

Secretary

C. C. FOSTER
RCA Laboratories

REPLICATION AND TRANSLATION

Original papers published herein may be referenced or abstracted without further authorization provided proper notation concerning authors and source is included. All rights of republication, including translation into foreign languages, are reserved by RCA Review. Requests for republication and translation privileges should be addressed to *The Manager*.

P. 2660

R-F SPUTTERING PROCESSES

BY

J. L. VOSSEN AND J. J. O'NEILL, JR.

RCA Laboratories
Princeton, N. J.

Summary—RF sputtering, which has been found useful as a technique for both film deposition and nonchemical etching of a wide range of materials, is highly dependent upon the configuration of the sputtering equipment. An apparatus was designed after consideration of all aspects of the process—the sputtering mechanism, the r-f discharge, the r-f circuitry, the vacuum system, and the general ease of operation and maintainance.

The system parameters that control deposition rates and etch rates were studied. Based on the results of this study, deposition and etch rates can be controlled within $\pm 2\%$ on a routine basis. In general, metals have the highest sputtering rates, complex crystalline solids have the lowest sputtering rates, and glasses and simple crystalline solids have intermediate sputtering rates. The quality of deposited films depends to a large extent upon the deposition rate. The maximum deposition rates that yield films of high quality range from a few tens of $\text{Å}/\text{min}$ to about a thousand $\text{Å}/\text{min}$, depending upon the material being deposited.

As a deposition process, the main advantage of r-f sputtering is its versatility. In theory, any material can be sputtered using this technique. However, certain phenomena occurring at the target surface and on the substrate may tend to change the stoichiometry of materials. Specifically, crystalline oxides of low chemical bond strength can be reduced chemically by argon discharges. Eighteen different oxides were studied experimentally, resulting in a tabulation that can be used to determine whether chemical reduction will occur in a given material. Changes in stoichiometry can also occur as a result of sublimation from the target and/or substrate when one of the constituents is highly volatile. This has been investigated empirically using the system $\text{Cd}_2\text{Nb}_2\text{O}_{11}$ as a vehicle.

For etching, the main advantages of the r-f sputtering process are (1) any solid material can be etched; (2) etch rates are easily controlled; (3) the technique produces etched patterns with vertical walls to a definition limited only by the mask used. To produce patterns of this type and to retain the original surface character, etch rates similar to the deposition rates cited above must be used.

INTRODUCTION

THE phenomenon of sputtering—the distintegration of a solid surface (target) when struck by ions or atoms in a gas discharge—has been studied for over 100 years. Because of the very complex interactions among the gas-discharge parameters, the target surface, and the mechanical aspects of the process, it is a very

difficult process to study in quantitative detail from a theoretical approach; most of the available information has been empirically obtained.

Sputtering has found practical application both in the deposition of thin films and in nonchemical etching. In the former application the target is the material to be deposited. Material is removed from the target by momentum transfer from discharge ions and is deposited on a substrate elsewhere. In etching, the surface to be etched serves as the target. The use of sputtering in the deposition of metal films has been practiced for many years.

Because high-energy ion beams are relatively easy to produce, ions rather than atoms have generally been used to disintegrate the target surface. Upon striking the target surface, the ion energy is transferred to the surface in the impact region. The basic mechanism of ejection of target surface material is momentum transfer, coupled with other complex, second-order phenomena.^{1,2} Those ions that penetrate the target surface give up their energy by vibrating the lattice (heating) and do not participate in the removal of target material unless the target material is volatile, in which case sublimation can occur.

To a first approximation, therefore, the surface of a target material that is not volatile is uniformly stripped of a layer of material, but the chemical composition of the target surface is unchanged by the ion beam. Films deposited by sputtering generally have the same chemical composition as the target surface. When films are to be deposited, great care must be taken to ensure that the target surface is clean and has the same chemical composition as the bulk material.

The method used to produce the high-energy ions determines, in large measure, the utility of the sputtering process. The simplest and most common method is a two-terminal d-c glow discharge. The Crooke's dark space around the negative terminal of the discharge is a sheath of positive ions and most of the discharge potential appears across this region; as the ions move through this sheath, they acquire a potential nearly equal to the voltage applied across the electrodes. In this configuration the sputtering target is the negative electrode. Clearly the target must be an electrical conductor. Otherwise, a controllable negative potential could not be sustained on the target surface exposed to the discharge. Films of metals, alloys, and some low-band-

¹ G. K. Wehner, "Sputtering by Ion Bombardment," in *Advances in Electronics and Electron Physics*, Vol. VII, pp. 239-298, Academic Press, N. Y. (1955).

² Eric Kay, "Impact Evaporation and Thin Film Growth in a Glow Discharge," in *Advances in Electronics and Electron Physics*, Vol. 17, pp. 245-322, Academic Press, N. Y. (1962).

gap semiconductors can be deposited with inert-gas discharges in this mode.

The material removed from the target surface is in a highly energetic state (2 to 10 eV) and is very prone to chemical reaction and adsorption. Care must be exercised to remove all reactive gases from the system when pure metal deposits are required. On the other hand, certain oxides, nitrides, and some mixtures can be deposited by purposely introducing reactive gases into the system during sputtering (reactive sputtering). This method of producing mixed oxides, nitrides, etc., is limited by the availability of metal targets containing the cations of the desired mixture in the proper proportions.

Limitations associated with two-terminal d-c sputtering include:

1. Deposition rates are generally low because the target-to-substrate separation and the gas pressure cannot simultaneously be kept small if a discharge is to be sustained (Paschen's Law). In other words, for a given voltage, the material emitted from the target must travel through the same number of mean-free-path lengths, regardless of the combination of pressure and separation used.

2. As discussed previously, the purity of the deposited film can be a problem (adsorbed inert gases in metal sputtering and incomplete reaction in reactive sputtering).

3. The versatility of the process is limited in that the target must be a fairly good conductor.

Various solutions for one or more of the problems cited above have been worked out. To increase deposition rates, "supported discharge"^{1,3} sputtering has been used. This system employs four power supplies, however, and contamination is often introduced by hot filaments.^{4,6} An alternative approach for increasing ion density at low pressures is to use a magnetic field normal to the target surface. The magnetic field forces discharged electrons to travel in helical paths, thus increasing the probability of an ionizing collision. Magnetic fields of this type yield higher ion densities for a given voltage and pressure and enable discharges to be sustained at relatively low pressures.

Bias sputtering was used by Maissel and Schaible⁷ to improve

³ J. Nickerson and R. Moseson, "Low Energy Sputtering," *SCP and Solid State Tech.*, Vol. 7, No. 12, p. 33, (1964).

⁴ R. E. Minturn, S. Datz, H. Taylor, "Thermal Emission of Alkali Ion Pulses From Clean and Oxygenated Tungsten," *J. Appl. Phys.* Vol. 31, No. 5, p. 876, (1966).

⁵ H. F. Winters, D. R. Denison, D. G. Bills, and E. E. Donaldson, "Chemical Sputtering of Tungsten at Elevated Temperatures," *J. Appl. Phys.*, Vol. 34, No. 6, p. 1810 (1963).

⁶ D. Lichtman, "Ion Emission From Heated Metal Surfaces," *J. Vac. Sci. & Tech.*, Vol. 2, No. 2, p. 91, (1965).

⁷ L. I. Maissel and P. M. Shaible, "Thin Films Deposited by Bias Sputtering," *J. Appl. Phys.*, Vol. 36, No. 1, p. 237, (1965).

the purity of deposited films. A negative substrate bias generates a Langmuir sheath in the vicinity of the substrate. Low-energy ions (50 to 200 eV) bombard the surface of the substrate during film growth, causing the substrate to be scrubbed and outgassed. In some cases re-sputtering of the film material is observed.

It should be noted that a small Langmuir sheath is always associated with insulating substrates. The magnitude of the ion energy in this sheath depends upon the location of the substrates with respect to the various parts of the discharge and to the intensity of the discharge. This type of sheath is not readily controllable.

If the substrates are positively biased during reactive sputtering, the few negative ions generated in reactive gas discharges are attracted to the substrates and tend to drive the reaction to completion. This is similar to the process of "plasma anodization".⁸

Other methods have been used to improve deposition rates and film purity, but those cited above have been found to be the most controllable.

The use of an r-f discharge for sputtering insulators was suggested by Wehner¹ in 1955. He reasoned that the positive space charge accumulated during one half cycle could be neutralized by discharge electrons during the other half cycle. Anderson et al.⁹ used r-f sputtering for cleaning, etching, and sputtering of insulators. Davidse and Maisel¹⁰ reported on the process from the viewpoint of the deposited film and its properties as opposed to the mechanism of the process.

RF sputtering is a process by which, in theory, films of *any* material can be deposited. This versatility is the major advantage of the process, and differentiates it from nearly all other methods of deposition. The original use of the process as a universal, nonchemical etching technique⁹ is another major area of application.

This versatility is not achieved without drawbacks. The process is quite complicated. It has all of the complexities of d-c sputtering plus a few more because of the power source employed.

It is our purpose to review the practical aspects of r-f sputtering. The design of r-f sputtering equipment represents a complex compromise that must be reached by considering all aspects of the process: the sputtering mechanism, the discharge, the r-f circuitry, the vacuum

⁸ J. L. Miles and P. H. Smith, "The Formation of Metal Oxide Films Using Gaseous and Solid Electrolytes," *J. Electrochem. Soc.*, Vol. 110, No. 12, p. 1240 (1963).

⁹ G. S. Anderson, W. N. Mayer and G. K. Wehner, "Sputtering of Dielectrics by High Frequency Fields," *J. Appl. Phys.*, Vol. 33, No. 10, p. 2991, (1962).

¹⁰ P. D. Davidse and L. I. Maisel, "Dielectric Thin Films Through rf Sputtering," *J. Appl. Phys.*, Vol. 37, No. 2, p. 574, (1966).

system, and the many details usually lumped under the heading human engineering. Other problems to be considered are the deposition-rate-controlling variables, sublimation of volatile species, decomposition of crystalline oxides, and the use of r-f sputtering as a nonchemical etch.

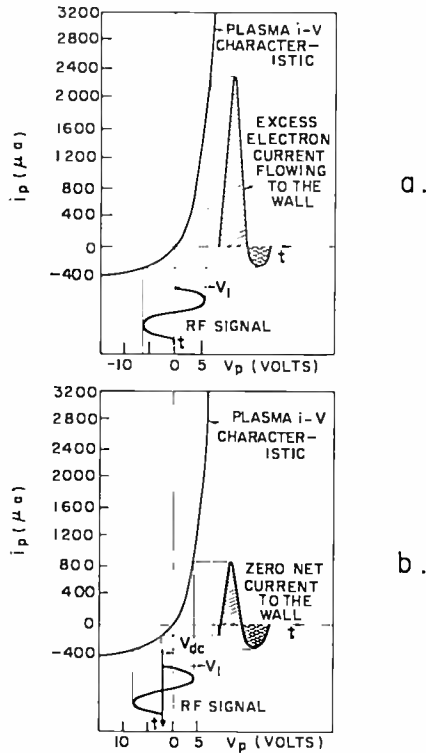


Fig. 1—Mechanism of sheath formation in an r-f discharge. (After Butler and Kino, Ref. (11))

THE R-F GLOW DISCHARGE AND SHEATH FORMATION

The exact mechanism of sheath formation in an r-f discharge was proposed by Butler and Kino¹¹ for the general case and extended by Anderson et al.⁹ to the case of sputtering. To obtain a high positive ion flux to a target in r-f sputtering, the target surface exposed to the discharge must be at a high negative potential. The source of this negative potential is the interaction of the applied r-f field and the I - V characteristic of a solid surface in a plasma (see Figure 1).

¹¹ H. S. Butler and G. S. Kino, "Plasma Sheath Formation by Radio Frequency Fields," *Phys. Fluids*, Vol. 6, No. 9, p. 1346 (1963).

When a time-varying potential is applied to a metal plate behind the target, another time-varying potential is developed on the opposite target surface through the impedance of the target. Once the gas has broken down, starting a discharge, a current flows from the plasma to the target surface. The magnitude of this current is determined by the I - V characteristics of the plasma (Figure 1a). Since the electrons in a plasma have a much higher random speed than the ions, the electron current to the target surface is initially much greater than the ion current. The surface will therefore receive a negative charge until its potential is sufficiently lowered that the net charge arriving at the surface is zero (Figure 1b).

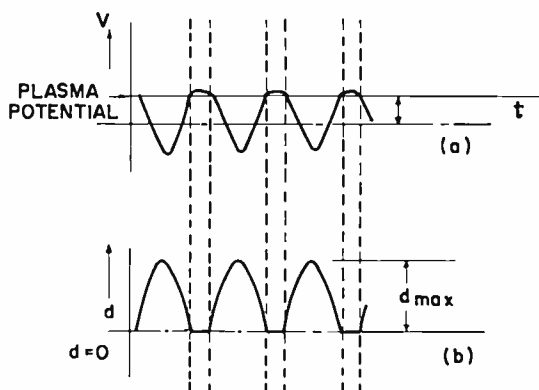


Fig. 2—(A) Target surface potential versus time and (B) ion sheath thickness versus time. (After Anderson et al, Ref. (9))

If the d-c potential of the target surface were to remain constant and the a-c potential were to vary in the plasma with time, an excess of electron current would always be flowing to the target surface. Since no charge can flow through the target, the net d-c current to the target must be zero. This implies that the target surface potential can become, at most, slightly positive and must have a peak negative value that is nearly as large as the peak-to-peak amplitude of the applied potential.

The resulting time-varying target potential is illustrated in Figure 2a. Since the target potential is negative with respect to the plasma, electrons are forced away from the surface, yielding an ion sheath that is visible as a dark space near the target surface. The thickness of this ion sheath varies with the surface potential of the target (Figure 2b). Ions from the sheath are drawn toward the target by the negative potential with an approximately sinusoidal energy distribu-

tion, the average of which is slightly less than the peak signal applied. The waveform is slightly clipped.¹¹

To minimize the slight positive target potential shown in Figure 1b (i.e., to prevent excessive positive charge accumulation at the target surface), the frequency of the applied voltage must be high. Anderson et al⁹ have shown that the frequency must be at least 10^6 Hz for any appreciable sputtering to occur. Below this frequency, the average energy of the ions is reduced significantly as a result of positive ion accumulation at the target. This accumulation occurs because the ions

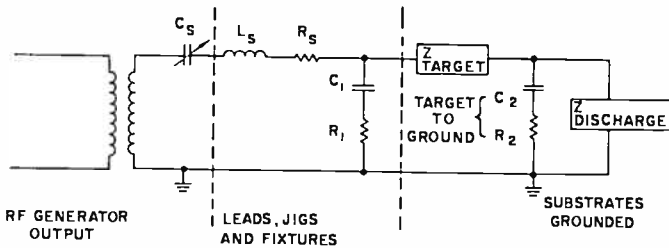


Fig. 3—Equivalent circuit of an r-f sputtering system.

are able to follow the applied signal better as the frequency is decreased, i.e., the I - V characteristic in Figure 1 becomes more linear. From the standpoint of charge accumulation, therefore, the frequency should be as high as possible.* There are, however, other considerations to be discussed that dictate the use of low frequencies.

From the above discussion, it is evident that the sheath produced in r-f sputtering is a high-potential Langmuir sheath, and may be treated accordingly.

EQUIPMENT AND CONFIGURATION OF R-F SPUTTERING APPARATUS

The design of an r-f sputtering system requires as much attention to the system impedances as to the nature of the discharge. There are numerous permutations and combinations that can change system impedances. Basically, however, all systems can be represented by an equivalent circuit similar to the one shown in Figure 3. Here we assume a transformer-coupled r-f generator and grounded substrates. For maximum power transfer from generator to load, the stray resist-

* The frequency cannot extend into the microwave region, however, since the plasma I - V characteristics of Figure 1 do not apply in this range.¹²

¹² F. F. Chen, "Electric Probes," in *Plasma Diagnostic Techniques*, Ed. by Huddleston and Leonard, pp. 113-200, Academic Press, N. Y. (1965).

ances, capacitances, and inductances should be minimized. Even more importantly, these parameters, once minimized, must be kept constant so that the electrical parameters of the discharge can be controlled accurately.

A. The R-F Generator

Almost any r-f generator is suitable for sputtering. In all cases, the generator must include an impedance-matching network so that the system can be tuned to resonance, thus allowing maximum power transfer to the discharge. A double-tuned transformer-coupled output is helpful because it can be slightly over-critically coupled. This slight over-coupling results in a resonant characteristic curve that is rather broad and flat-topped at the peak. By tuning the generator to the center of this peak, the power delivered to the load remains constant, even if some of the stray parameters in the system change a little due to heating.

Many coupling techniques can be used.^{13,14} If metals are to be sputtered, a series capacitor must be included in the secondary (C_s in Figure 3) to satisfy the sheath criterion calling for no d-c current flow in the target leg of the circuit. In the system shown, C_s is a variable capacitor (25-500 picoforads) and is part of the coupling network. For dielectric targets, C_s need not be included if other coupling means are employed.

As mentioned previously, as high a frequency as possible would be desired if the discharge mechanism were the only consideration. For dielectric targets, a high frequency is also desirable to minimize the series capacitive reactance of the target. However, minimization of the attenuating effects of L_s , R_s , C_1 and R_1 , beyond what is possible by mechanical means alone, requires that the operating frequency be low. With a given vacuum system and target configuration, it is not possible to reduce these attenuating effects below a certain level. Furthermore, as the frequency is increased, adequate ground returns become very difficult to make.

A good compromise frequency range is between 10 and 20 MHz. Within this range, 13.560 MHz is the only frequency allocated by the Federal Communications Commission to industrial-scientific-medical purposes. If the generator is locked to this frequency, the equip-

¹³ F. E. Terman, *Radio Engineer's Handbook*, pp. 148-164, McGraw-Hill Book Co., N. Y. (1943).

¹⁴ D. J. Healy and M. Lauriente, "Impedance Matching Network for rf Sputtering Systems," paper presented at the 13th National Symposium of the American Vacuum Society, San Francisco, California (1966).

ment can be certified for compliance with FCC regulations rather easily.¹⁵ For truly optimized performance, it is preferable to have a variable-frequency generator so that the best frequency for any given system can be used. The price paid for this advantage is the added difficulty in obtaining certification of compliance with FCC rules and regulations on radio interference.¹⁵

The required power output level of the generator depends upon the size of the target and the losses in the system. The net current density in the discharge ranges from 1 to 4 milliamperes/cm². The generator must be able to supply this power plus whatever is needed to overcome losses in the leads, jigs, and fixtures.

B. Leads, Jigs, and Fixtures

After trying out several different lead geometries, we have concluded that the best is a rigid, air-dielectric coaxial system flanged to the generator housing (which is earth grounded) and to the base plate of the vacuum system. The inner conductor should be of substantial diameter and short length to minimize inductance and resistance. A one-inch-diameter, brass, center conductor was found adequate for power levels up to 3000 watts and frequencies up to 20 MHz. The outer conductor (shield) should have as large an inner diameter and as thick a wall as space will allow. This minimizes the series resistance and inductance and the shunt capacitance C_1 . Large-area flanges should be used throughout to minimize these stray parameters and to enhance the ground return.

The importance of good ground returns cannot be over-emphasized. In r-f power circuits, two points that are very close together physically, are not really at the same potential, even when connected by a substantial conductor, because of the inductance in the connection.

Solid dielectric coaxial cable, even of large size, has been shown to be a poor lead system. The power losses due to r-f heating of the cable are variable and uncontrolled unless the cable is terminated with an impedance-matching network. The physical size of such a network is so large as to make this arrangement undesirable in sputtering equipment.

Similarly, the loss tangent of the dielectrics used as insulation on r-f vacuum feedthroughs must be considered. Most commercial r-f feedthroughs are designed to be water cooled, which may or may not be necessary for a given application, depending upon the power levels. If water cooling of the system can be avoided, the electrical and mechani-

¹⁵ Federal Communications Commission Rules and Regulations, Part 18, Industrial, Scientific and Medical Equipment, Jan., 1964.

cal simplicity of the system is greatly enhanced. We have found that water cooling of the target is not necessary up to discharge power levels of 3000 watts.

Most commercially available r-f feedthroughs are geometrically and mechanically unsuitable for sputtering. We have found that an ambient-cooled r-f feedthrough with glazed porcelain insulators is suitable for power levels up to 3000 watts and frequencies up to 20 MHz.

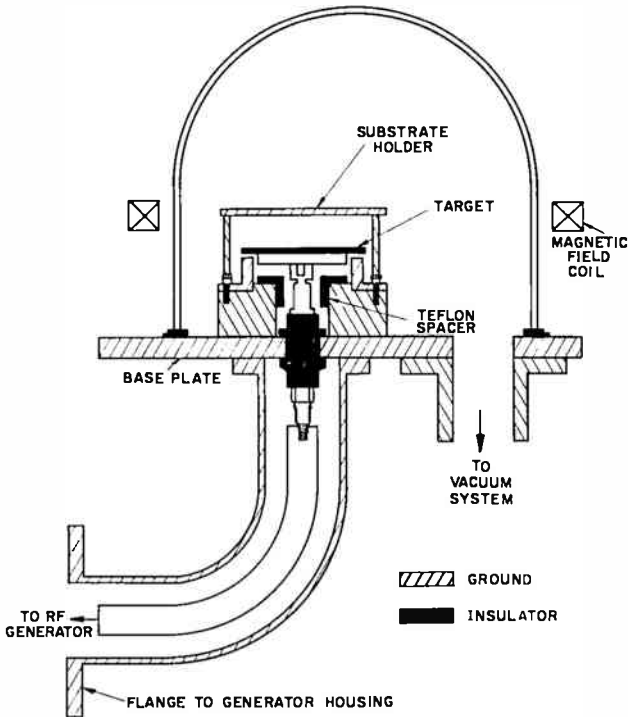


Fig. 4—Cross section of the r-f sputtering system.

Figure 4 is a cross-sectional view of a system found to be quite satisfactory for targets up to 4 inches in diameter. A metal target support is screwed directly into the top of the feedthrough and a massive coaxial shield is used to suppress the discharge below the target. This system can be scaled up to larger target diameters (Figure 5) or down to small diameters (Figure 6).

To accommodate the massive shields both inside and outside of the vacuum system and to have the target nearly concentric with the magnetic field coil (Figure 4), the pumping port is eccentric and the base

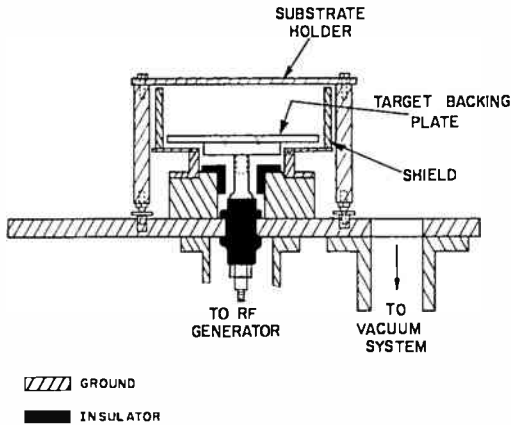


Fig. 5—R-F sputtering system scaled-up for larger targets

plate cantilevered off the port, leaving free access to the center of the base plate.

Inside the vacuum system, the previous consideration of separation between center conductor and outer ground (shield) no longer applies. Inside the system, the ground shield must be close enough to the center conductor to suppress any discharges below the target, but must be large enough to minimize the capacitance. Fortunately, the higher rates of deposition occur at pressures less than 10-15 millitorrs, a pressure range where discharges are not maintained for small separations.¹⁰ We have found that a separation of approximately 0.25 inch is adequate to suppress the discharge up to 0.04 Torr. This small physical separation can be achieved, while keeping the capacitance at a mini-

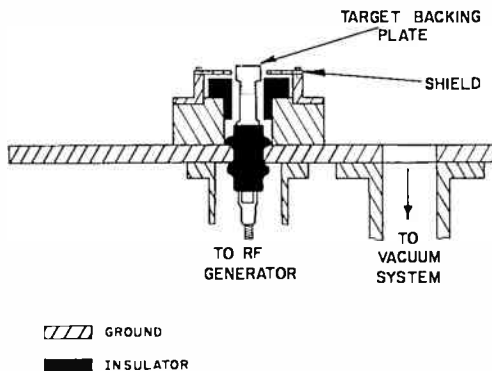


Fig. 6—R-F sputtering system scaled-down for smaller targets.

imum, through the use of an insulating spacer on the ground shield, as shown in Figure 4. Teflon* is found satisfactory for this service up to 1500 watts, because of its low dielectric constant and machinability. Above this power level, the Teflon spacer begins to decompose. The massive ground shield provides both a good ground return and good heat sinking.

The configuration of the whole sputtering apparatus is coaxial and cylindrical throughout. Sharp corners and rectangular geometries should be avoided to eliminate the high field concentrations at corners that result in overheating, nonuniform discharges, and other undesirable effects. For the same reason, if the target surface is lower than, or planar with the top of the ground shield, the discharge covers only a portion of the target surface. This results in nonuniform target disintegration, nonuniform target heating, cracking of brittle targets, and nonuniform film thickness on the substrate due to ground-shield focusing of the discharge.

C. *The Vacuum System*

The vacuum system must have a high pumping speed for all gases used. If oxygen discharges are used in an oil system (diffusion and mechanical pumps), both pumps must be suitable for pumping oxygen. Silicone oil is satisfactory for diffusion pumps. Mechanical pumps require oxidation-resistant oil and special seals. Pump explosions can result if these precautions are not taken.

D. *The Target*

The impedance of the target should be as low as possible. Therefore, regardless of the material, the target should have the maximum possible area-to-thickness ratio consistent with the mechanical requirements (i.e., rigidity, flatness, etc.). All edges of the target exposed to the discharge should be rounded to prevent high field concentrations at sharp corners. Also, the contact resistance of the target to its support should be minimized. The back surface of dielectric targets should at least be metallized, and it is better to solder the target to the support plate.

If the impedance of the target is high, not only is the discharge current limited, but the electrical conditions are difficult to control because of the temperature coefficient of target impedance and because of r-f heating of the target. The power loss in watts per unit volume

* Registered trademark of E. I. Du Pont De Nemours & Co.

for dielectric targets is given by

$$L = \epsilon_0 \omega \mathcal{E}^2 K \tan \delta, \quad (1)$$

where ϵ_0 is the permittivity of free space (8.85×10^{-12} farad/meter), ω is the angular frequency, \mathcal{E} is the electric field across the volume, K is the relative dielectric constant of the target, and $\tan \delta$ is the dissipation factor of the target. It is evident that the important parameter to minimize is the electric field across the target, which is best done by keeping the target impedance low. There are other obvious compromises. In the case of polycrystalline, ceramic targets, it is particularly important to minimize r-f heating to prevent cracking of the target. How low the target impedance should be depends upon the parallel combination of C_2 , R_2 and the discharge impedance. The ratio of target impedance to the total impedance determines the voltage drop across the target.

E. Target Surface-to-Ground Impedance and Substrate Supports

The impedance from the surface of the target (the surface exposed to the discharge) to ground (C_2 and R_2 in Figure 3) is an operating variable, i.e., it varies with the target-to-substrate separation and the surface area of metal on the substrate support.

The substrate support shown in Figure 4 is an aluminum plate on four conducting pillars. These are terminated at the lower end with banana plugs inserted into the ground shield. This method of substrate grounding has proved adequate and is quite flexible, since the support can be removed and replaced easily. The same arrangement can be used for larger targets and larger substrate supports, except that the legs for the support must be more substantial since the distance from substrate to ground is larger. In the configuration shown in Figure 5, the substrates are above the target. This simplifies mechanical design, but has the obvious disadvantage that the total substrate surface cannot be coated owing to the necessity for supporting the edges of the substrate. However, this arrangement allows for ease in changing targets and for converting the system to r-f sputter etching. It also eliminates problems associated with supporting large targets against gravity.

One of the assumptions made here is that the substrates are maintained at ground potential. This is the usual configuration and the one that results in the highest deposition rate. We have also investigated the effect of isolating the substrates from ground by using glazed steatite legs on the substrate platform. The substrate platform is then

capacitively coupled to ground, as shown in Figure 7 (C_3). In this case, the discharge is partly from target to substrate and partly from substrate to ground. The exact proportions are determined by the ratio of C_2 to C_3 . This configuration has been used to test the importance of substrate grounding in terms of deposition rate. It can also be used to isolate the substrates from the massive heat sink, permitting the discharge to heat the substrates. Removal of the substrates from electrical ground increases the potential of the Langmuir sheath in the vicinity of the substrates and makes this sheath uniform regardless of the ratio of metal area to open area on the substrate platform.

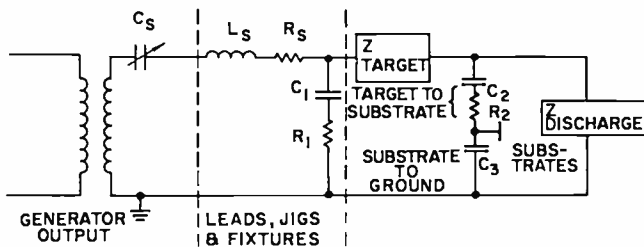


Fig. 7—Equivalent circuit of the r-f sputtering system with the substrates isolated from ground.

F. Measurement of R-F Voltage, Current, and Power

The measurement of r-f current is usually performed in the r-f generator by means of a thermocouple-type r-f ammeter. It would be preferable to measure the current in the discharge directly, but the various techniques for doing this are insensitive in the range of currents of interest, and complicate the apparatus considerably.¹⁶ By measuring the current at the generator terminals and utilizing known values for the impedances in the system, one can calculate the discharge current approximately.

The measurement of r-f voltage can be accomplished just below the target with a probe capacitive voltage divider. The measured voltage is the sum of the voltages across the target and the discharge. The electrical circuit and mechanical construction of a simple r-f kilovoltmeter are shown in Figure 8. The VTVM can be calibrated (with the vacuum system open) by comparing its readings with those of a calibrated oscilloscope.

¹⁶ S. L. Leonard, "Basic Macroscopic Measurements," in *Plasma Diagnostic Techniques*, See Ref. (12), pp. 8-67.

From the discharge voltage and current, as measured or calculated above, one can determine the r-f power delivered to the discharge. An r-f power meter can also be used. R-F power meters that indicate both transmitted and reflected power are especially useful in matching the generator to the load.

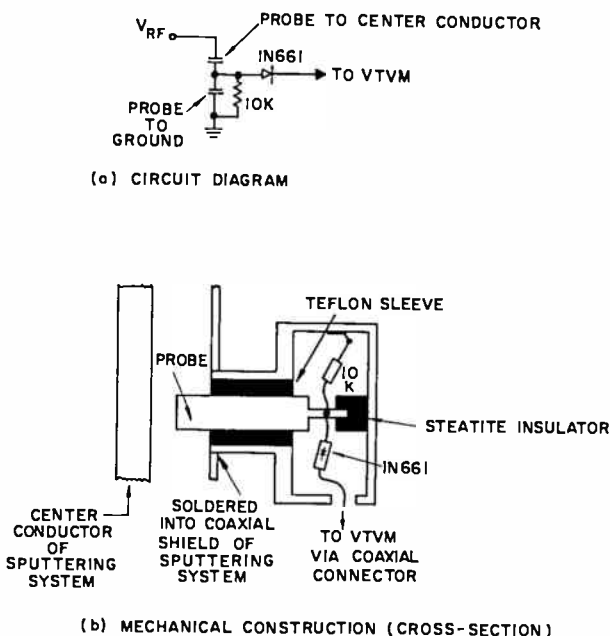


Fig. 8—R-F kilovoltmeter circuit and construction.

ELECTRICAL CHARACTERISTICS OF THE DISCHARGE

Because of the complexity of the sputtering system, it is difficult to determine accurately the impedance of the discharge. The discharge may be represented as a series resistor-capacitor combination. The reactive part of its impedance is capacitive as evidenced by a downward shift in frequency upon breakdown of the gas. An estimate of this capacitance has been made for the system shown in Figure 4 (accurate measurements of the stray parameters of this system have been made.) For an argon discharge, the capacitance decreases linearly with current density from approximately 10,000 pF at 0.5 milliamperes/cm² to 2000 pF at 4 milliamperes/cm². The resistance increases from approximately 1000 ohms at 0.5 milliamperes/cm² to 2000 ohms at 4 milliamperes/cm². The resistance is the dominant part of the impedance in

the frequency range of interest. These estimates were made for a discharge at a pressure of approximately 8×10^{-3} Torr with a 3-inch-diameter metal target. The results obtained by Benson and Bradshaw¹⁷ at higher pressure have been extrapolated to lower pressures and are found to be in reasonable agreement with our data.

A more precise determination could probably be obtained by constructing a small tube, simulating r-f sputtering conditions, and then measuring the impedance directly in this more convenient geometry.

TARGET MATERIALS

The relation between the deposition rate and the target material is a study in itself. We shall not detail the particular properties of various target materials here. Rather, some general comments applicable to all materials will be made. When speaking of targets in this context, we really refer to the target *surface*, since it is from the surface that material is emitted. The exact mechanism by which material is emitted varies somewhat depending on the target material.¹

It is fairly well established that momentum transfer from fast-moving positive ions attracted from the discharge toward the target surface causes disintegration of the target surface, i.e., rupture of surface bonds. The elastic constants of the target and the strength of the atomic or molecular bonds in the target material are the important parameters.

Elemental metals have the highest r-f sputtering rates. The deposition rates for metal alloys are somewhat lower than for their constituent metals.

We have found to date that insulators should be grouped into three classes: (1) simple crystalline solids (e.g., SiO_2 , Al_2O_3), (2) multi-compound crystalline solids (e.g., BaTiO_3 , $2\text{CdO} \cdot \text{Nb}_2\text{O}_5$), and (3) noncrystalline solids (e.g., glasses). Of these classes, noncrystalline solids have the highest deposition rates and multi-compound crystalline solids have the lowest deposition rates. There are exceptions, notably, SiO_2 , which has a higher deposition rate than any glass sputtered to date.

Glasses, as deposited, are stoichiometrically identical to the target material, but usually are poorly structured. The films are undensified and the bond angles are not the same as in the target material. This is evidenced by a higher etch rate for films than for the bulk glass, and the fact that heat treatment of films (usually at or near the soften-

¹⁷ F. A. Benson and M. W. Bradshaw, "Impedance/Frequency Characteristics of Glow Discharges," *Proc. I.E.E.*, Vol. 113, No. 1, p. 62, (1966).

ing point of the glass) leads to films having infrared absorption and reflection spectra identical to the bulk material. This observation is also characteristic of other deposition techniques, such as chemical vapor deposition.

Great care must be taken to ensure that the glass surface is representative of the bulk. This is especially true of glasses containing B_2O_3 . Boron oxide is quite volatile and can be sublimed from the target surface by fire-polishing, high-temperature metallizing, and other heat treatments. After target metallization, it is good practice to lap the target surface back to expose virgin glass for sputtering. Chemical etching of the surface should be avoided, since some components are often leached out in this process, changing the surface composition.

Some of the same problems exist with simple crystalline solids. Films are found not to have their theoretical density and are usually amorphous as deposited. Again heating, either during or after deposition, corrects these deficiencies.^{18,19} Heating of the substrate during deposition reduces the deposition rate, particularly for volatile materials. The energy of the sputtered species upon arrival at the substrate is quite high, causing the substrate temperature to rise. If, in addition, the substrate is heated, sublimation from the substrate may occur, lowering the net deposition rate. In some instances, volatile species in or on the substrate itself have the same effect.

Certain crystalline oxide targets are found to be reduced chemically when sputtered in argon discharges. It is important to know which oxides reduce and which do not, so that one can decide whether to add oxygen to the discharge to minimize or prevent reduction of the target and film.

It is difficult, without direct experimental verification, to compile a list of oxides in order of their ease of reduction. First, the degree of reduction (i.e., how many oxygen atoms are removed from the molecule) is unknown in most cases. If partial reduction occurs, there is little or no thermodynamic data available for these partially reduced forms. Free energies of dissociation are generally available^{20,21} only

¹⁸ M. H. Francombe, "Growth Phenomena in the Formation of Dielectric Films by Sputtering," Meeting of the Electrochemical Society, May 9, 1967, Dallas, Texas.

¹⁹ M. H. Francombe, A. J. Noreika and S. A. Zeitman, "Recrystallization and Phase Transformations in Oxide Thin Films," *Extended Abstracts, 13th National Vacuum Symposium (American Vacuum Society)*, 1966, San Francisco, California.

²⁰ J. P. Coughlin, *Contributions to the Data on Theoretical Metallurgy, XII. Heats and Free Energies of Formation of Inorganic Oxides*, U. S. Bureau of Mines Bulletin No. 452, Washington, D. C. (1954).

²¹ J. A. Gibson, J. F. Miller, P. S. Kennedy and G. W. P. Rengstorff, *Compilation of the Properties of Rare Earth Metals and Compounds*, Battelle Memorial Institute, Columbus, Ohio (1959).

to complete dissociation of the form



In some cases, a change in state of the cation is involved, which is often not detectable. For example, in the dissociation of CdO, there are three values for the free energy change depending upon whether the Cd is solid, liquid, or gas. It is possible for any or all of these states to exist in the sputtering environment, thus making an estimate of the change virtually impossible.

Another method for compiling a list of oxides in order of their ease of reduction is to use the strength of the chemical bond as the determining factor. Extensive data on bond strengths are available only for diatomic molecules.²² These bond strengths are not equal to mean bond energies calculated from heats of formation of molecules. However, in the absence of bond-strength data on polyatomic molecules, the average heat of formation per oxygen atom is used as a guide to bond strength (Table I). The standard heat of formation per bond is multiplied by the number of bonds for each oxygen atom in the crystal to arrive at the average energy required to remove one oxygen atom from the structure. The standard heats of formation per bond were taken from References (21) and (23). The number of bonds per oxygen atom were taken from Wyckoff.²⁴

The bond strength of the diatomic molecule formed from the same cation and oxygen is also listed for each molecule. This number is the energy required to remove the last oxygen from the molecule (in the case of a polyatomic molecule). By comparing this with the "average" energy per oxygen atom, it is often possible to predict whether dissociation will be complete or partial. These data are taken from the compilation of Kerr and Trotman-Dickenson.²²

Despite the questionable nature of this method of listing, it has proven consistent in practice. At a discharge voltage level of approximately 3600 volts (peak-to-peak), molecules up to ZrO_2 are found to reduce at least partially. All of those oxides having dissociation energies higher than that of SrO did not reduce.* The oxides that have

²² J. A. Kerr and A. F. Trotman-Dickenson, "Strengths of Chemical Bonds," in *Handbook of Chemistry and Physics*, Edited by R. C. Weast, 47th Ed., pp. F-130-136, Chemical Rubber Publishing Co. (1966-67).

²³ R. T. Sanderson, *Chemical Periodicity*, Reinhold Publishing Corp., N. Y. (1960).

²⁴ R. W. G. Wyckoff, *Crystal Structures*, 2nd Ed., Vols. 1-3, Interscience Publishers, N. Y. (1965).

* It should be noted that the chemical reduction referred to here is a gross effect. It is highly probable that the oxides having higher heats of dissociation are still reduced to some extent during sputtering in argon.

Table I—Oxides in Order of Approximate
Dissociation Energy Per Oxygen Atom

Molecule	Heat of Dissociation/ Bond kcal/mole	Heat of Dissociation/ Oxygen Atom kcal/mole	Chemical Bond Strength of Diatomic Molecule of the Same Cation and Oxygen kcal/mole
HgO	10.8	21.6	—
SeO ₂	13.75	27.50	101
*PbO ₂	16.56	33.06	99
TeO ₂	19.42	38.84	64
*Bi ₂ O ₃	23.0	46.0	86
As ₂ O ₃	26.0	52.0	114
*PbO	26.1	52.2	99
*CoO	28.6	57.2	—
*NiO	29.2	58.4	—
Sb ₂ O ₃	29.5	59.0	75
*CdO	30.43	60.86	89
Fe ₂ O ₃	32.1	64.2	98
Fe ₃ O ₄	33.4	66.8	98
WO ₃	33.47	66.84	155
*SnO ₂	34.7	69.4	133
P ₂ O ₅	36.0	72.0	144
*V ₂ O ₅	37.3	74.6	149
ZnO	41.59	83.18	93
K ₂ O	43.2	86.4	—
*Cr ₂ O ₃	44.9	89.8	102
MnO	46.0	92.0	97
*Nb ₂ O ₅	46.32	92.64	93
GeO ₂	32.1	96.3	159
Na ₂ O	49.1	99.4	—
Ta ₂ O ₅	50.0	100.0	195
*TiO ₂	54.5	109.0	157
In ₂ O ₃	37.1	111.3	26
CeO ₂	61.25	122.5	186
Ga ₂ O ₃	43.4	129.0	59
*ZrO ₂	64.6	129.2	151
*BaO	66.7	133.4	133
HfO ₂	67.9	135.8	—
Y ₂ O ₃	70.0	140.0	170
*SrO	70.6	141.2	112
Li ₂ O	71.2	142.4	84
Sm ₂ O ₃	71.6	143.2	—
MgO	71.92	143.84	94
Nd ₂ O ₃	72.0	144.0	167
BeO	73.0	146.0	107
Pr ₂ O ₃	73.25	146.5	172
B ₂ O ₃	50.3	150.9	173
*CaO	75.9	151.8	116
*La ₂ O ₃	76.3	152.5	187
*SiO ₂	51.3	153.9	192
*Al ₂ O ₃	65.3	195.9	120

* Experimentally investigated oxides.

been investigated experimentally were dry-pressed and sintered disks, and are noted in the table by an asterisk.

It is of interest to note that there is no oxide with a heat of dissociation *per bond* greater than the heat of dissociation *per oxygen atom* of ZrO_2 . This implies that no oxide can be sputtered under the above conditions without breaking some bonds, resulting in crystallographic distortions both at the target surface and in deposited films. Comparative x-ray fluorescence and diffraction of target surfaces do not show this effect, but the x-ray penetration depth (approximately 20 microns) may be too deep to observe the effect.

Table II—Cd/Nb Ratio of Sputtered $Cd_xNb_2O_{7+x}$ Films
(Original Target Ratio = 1)

Time of Target Usage Hours	Cd/Nb Ratio of Films
1	0.96
10	0.70
100	0.50

Multicomponent crystalline materials combine all of the problems cited above. Many materials have at least one volatile constituent, and this results in a problem of control of stoichiometry both at the target and at the substrate. As an example, the system $Cd_xNb_2O_{7+x}$ has been investigated. Although x-ray fluorescence and diffraction analysis of the target surface showed no crystallographic or stoichiometric changes with time of target usage, wet-chemical analysis of deposited films indicated a decrease in Cd content with time of target usage. This is illustrated in Table II. The particular target used for this investigation was a 3-inch-diameter dry-pressed and sintered ceramic. The discharge gas was O_2 . The peak-to-peak r-f voltage was 2500 volts.

To deposit stoichiometric $Cd_2Nb_2O_7$, it was found necessary to use a composite target consisting of an Nb_2O_5 plate with small CdO disks placed on it in a regular array. The film composition in this case depends upon the ratio of exposed surface areas for the two materials, the thickness of the CdO pellets, etc.

VARIABLES CONTROLLING DEPOSITION RATE

Numerous sputtering variables affect the deposition rate of materials. These are the target material (as discussed above), the sputtering gas(es), the pressure, the electrical parameters of the discharge

(including the quality of the ground), the magnetic field, the target-to-substrate separation, and the target area. Not all of these variables are independent of one another, as will be shown.

To eliminate the complications added by the target material, all of the data that follow are for SiO_2 . There are no gross material complications with this oxide and its use as a reference material (for studying deposition-rate-controlling variables) considerably simplifies the discussion. The data following were taken with the system described above and using a 3-inch-diameter target, unless otherwise specified.

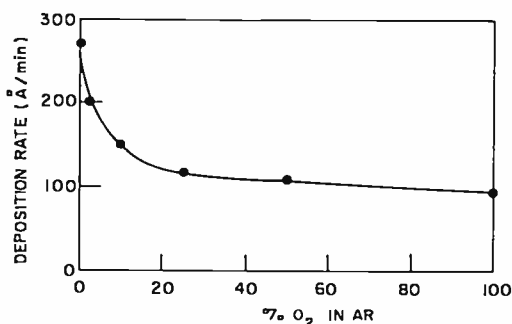


Fig. 9—Deposition rate of SiO_2 versus volume percent of oxygen in an argon discharge.

A. The Discharge Gas and Gas Pressure

Because of its availability in high-purity form, its high atomic weight, and its inertness, argon is ordinarily used for sputtering. The noble gases yield sputtering rates directly proportional to their atomic weights.

Reactive gases behave altogether differently. With oxygen, for example, energy must first be expended to break down the O_2 molecule; then the atoms must be positively ionized by stripping an electron from an atom having a high electron affinity. Thus, a great deal of energy is required simply to support a discharge, and less energy is available to the positive ions for impacting the target and sputtering than is available to noble gas ions under equivalent conditions.

Deposition rates in pure oxygen are generally about half the rates in argon. Figure 9 shows the effect on the deposition rate of various partial pressures of O_2 in Ar. This curve may be compared with similar data reported by Davidse and Maissel.¹⁰

Regardless of the sputtering gas used, the deposition rate is constant from about 2×10^{-3} to 15×10^{-3} Torr and then falls off rapidly

above this range (Figure 10). Ion density increases with pressure, but the mean free path of the emitted species decreases with pressure. In the range of constant deposition rate, these opposing factors cancel each other.

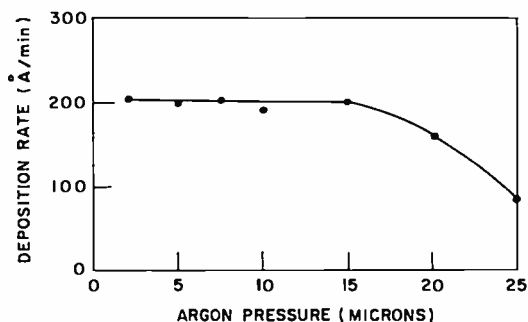


Fig. 10—Deposition rate of SiO_2 versus argon pressure.

B. The Effect of a Magnetic Field

A magnetic field normal to the surface of the target has a number of effects. First, the electrons in the discharge are constrained to follow a helical path, the radius of which is given by

$$r = \frac{m_e v \sin \phi}{e B}, \quad (2)$$

where m_e is the electronic mass, v is the electronic velocity, e is the electronic charge, ϕ is the angle of emission of the electron, and B is the magnetic flux density. Both v and ϕ have a wide distribution in an r-f discharge, resulting in a range of radii. The net effect, however, is to lengthen the electron path, thus increasing the probability of ionizing collisions and, hence, yielding a higher ion density. The higher ion density results in a higher deposition rate (Figure 11). The higher magnetic field also allows one to sustain discharges at lower pressures and for small target-to-substrate separations. Finally, the turbulence added to the discharge improves the uniformity of film thickness over large substrate areas, probably by scattering the emitted species slightly.

The highest deposition rates and the best thickness uniformity are achieved when the substrate and field-coil center lines are the same (see Figure 4). A Helmholtz pair yields slightly improved uniformity of films over the single-coil configuration.

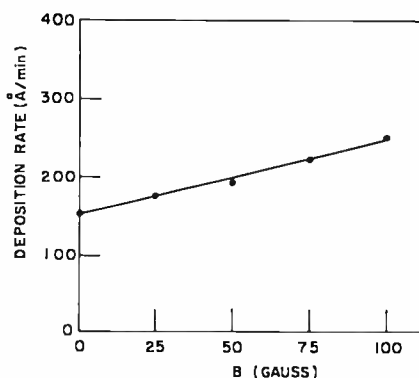


Fig. 11—Deposition rate of SiO_2 versus magnetic flux density.

C. R-F Voltage, Current, and Power

The relationships between the deposition rate and r-f voltage, current, and power are shown in Figure 12. The voltages, currents, and powers indicated are values calculated for the discharge itself; they do not include the losses in the rest of the system. It is evident that rms power in the resonant tuned condition is the simplest and easiest parameter to monitor for purposes of process control.

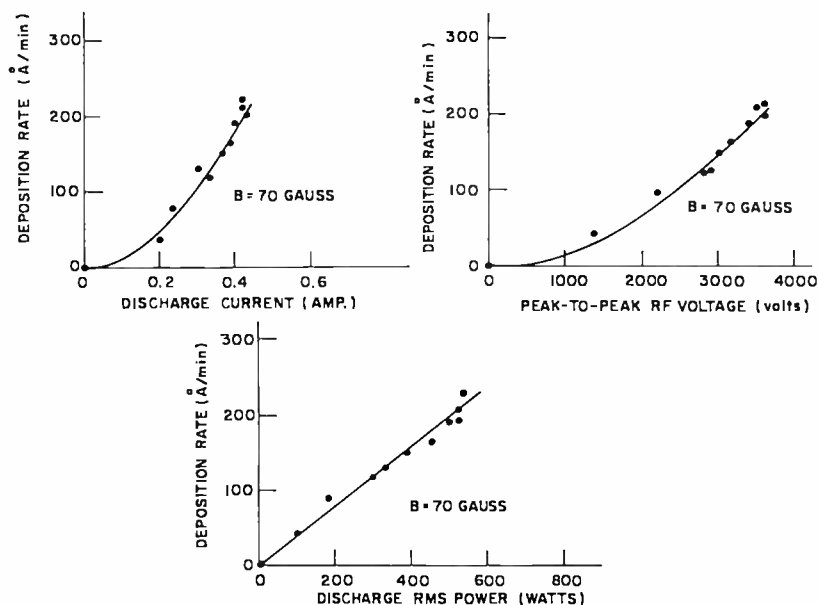


Fig. 12—Deposition rate of SiO_2 versus discharge electrical parameters: discharge current, discharge voltage, and discharge power.

D. Target-to-Substrate Separation

The relationship between deposition rate and target-to-substrate separation is approximately linear in the useful range of separations (Figure 13). Clearly, the separation cannot be less than, or even equal to, the sheath thickness (approximately 1 cm), or no discharge will be initiated or sustained. It is possible to support a discharge at 1.5×10^{-2} Torr down to a separation of about 2.2 cm, but it is not easy to control. A reasonable separation for most work is about 2.5 to 3.0 cm, which allows easy control of the discharge parameters even when reactive gases are used.

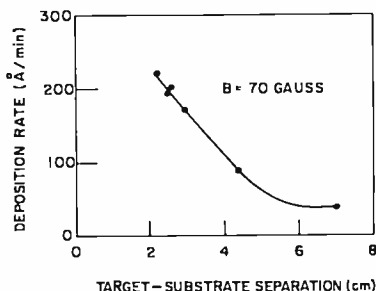


Fig. 13—Deposition rate of SiO_2 versus target-substrate separation.

E. Target Area

The deposition rate as a function of target area follows a $3/2$ power law as shown in Figure 14. This follows from two separate effects. First, for a given target thickness, the target impedance is inversely proportional to the area; consequently, the discharge power is proportionally higher. Second, material from the target is emitted at angles varying from nearly 0° to 90° . For a small target, the material emitted at small angles does not reach the substrate, but rather is collected on the chamber walls. As the target area increases, emission at small angles is more completely collected. A hemispherical distribution of emitted material is assumed here and, hence, the deposition rate due to this effect alone would be proportional to the target radius, which, in turn, is proportional to the square root of the target area. When these effects are combined, the rate should be proportional to $(\text{area})^{3/2}$ or to $(\text{radius})^3$.

As would be expected, the uniformity of thickness for the deposited film is also determined largely by the target area. Uniformity of film thickness within $\pm 5\%$ is found in a substrate area concentric with the target; the radius of uniformity is approximately 0.5 inch less than the radius of the target.

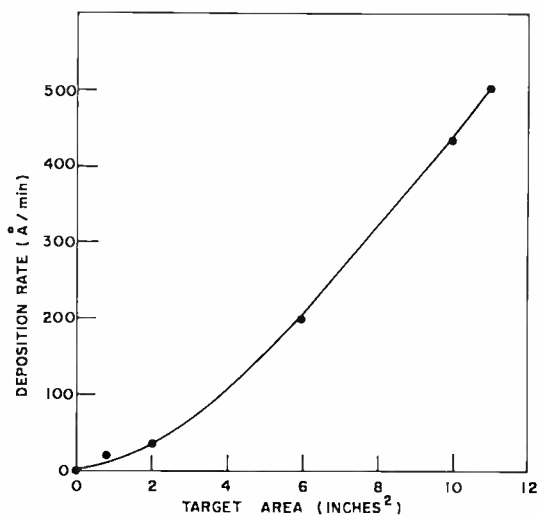


Fig. 14—Deposition rate of SiO₂ versus target area.

F. Substrate Grounding

In discussing the r-f aspects of this process, it was noted that a capacitively coupled substrate configuration could be used to determine the effect of the substrate ground return on the deposition rate. When we speak of a ground return in reference to the substrates in the system, we refer to the best ground return that can be made under the circumstances. It cannot be perfect at these frequencies.

Referring to Figure 7, we define the ratio C_3/C_2 as a measure of the quality of the ground (a short circuit is an infinite capacitance). The deposition rate as a function of the reciprocal of this ratio is plotted in Figure 15. In this configuration, part of the discharge occurs between the target and the substrate and part between substrate and ground.

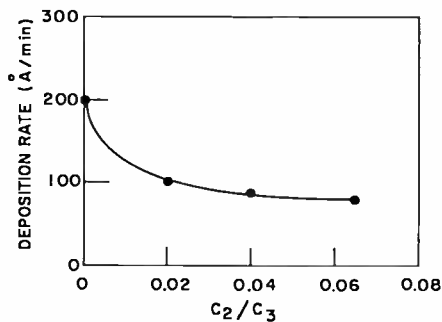


Fig. 15—Deposition rate of SiO₂ versus the quality of the substrate ground. The ratio of C_2/C_3 is a measure of the quality of the ground. (See Figure 7.)

It should be re-emphasized that the point at $C_2/C_3 = 0$ is for a substrate grounded as well as possible. If it were possible to provide a perfect ground return, the rate would, no doubt, be higher.

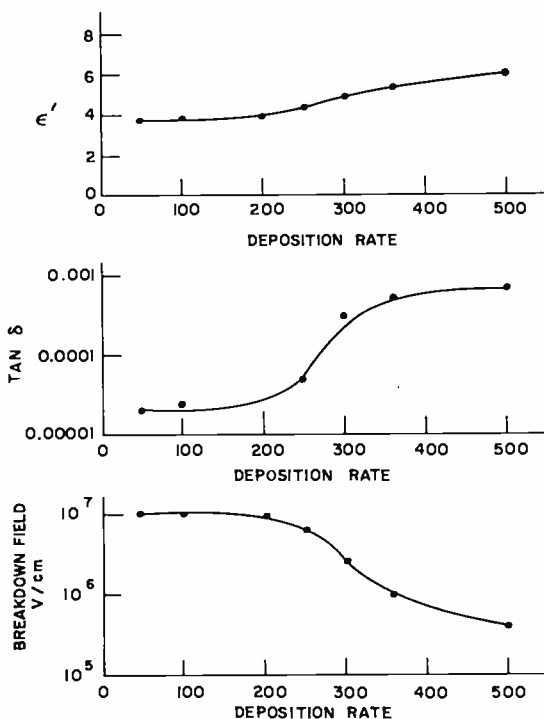


Fig. 16—The effect of deposition rate on the electrical properties of SiO_2 films: (top) dielectric constant at 1 kHz, (center) dissipation at 1 kHz, and (bottom) d-c breakdown field.

CHARACTERISTICS OF R-F SPUTTERED FILMS

In general, r-f sputtered films are highly uniform in thickness and in composition. They adhere very well to most surfaces, primarily because of physical adhesion due to the high arrival energy at the substrate as well as chemical bonding that can exist at the film-substrate interface.

The structure of the films depends to a large degree on the deposition rate and substrate temperature. For example, dielectric films, as deposited, are not very crystalline for deposition rates greater than 200 Å/min. Figure 16 illustrates the effect of this poor structure on the dielectric properties of SiO_2 films. Infrared absorption spectra (trans-

mission technique) indicate a shift of the 9.4-micron absorption peak to higher wavelengths when the deposition rate is greater than 200 Å/min. Both the infrared spectra and the dielectric properties of films deposited at high rates will approach bulk properties upon heating. For SiO₂ films, bulk properties are approached after heating in air at 300°C for three days, at 1000°C for a few minutes, or various intermediate combinations.

To achieve bulk properties in glass films, heat treatments near the softening point of glass are required for films deposited at rates higher than about 200 Å/min. Some crystalline solids deposited at rates as low as 50 Å/min have grain sizes so small (~200 Å in diameter) that they do not exhibit bulk properties. Recrystallization and grain growth are accomplished by heat treating after deposition^{18,19} or by using a high substrate temperature during deposition if the material is not volatile.

R-F SPUTTER ETCHING

Anderson et al⁹ utilized r-f sputtering as a technique for cleaning the inside walls of tubes used in their studies of sputtering yields. Davidse²⁵ utilized the technique for pattern generation.

The same equipment can be used both for etching and for depositions and the system described herein was designed with this dual function in mind. The method of operating the system for sputter etching is somewhat different however. Since the piece to be etched is the target, one is concerned only with effects that occur at the target; the collection of material elsewhere is not of primary concern. The following operating variables must be considered in etching:

1. The gas pressure should be kept low so as to prevent material emitted from the target from being reflected back.
2. A very wide separation between the target and ground plane should be used to allow the gas pressure to be kept low even at low r-f voltage.
3. All grounded parts of the system should be kept at least one inch away from the edges of the piece being etched. Closer spacings result in ground-plane focusing of the ions, which, in turn, results in a higher rate near the ground plane than at points farther removed from it (i.e., nonuniform etching).

It is convenient to differentiate between etching used to thin a material uniformly and etching to generate a pattern.

To thin a material uniformly requires only that the part to be

²⁵ P. D. Davidse, "RF Sputter Etching—A Universal Etch," *Extended Abstracts, 13th National Vacuum Symposium (American Vacuum Society)*, 1966, San Francisco, California.

thinned be placed on the target backing plate. Just as for deposition by sputtering, sharp edges and corners should not be exposed to the discharge. When the thickness of the piece being etched approaches about 1% or more of one electron mean-free-path length, the edge of the sample becomes a high-field point. The surface must then be made flush to eliminate nonuniform etching at the edges. This can be done in several ways. For instance, the pieces to be etched can be recessed into the backing plate, or a recessed mold suitable for the pieces can be placed on the backing plate and the pieces put in it.

When thinning a layer uniformly, one can refer to a specific etch rate for the material involved. However, when the technique is used for pattern generation, this is no longer true. When a pattern is to be etched into a surface, some kind of mask material must first be applied to the surface. The mask material is then removed during sputtering at the same time as the rest of the surface. The mask material and the material to be etched form a *new composite surface* that generally has a different etch rate than that of either the mask material or of the material being etched, alone. Therefore, to speak of *the* etch-rate of a material has little meaning. The etch rate in pattern generation is specific to the combination of the material being etched, the mask material, the pattern, and the substrate. The etch rate for each combination must be empirically derived. Once the etch rate for a given combination has been derived, it is quite reproducible and easy to control.

The masking material must be sufficiently thick so that some of it is left after etching through the desired thickness of the other material. This thickness must be determined empirically as discussed above. In general, the mask material should always be somewhat thicker than the final etch depth.

For fine patterns, the customary mask materials are photosensitive resists. These organic resists can be cross-linked by the discharge. Some resists cannot tolerate even mild discharge conditions without blistering, cracking, etc. Even with those resists that do not suffer mechanical damage during sputtering, removal of resist after etching can lead to problems because of additional cross-linking. This usually requires that relatively mild discharge conditions be used.

As discussed above, the limit on the etch depth is determined by the removal rate of the mask material as compared with that of the material being etched. With photosensitive resists, however, the edge definition becomes poorer as the resist thickness increases. Therefore, a compromise is sometimes necessary between the etch depth desired and etch definition required.

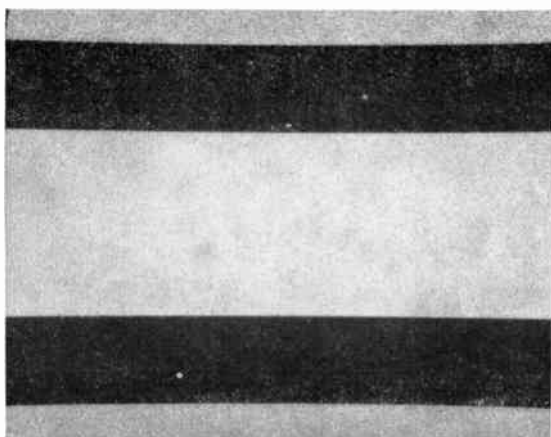


Fig. 17—Photomicrograph of W sputter etched from a Si surface (Dark lines are Si, 10 microns wide.)

Definition in the etched sample is limited only by the quality of the mask pattern. Figure 17 shows a photomicrograph of a sputter-etched line that illustrates the definition that can be obtained. Figure 18 shows an angle lapped section of a sputter-etched line, demonstrating that the etched out walls are vertical and that there is no undercutting. Tsui²⁶ presented scanning electron micrographs that demonstrate this very well.

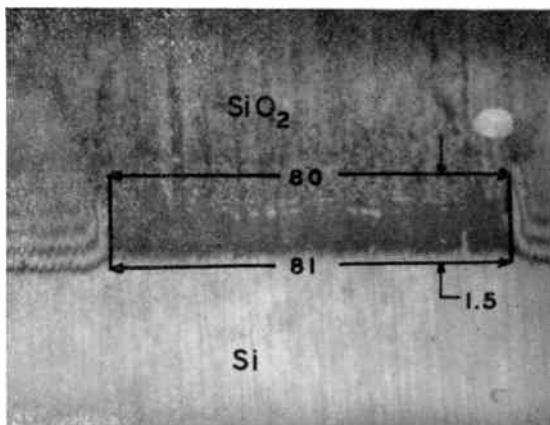


Fig. 18—Photomicrograph of a 3° angle lapped section of a sputter etched line. The etch depth is 1.5 microns and the line width is 80 microns. Angle lapping includes the effects of photoresist definition and the wall contours.

²⁶ R. T. C. Tsui, "Ion Etch Technique and Its Applications," paper presented at the Second Symposium on the Deposition of Thin Films by Sputtering, Univ. of Rochester, (June 7, 1967).

In sputter etching, the discharge voltage must be adjusted for a given material depending upon the degree of surface damage due to ion penetration that can be tolerated. Substantial radiation damage is found to occur in planar silicon junctions unless the junction is passivated by at least 0.2 micron of oxide. Radiation damage to surfaces by ion penetration is a very complex phenomenon²⁷ and cannot easily be treated theoretically, even for single crystals.

As described previously, certain crystalline oxides can be chemically reduced by argon discharges. If this is a problem with the particular sample to be etched, an oxygen or argon-oxygen discharge should be used.

SUMMARY

R-F sputtering is a valuable and versatile process for the fabrication of thin films for many different device applications. The process has the following main advantages:

1. It is versatile. Any target material (conducting or nonconducting) may be used; for some materials, however, the films deposited may not be identical in composition to the target.
2. Precise control of deposition rate and film thickness is easily maintained.
3. Uniformity of film thickness and stoichiometry over large substrate areas is excellent.
4. The deposited film generally has excellent mechanical properties (adhesion, etc.).

The main disadvantages of the process are:

1. The rates of deposition are relatively slow.
2. The basic process mechanism is complex.

The deposition rates can be and have been increased by various techniques; however, it seems generally true that the higher the rate of deposition, the poorer the quality of the films. This is also usually true for other deposition methods. In the case of r-f sputtering, we find that a deposition rate of the order of 200 Å/min. is the best compromise between processing speed and film quality for most of the materials investigated to date. This rate is substantially lower than the best compromise for other processes. If this remains true, even after further research, it is evident that r-f sputtering is truly useful only for thin films (less than a few microns) unless long processing times are tolerable. As the deposition rate is increased, not only do

²⁷ See, for example: E. M. Baroody, "Influence of Anisotropic Scattering on Stopping by Elastic Collisions," *J. Appl. Phys.*, Vol. 36., p. 3565, (1965); E. M. Baroody, "Stopping by Elastic Collisions of Particles from a Unidirectional Plane Source," *J. Appl. Phys.*, Vol. 35, p. 2074, (1964).

the film properties degrade, but rate and thickness control become more difficult.

Even though in the scientific sense the mechanism of sputtering is complex and not well understood, from a practical standpoint excellent control is achieved in a well-designed system. For example, we have been able to control the deposition rate to $\pm 3\%$ from run to run on a routine basis. Once all of the variables described herein have been characterized, control of deposition rates is relatively simple.

Similarly, the use of r-f sputtering as an etching technique is quite useful. The main advantages of r-f sputter etching are:

1. It is universal in the sense that any solid material can be etched.
2. Sputter-etching requires no chemical reagents and leaves no residues.
3. The definition of patterns is limited only by the definition of the mask used.
4. The side walls of etched patterns are vertical and there is no undercutting.
5. Etch rates are easily controlled.

The main disadvantages of r-f sputter-etching are:

1. Etch rates are relatively low.
2. When organic photoresists are used to delineate patterns, the etch rate must be kept very low to avoid degradation of the resist itself.
3. If the surface to be etched is a thermodynamically unstable material, dissociation of the material at the surface can occur.
4. In surface-sensitive devices, radiation damage can adversely affect the surface.

ACKNOWLEDGMENTS

We should like to acknowledge J. W. Gaylord's continuing help with the r-f aspects of this work. J. J. Pacia was most cooperative in providing mechanical assistance through the course of our investigations regarding the physical design of the sputtering system. J. A. Amick offered many valuable suggestions after critically reading the manuscript.

LAMINATED FERRITE MEMORIES—REVIEW AND EVALUATION

BY

R. SHAHBENDER

RCA Laboratories
Princeton, New Jersey

Summary—Laminated ferrite memories are a development of RCA Laboratories. The fabrication technology for laminates is briefly described and the results of pilot plant operation are presented. Systems characteristics for operation at cycle times and capacities suitable for computers are reviewed and evaluated with respect to other computer technologies.

INTRODUCTION

LAMINATED (or monolithic) ferrite memories, a development of RCA Laboratories, have performance characteristics, in terms of capacity and speed, that anticipate the needs of future computers. These needs are expressed in terms of a hierarchy of memories having cycle times in the range of 0.1 to 5 microseconds and corresponding capacities of 10^5 to 10^8 bits. A review, and evaluation of RCA's effort in laminates is presented in this paper.

The fabrication technology¹⁻³ for laminates is briefly described, and the results of a pilot-plant operation are reviewed. Systems characteristics for operation at 0.2 microsecond^{4,5} and 0.5 microsecond^{3,6}

¹ R. Shahbender, C. Wentworth, K. Li, S. Hotchkiss, and J. A. Rajchman, "Laminated Ferrite Memory," *RCA Review*, Vol. 24, p. 705, Dec. 1963 (see also *Proc. Fall Joint Computer Conf.*, p. 77, Nov. 1963).

² R. Shahbender, C. Wentworth, K. Li, S. Hotchkiss, and J. A. Rajchman, "Laminated Ferrite Memory," *Proc. Intermag. Conf.*, p. 5-6-1, April 1964.

³ I. Abeyta, M. M. Kaufman, P. Lawrence, "Monolithic Ferrite Memories," *RCA Review*, Vol. 27, p. 77, March 1966. (Also *Proc. Fall Joint Computer Conf.*, p. 995, 1965).

⁴ G. R. Briggs, J. T. Grabowski, and J. W. Tuska, "Laminated Ferrite Modular Memory for 150-250 NS Cycle Operation" *Abstracts Intermag. Conf.*, April 1968 (to be published in *IEEE Trans. on Magnetics*).

⁵ K. Li, "High Speed Characteristics of Laminated Ferrite Memory Planes" *Abstracts Intermag. Conf.*, April 1968, *IEEE Trans. on Magnetics*.

⁶ M. M. Kaufman, R. L. Pryor, A. Gilewitz, "Monolithic Ferrite-Integrated Storage Diode Memory," *Proc. International Solid State Circuit Conf.*, Phila., Pa., p. 98, Feb. 1966.

cycle times are summarized from published papers. The results of a research program⁷⁻¹⁰ for realizing large-capacity, low-power memories are presented. A more detailed description of this program is given in a companion paper.¹¹ Finally, the laminates are evaluated with respect to other technologies.

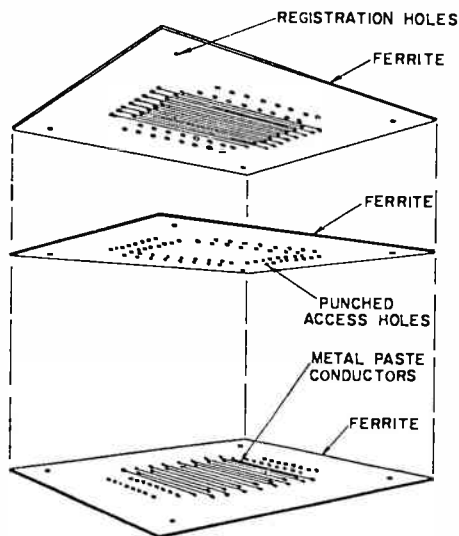


Fig. 1—Laminate construction.

FERRITE WAFER FABRICATION

The laminated ferrite wafer,¹⁻³ as shown in Figure 1, is constructed by sandwiching two groups of conductors between very thin sheets of

⁷ R. Shabbender, "Laminated Ferrite Memory, Phase I," Final Technical Report Contract NASw-979, NASA CR-398, National Aeronautics and Space Administration, Washington, D. C., March 1966.

⁸ R. L. Harvey, I. Gordon, A. D. Robbi, "Laminated Ferrite Memory—Phase II," Final Technical Rep., Contract NASw-979, National Aeronautics and Space Administration, Washington, D. C., August 1966. ("Low Drive, Temperature Stable Ferrite for Laminated Memory Array," *IEEE Trans. Magnetics*, p. 526, Vol. MAG-3, 1967).

⁹ J. T. Wallmark, W. A. Bosenberg, E. C. Ross, D. Flatley, H. Parker, "MOS Field-Effect Transistor Technology," Final Rep., Contract NAS 1-5794, National Aeronautics and Space Administration, Washington, D. C., Aug., 1967.

¹⁰ A. D. Robbi, J. W. Tuska, "Integrated MOS Transistor-Laminated Ferrite Memory," (Abstract), *IEEE Trans. Magnetics*, p. 329, Vol. MAG-3, 1967.

¹¹ I. Gordon, R. L. Harvey, H. I. Moss, A. D. Robbi, J. W. Tuska, J. T. Wallmark, and C. Wentworth, "An MOS Transistor-Driven Laminated Ferrite Memory," *RCA Review*, June 1968, p. 199 (this issue).

ferrite to form closed-flux-path storage elements. The pilot-line wafer is just over one inch square and less than 6 mils thick. Each group of conductors consists of 64 parallel straight lines in a planar array with center-to-center separation of 15 mils as shown in Figure 2. The conductors of one group are placed at right angles to those of the other group. Their vertical separation is less than one mil.

Palladium paste is squeegeed through a metal mask onto a glass substrate to form the conductor patterns. The metal mask is removed and the ferrite in the form of a slurry is doctor bladed over the line

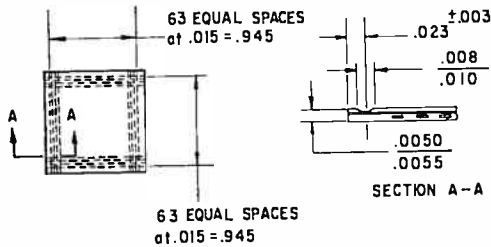


Fig. 2—Detail of basic ferrite wafer.

pattern. This is allowed to dry forming a ferrite sheet which is then peeled off the glass surface. Three sheets are laminated together (two sheets containing conductors and one sheet serving as an insulator) to form a ferrite wafer. The wafer is 1.2 inches square in the unfired state, and is conventionally sintered to yield square-loop properties. After sintering, the ends of the palladium conductors are exposed for electrical connections. This is accomplished by using an "airbrasive" machine to erode away the ferrite covering the ends of the conductors. The electrical resistance of the 1-inch embedded conductors is typically 2.5 ohms.

As mentioned above, the unfired wafer is 1.2 inches square. The fired wafer is approximately one inch square. This represents a shrinkage in lateral dimensions of approximately 20%. Inability to hold the fired dimensions of the wafers to better than ± 10 mils is a limiting factor in the production of laminates. With this tolerance in dimensions, it is not possible to devise simple mass interconnection schemes to connect the embedded conductors to external circuitry since the center-to-center spacing of the conductors are not sufficiently uniform and reproducible from sample to sample.

After exposing the ends of the conductors, photoetched copper conductor combs are manually soldered to the ends of the embedded con-

ductors on all four edges of laminate—a total of 256 soldered connections per wafer. The wafer with the attached conductor combs is next enclosed in a semihermetic package containing a molecular sieve in a silicone grease to prevent changes in the resistance between conductors as a result of operation in high-humidity ambients. At this stage, the wafer can be electrically and magnetically tested to determine the performance characteristics of individual storage locations.

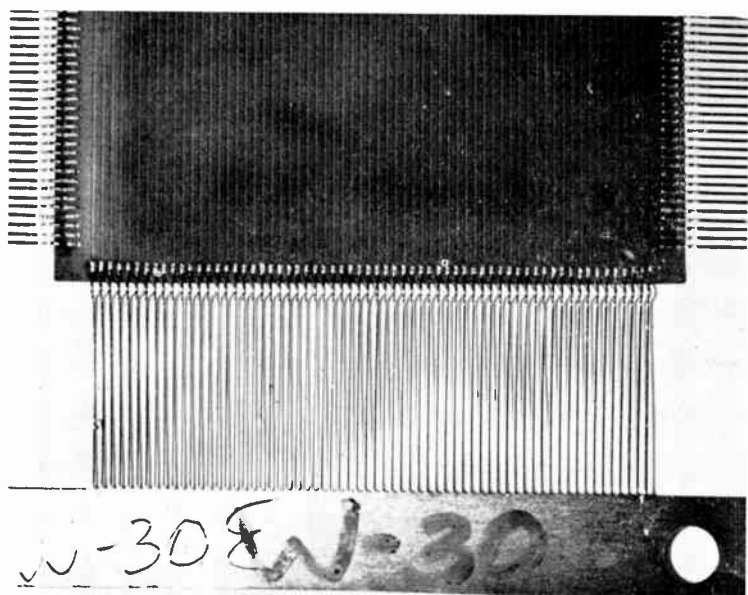


Fig. 3—Portion of wafer showing conductor combs attached to embedded windings. Dimple in corner is a point mark used for reference.

Figure 3 shows part of an unencapsulated wafer with the photo-etched conductor combs attached to it, and Figure 4 shows an encapsulated wafer with the conductors projecting from the encapsulating package. Test data on encapsulated wafers showed no change in the resistance between conductors for wafers subjected to temperature ambient of 100°C, a relative humidity in excess of 90%, and an applied potential of 30 volts for a period of six months. This demonstrates that the encapsulation technique developed is adequate for preventing deleterious effects resulting from atmospheric ambients.

PILOT-PLANT OPERATION

The RCA Memory Products Division at Needham, Mass., established

a pilot-plant operation to produce laminates for memory systems. Using the fabrication technology described above, it was found that 50% of the wafers with exposed conductors had mechanically acceptable characteristics as determined by visual examinations. The major causes of wafer rejections at this stage were

1. Human error in establishing sintering conditions, resulting in excessive mechanical distortion of the wafers.

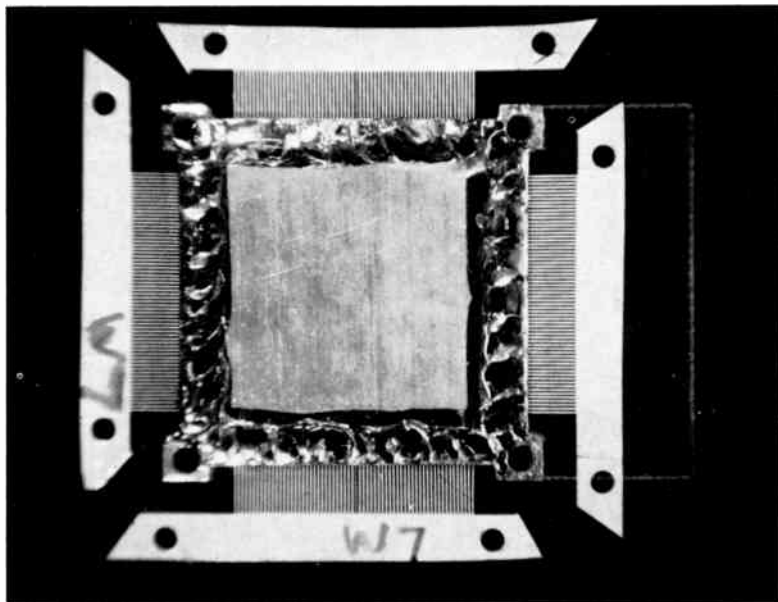


Fig. 4—Encapsulated wafer with conductor combs protruding from encapsulating package.

2. Microcracks and local distortions in the wafers due to ceramic particles on the ceramic substrates on which the wafers are placed for sintering.

3. Damage to the edges of the wafer during the "airbrasive" operation to expose the embedded conductors.

During a 6-month period records were maintained on a weekly basis of the ratio of the total number of wafers passing mechanical inspection to the total number of wafers passing all electrical and magnetic testing after encapsulation. Figure 5 shows the yield data obtained in that period with an average of 17.1% and a maximum of 50%. This yield is based on all bits in a wafer having acceptable electrical and

magnetic characteristics. If a single bit in a wafer (one intersection out of 4096) has unacceptable characteristics, the wafer is rejected. In operation of a laminate memory, no redundant locations are utilized, and it is assumed that a 100% operation of each wafer is necessary to result in economic memory systems.

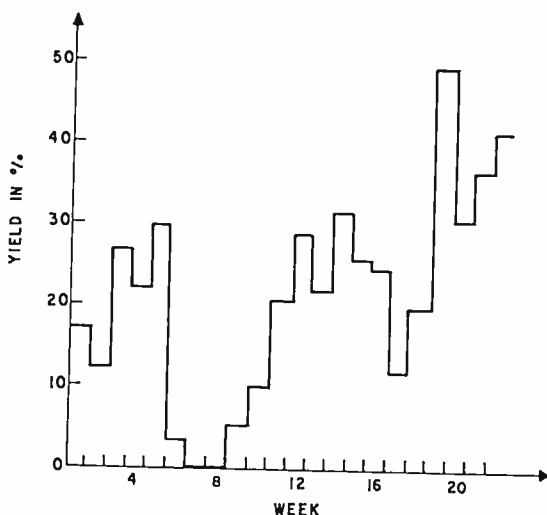


Fig. 5—Wafer yield.

For the manual operation of soldering the interconnection combs and encapsulating the wafers, the pilot-plant operation demonstrated that two wafers per hour per operator could be processed. This involved making 256 soldered connections and encapsulating the wafer in its package. The etched combs are photoformed and mechanically shaped to simplify the interconnection.

LAMINATED FERRITE MODULAR MEMORY ^{4,5}

For the next generation of computers it is anticipated that main frame memory cycle times of less than 0.2 microsecond are required. A design to meet this target objective was developed. The design exploits the potential of large-scale integration (LSI) of semiconductor elements for reducing the ratio of semiconductor costs to magnetic stack costs in memory systems while utilizing relatively greater number of semiconductor components. By distributing the magnetics and semicon-

ductors in modules throughout the system, faster operation, improved signal-to-noise ratio, lower digit power, and wider operating margins are obtained.

The basic design is aimed at realizing a memory capacity of 32,000 words, with 64 bits per word. The store is arranged as an 8×8 array of modules as shown in Figure 6. Each module contains 512 words

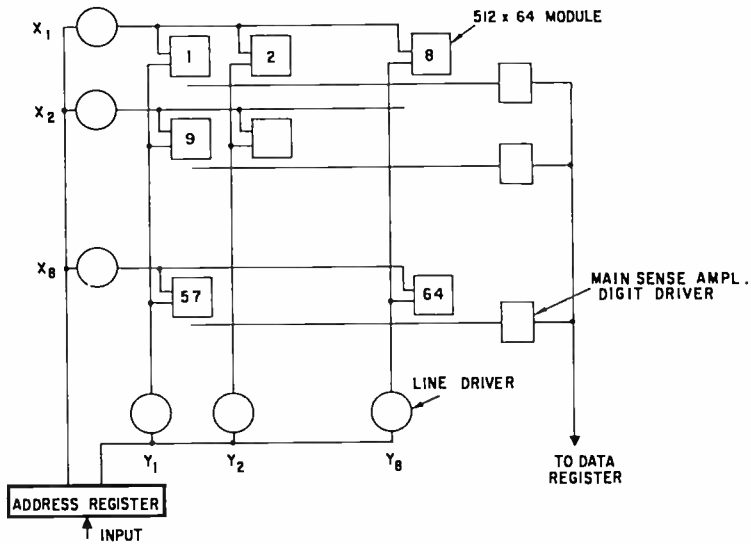


Fig. 6—Modular memory organization.

(32,000 bits per module) and is operated in a 2D organization with two intersections per bit. The word read-write currents are supplied by self-contained diode matrix bipolar transistor switches in each module. The switching circuits receive partially decoded low-level address signals from decoder-line drivers arranged in eight x and eight y circuit groups. These groups are driven from the address register via buffers. For reading, preamplifiers in the modules are gated to information lines, and for writing, digit control signals are gated to the module digit drivers. Final sense amplification and digit control circuitry is provided peripherally. All circuits are transformerless to facilitate integration. The word drivers use complementary circuits to supply positive and negative current pulses to a memory module.

To establish the technical performance characteristics of the memory, a 512×64 bit module was constructed from encapsulated wafers supplied by the RCA Memory Products Division. The selection diodes

are integrated in strips of eight diodes encapsulated in glass packages. Two diodes (from adjacent strips) are used per word to supply the read and write currents. The diodes, on 15-mil centers, are mounted along the edges of the laminates, as seen in Figure 7. Connections to the word lines are made by planar combs.

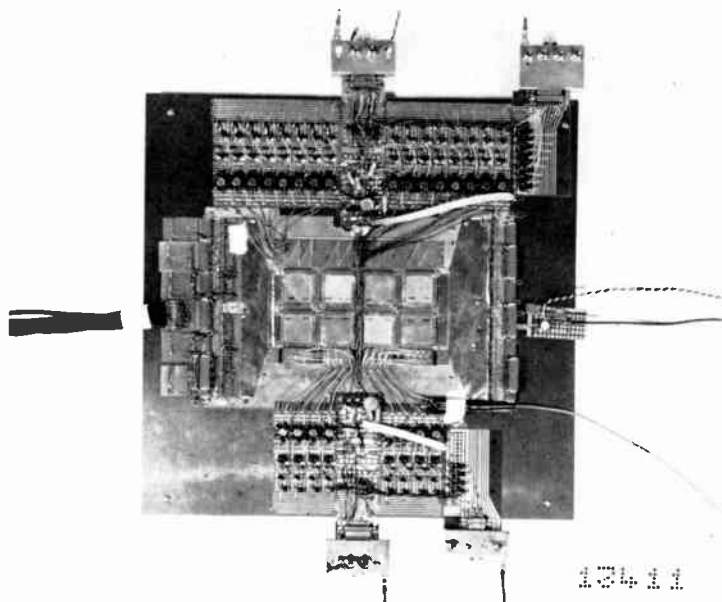


Fig. 7—512 × 64 bit memory module. Each wafer measures 1 × 1 inch approximately.

For the test module, the word-selection circuitry is constructed from nonintegrated circuits and mounted on the platter containing the laminates (Figure 7). One-half of the memory module (256 words) is assembled on one surface of the platter and the remaining words are placed on the reverse side of the platter. Partial digit sense circuitry was also built to test memory operation. In addition, module-selection circuitry was assembled from partially integrated circuits to permit measurements of propagation delays and loading effects.

Laminates made from two ferrite compositions, MgMnZn and MgMn, were extensively tested to determine their high-speed operating characteristics. The MgMnZn composition, used for high-speed cores, was used for the pilot production of laminates. The MgMn composition was subsequently experimentally found to yield superior results. Table

I summarizes the characteristics of both compositions for operation at 125 nanoseconds cycle time. The main advantages of the MgMn over the MgMnZn composition are the invariance of sense signal with repetition rate resulting from a higher Curie temperature; the shorter

Table I—Switching Characteristics of Laminates for 125 Nanoseconds Cycle Time

	Ferrite Composition	
	MgMnZn	MgMn
Curie Temperature (°C)	205	270
Coercive Force (oersted)	1.5	2.5
Peak Read Current (A)	0.6	0.7
Bit Back Voltage (mV)	250	250
Digit Current (mA)	25	35
Sense Signals with RZ Digiting		
Low Duty Cycle Read-Write (mV)	7.6	7.3
High Duty Cycle Read-Write (8 mHZ) (mV)	4	6.7
Sense Signals with NRZ Digiting		
Low Duty Cycle Read-Write (mV)	10.5	13.0
High Duty Cycle Read-Write (mV)	5	12
T_R (ns)*	145	85
Propagation Delay for 1024 Words (ns)	32	20
Test Conditions		
Read Current		
Rise Time/Width at Base (ns)		30/45
Write Current Width at Base (ns)		35
Digit Current		
RZ Width at Base (ns)		45
NRZ Minimum Width at Base (ns)		85

* T_R Digit current width at base giving sense output of 90% of that with d-c digit current for high-speed read-write pulses.

propagation delay resulting from greater squareness; and the considerably shorter relaxation time permitting operation in a non-return to zero (NRZ) mode⁴ (doubling of the sense signal) for a cycle time of less than 200 nanoseconds. The slightly higher read and digit currents required with the MgMn composition are well within the capability of

the transistor drive circuitry. For the test module, MgMnZn wafers were utilized, since these were readily available.

For the test module, the read-write drivers are operated from power supplies of -25 and $+17$ volts, as shown schematically in Figure 8. The digit-sense lines are connected in four-arm balanced bridge circuits, each bridge arm containing 256 intersections as shown schematically in Figure 8. Digitizing is simulated NRZ using digit current

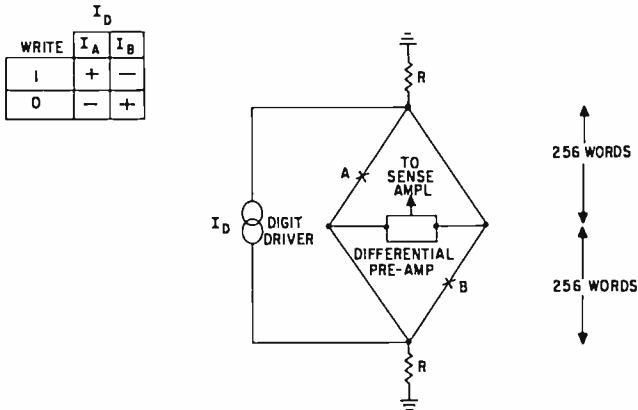


Fig. 8—Bridge circuit for digit-sense windings for modular memory (A and B are the two elements of a bit).

duration of 200 nanoseconds. With optimum settings, the module reading time (measured from 50% of the voltage switch input to peak of the sense preamplifier output) is approximately 67 nanoseconds. The peak noise at read time averaged ± 1.7 mV and did not exceed 3.25 mV in the worse case. Digit-sense line recovery following the digit transition occurred in 150 nanoseconds. Disturbed sense signals with a minimum value of ± 7 mV for the module were obtained. Decreasing power supply voltages by 25% decreased the sense signals by 20%, but produced little shift in peaking time. The test data in general showed operating margins of $\pm 10\%$.

For the MgMnZn wafers, digit-sense line recovery was found to be sensitive to the stored information patterns. For worse-case patterns, a recovery time as long as 230 nanoseconds occurred. With MgMn wafers, the recovery time is considerably less sensitive to stored information patterns and for worst-case conditions is 90 nanoseconds.

By combining the data for the test module, the module selection circuitry, and digit-sense amplifier circuitry, estimates of the access time and cycle time for the modular memory system were made. For a system utilizing MgMnZn wafers with conductors on 15 mil centers,

the access time for a 32,000-word system is 112 nanoseconds. For a design based on MgMn wafers with 10-mil spacing between conductors, the access time is approximately 100 nanoseconds. For the MgMnZn wafer system, a 250-nanosecond minimum cycle time is possible using NRZ digitizing and address overlap. For the MgMn laminated design a cycle time of 120 nanoseconds is possible with extreme address overlap; 150-nanosecond cycle with moderate overlap; or 200 nanoseconds without address overlap.

LAMINATES FOR 0.5-MICROSECOND MEMORIES ^{3,6}

Feasibility of the modular memory depends on the development of LSI techniques to maintain bit costs at economic levels. More immediate use of laminates is possible utilizing conventional bipolar transistor circuits operating at speeds compatible with a memory cycle of 0.5 microsecond or less. A program to evaluate laminates for this speed range was undertaken as described below.

A 2048×32 bit stack was assembled and completely tested. The stack was assembled from pilot-plant wafers using MgMnZn composition. Each wafer contained 64×64 intersections and was encapsulated in a semi-hermetic package. The memory is operated in a word-organized, two-intersections-per-bit mode. The stack was assembled as two sub-stacks with each sub-stack containing 1024×64 storage intersections. Each sub-stack contained 16 wafers and its own glass-encapsulated selection diodes. The sense-digit windings were serially connected through each sub-stack. Figure 9 is a photograph of the memory stack with each sub-stack occupying a volume of $1.5 \times 2 \times 2.5$ inches. The selection diodes for the stack were organized as a 64×32 switching matrix.

For the system, a cycle time of 450 ns was achieved with an access time of 150 ns. The digit recovery time using RZ (return to zero) digitizing is 250 ns. Typical drive requirements are 450 mA read (at 90 ns rise time), 150 mA write, and 20 mA digit. For these drive conditions the minimum stack sense signal is 5.5 mV. The worst read noise is 0.5 mV, while the worst digit transient noise (at 450 ns cycle time) is 2 mV. Under worst-case conditions, these two effects add to give a total noise of 2.5 mV. Figure 10 shows schematically the connection of the sense digit windings. The relatively long digit transient recovery is related to the relaxation effects in the MgMnZn wafers, and resulted in the relatively long recovery time of 250 ns. Use of MgMn wafers would result in a considerably shorter digit recovery and faster cycle time. Figure 11 shows the operating margins for the memory system at a cycle

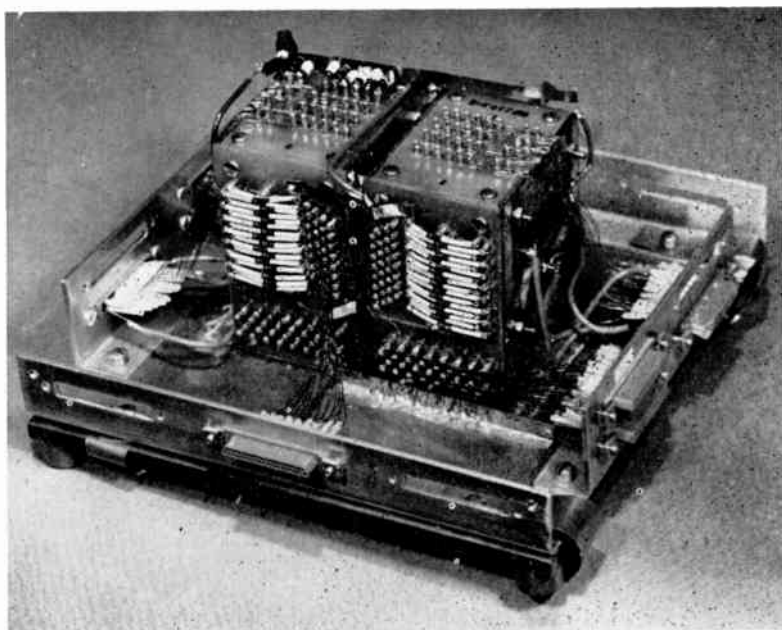
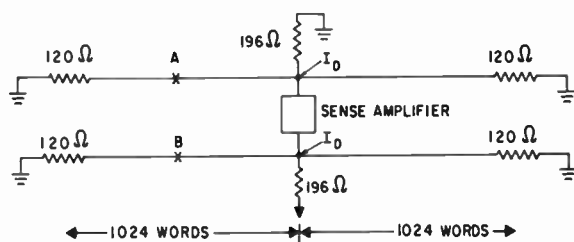


Fig. 9—Memory stack of 2048×32 bits. Each substack measures $1.5 \times 2 \times 2.5$ inches and includes diode matrix.

time of 450 ns as determined with a memory exerciser with error detector. As can be seen, the margins are quite good and are possible because of the inherent uniformity and close dimensional tolerances of the memory stack.



	I_D	
WRITE	I_A	I_B
1	+	-
0	-	+

Fig. 10—Sense-digit circuit for 0.5 microsecond memory (A and B are elements of a bit).

Additional data was obtained to determine the maximum word length that could be utilized in a memory system. A cross section with 64 words by 128 bits was tested and demonstrated that the current rise times could be maintained at 128 bits, and that the noise during

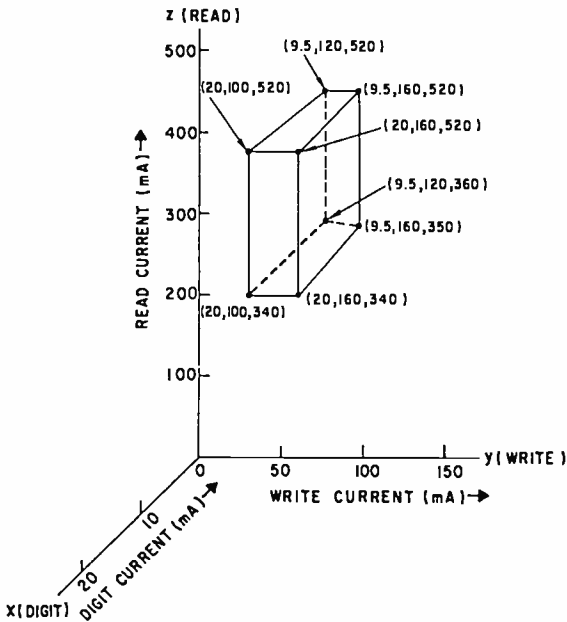


Fig. 11—Current operating margins for a 2048-word by 32-bit monolithic ferrite memory at a cycle time of 450 ns.

read time did not increase significantly because the laminates have a high common-mode rejection ratio. Thus, it is expected that systems with 2048×128 bits could be operated at 0.5 microsecond or less. Further, the substitution of MgMn ferrite with 10-mil-spaced conductors could result in significant reduction in this cycle time.

LAMINATED FERRITE MASS MEMORY*

The small effective size of the storage element in a laminated wafer may be exploited for realizing moderate-speed mass memories by oper-

* This program was partly supported by NASA under Contracts NASw-979, "Laminated Ferrite Memory—Phase I and Phase II; and NAS1-5794, "MOS Field-Effect Transistor Technology".

ating at very low power.⁷⁻¹³ Under these conditions, the drive currents and sense signals are compatible with low power, LSI transistor circuits. The design objective pursued at RCA Laboratories is a system module with a capacity of 65,000 words, each 150 to 250 bits long, i.e., a total capacity of 10^7 bits. The cycle time expected is in the range of 1.5 to 3.5 microseconds depending on the number of bits serviced by each sense amplifier/digit-driver circuit.

To realize the design objectives, the program, as described fully in the companion paper,¹¹ concentrated on:

1. Synthesis of low-drive ferrite composition.⁸
2. Fabrication of memory arrays with 256×128 storage locations.⁷
3. Development of integrated semiconductor circuitry for word drive, digit drive, and sense.^{7,9}
4. Systems simulation, test and evaluation.⁹

Briefly, the results obtained from this program are:

Ferrite Synthesis

An MgMnZn ferrite was synthesized with a coercive force of 1.3 oersteds, a squareness ratio in excess of 0.9, a switching coefficient of 0.5 oersted/microsecond, a material resistivity of 2×10^7 ohm centimeter, a Curie temperature of 260°C, and a grain size less than 10 microns. Laminates made from this composition displayed operating characteristics that are eminently well matched to integrated semiconductor circuits.

Wafer Fabrication

For a mass magnetic random-access memory such as the $2\frac{1}{2}$ D two-wire core system, a major fraction of the memory-system cost is in the magnetic stack. To achieve economic bit prices with a laminated memory, it is necessary to utilize wafers with considerably more storage elements than the 64×64 arrays produced by the pilot operation. For this reason, two alternative fabrication technologies—embossing and pressure sintering^{13*}—are being developed to permit the construc-

¹² R. C. Ricci, P. J. Truscillo, "A Monolithic Ferrite Space Memory," *Proc. National Electronics Conf.*, Chicago, Ill., p. 758, Oct. 1966.

¹³ H. I. Moss, A. D. Robbi, "High-Pressure Sintering of Ferrites," Final Rep., Contract DA36-039-AMC-037 10 (E), United States Army Electronics Command, Fort Monmouth, N. J., July 1967.

* Work on high pressure sintering of computer ferrites was partially supported by the USAECOM, Fort Monmouth, New Jersey, under Contract DA-36-039-AMC-037 (E), "High Pressure Sintering of Ferrites". Fabrication of laminated arrays by high pressure sintering is partially supported by NASA under Contract NAS 12-574, "10⁸ Bit Low Power Laminated Ferrite Memory".

tion of wafers with 256×128 intersections. At present, large size wafers are successfully produced with the embossing technology but suffer the same mechanical difficulties as the small wafers. The conductor center-to-center distances (10 mils) are nonuniform and nonreproducible from sample to sample. In addition, the conductor ends must be exposed by airbrasive erosion of the ferrite. With pressure-sintering it is hoped to produce wafers with solid conductors, embedded in the ferrite, protruding from the edges of the wafer on uniform and reproducible centers. By using a large wafer (256×128) the number of bits per connection is increased by a factor of 3, resulting in higher reliability and lower cost.

Integrated Semiconductor Circuit Developments

A metal-oxide-semiconductor transistor is inherently a bidirectional switch and may be used to steer positive and negative current pulses for read and write in a 2D laminated memory. Integrated word switch-strip designs with one transistor per word were developed and fabricated on an experimental basis.⁹ Each switch strip, as shown in Figure 12, contains 64 transistors on 10-mil centers matching the conductor spacing in the laminates. Each transistor is capable of delivering a read current of over 100 mA and a write current of 70 mA.

A 64-output quaternary address decoding tree was designed and fabricated as an integrated MOS structure. Figure 13 shows four such trees on a silicon wafer prior to dicing. The tree could be used as a building block to construct an address decoder with 1024 outputs. Each output on the address decoder would fan to 64-word driver gates on separate switch strips. The address decoder in combination with 64 read-write current sources would provide decoding for 65,000 words.

Scaled-down versions of the MOS word switches were developed for use as digit drivers. These were capable of delivering 20 to 40 mA of digit pulses. An integrated bipolar transistor sense amplifier was designed and experimentally fabricated with an overall gain of 700, a bandwidth of 3 MHz, and a threshold of 0.5 mV. Standby power dissipation in the amplifier is 135 mW.

Systems Test and Evaluation

A small memory cross section, as described in the companion paper,¹¹ was constructed and tested.^{9,10} For operation in a two-intersection-per-bit mode with unipolar digit pulses and with read currents of 100 mA having a rise time of 0.25 microsecond, the nominal sense signals are ± 2 mV, with a back voltage of 40 mV per bit. From

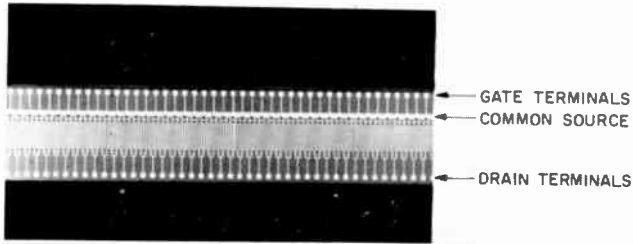


Fig. 12—Photomicrograph of 64-output MOS word switch (44 units shown).

measurements on the propagation characteristics of the sense digit windings, it is estimated that a cycle time of 3.5 microseconds can be realized for a system in which each sense amplifier/digit driver circuit services 8,000 bits, and a cycle time of 1.5 microseconds can be realized with the circuit servicing 2,000 bits. These cycle times are determined mostly by the recovery of the sense winding following the digit transient.

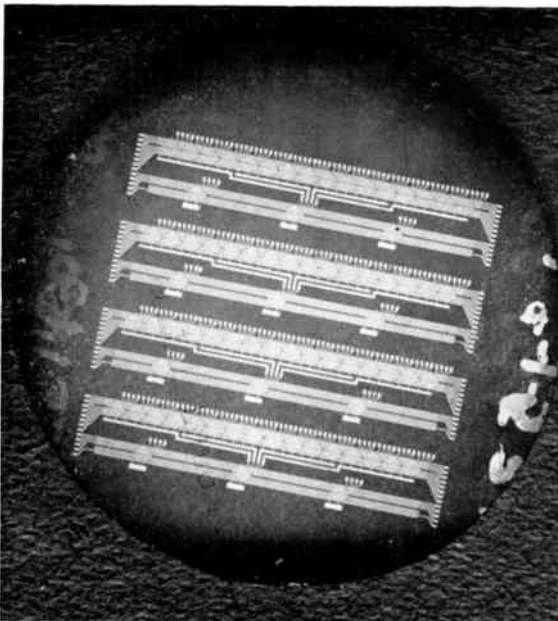


Fig. 13—Silicon wafer with four tree decoders. Each decoder is a 64-output p-MOS quaternary tree with outputs on 10-mil centers.

A redesign of the integrated sense amplifier to permit the use of preamplifiers multiplexed into a final amplifier section reduces the standby power consumed by the sensing circuits. With this redesign it is estimated that a 10^7 -bit memory operating at a continuous read-write cycle time of 2 microseconds would require 100 watts, occupy a volume of 300 cubic inches, and weigh 20 pounds. Reduction in memory volume and weight by a factor of approximately 2 may be realized by operating in a one-crossover-per-bit mode. However, this will require considerable improvement in the uniformity of the magnetic characteristics of the laminates.

EVALUATION AND STATUS OF LAMINATES

For a magnetic memory system, the ratio of semiconductor cost to magnetic stack cost depends on the cycle time and capacity of the system. For a high-speed system, the semiconductor costs to a large extent dominate the picture. The modular memory, as described, attains a high degree of compatibility between integrated circuits and memory stack. Economic feasibility of the system hinges on the economic feasibility of integrated circuits at low production volume. In addition, a reasonable mass interconnection technique for the laminates must be realized to facilitate system construction. This is expected to be attained with the pressure-sintered laminates. Technical performance characteristics realized with the modular system are competitive with those of plated-wire or flat-film memories. However, all-semiconductor memories in LSI form may eventually be a more attractive and economic approach for realizing high-speed memories.

For memory systems operating at 0.5 microsecond cycle time, presently available designs based on $2\frac{1}{2}D$ core arrays meet the needs of the computer industry. Laminated memories in this cycle time range offer no economic advantages over core systems for commercial applications. However, for space-borne and military applications, the laminates with their higher packing density, smaller volume, and lower operating power may be of use.

For systems with a capacity of 10^7 to 10^8 bits, the magnetic stack is the dominant cost item. For such systems, the laminates offer the potential of lower bit cost as a result of lower magnetic stack cost. In addition, the compatibility between the magnetic stack and the integrated semiconductors facilitates the task of integrating the semiconductor circuits.

The program demonstrated the feasibility of utilizing MOS inte-

grated circuits for operating laminated arrays. However, production of word-driver switching strips with their large MOS devices at reasonable yield has not been accomplished. Integrated bipolar word switching strips involving smaller silicon area devices are being investigated as an alternative to MOS drivers.* These circuits would operate in the same fashion as the MOS circuits and would utilize an MOS address decoder. For either bipolar transistors or MOS transistors, laminates with 256×128 intersections, or preferably even larger, having conductors on uniform centers protruding from the edges of the laminate are required for realizing economic bit prices. For this reason, the program on pressure sintering of laminates is being actively pursued.

The laminates offer advantages for realizing large-capacity systems with respect to either plated wire or $2\frac{1}{2}$ D two-wire core systems. For the plated-wire memory, integration of the word addressing and driving circuitry is not as practical as for the laminates. The use of fully integrated digit sense circuitry places less of a premium on the $2\frac{1}{2}$ D organization possible with plated wire. In addition, this $2\frac{1}{2}$ D mode of operation for plated wire requires NDRO (non-destructive read out) operation with equal read and write currents. For a large-capacity memory system involving very long words, the NDRO sense signals are not expected to be of adequate amplitude to facilitate operation in a $2\frac{1}{2}$ D mode. Cryoelectric memories with technical performance characteristics that are competitive with magnetic memories for all capacity and cycle time ranges are expected to be more economic than magnetic memories for capacities as low as 10^7 bits and possibly even smaller.

At present the effort in laminates is restricted to investigating the technology for fabricating memory arrays with pressure sintering.

ACKNOWLEDGMENTS

A considerable portion of the work reviewed in this paper was conducted at the RCA Laboratories under the supervision of J. A. Rajchman, Staff Vice-President, Data Processing Research, RCA Laboratories. His many contributions to this program are greatly appreciated.

The RCA Memory Products Division, Needham Heights, Massachusetts, established a pilot operation for fabricating wafers and assembling stacks. The effort was under the supervision of H. Lemaire, Chief Engineer. The contributions of his staff greatly aided in devel-

* This work is being partially supported by NASA under Contract NAS12-574.

oping engineering solutions to the problems encountered on the program.

The advanced development laboratory of RCA Electronics Components, Somerville, New Jersey, developed the technology for fabricating integrated diode structures for addressing laminated memories. This effort was primarily directed by R. B. James. In addition they played an important role in developing integrated MOS circuits for laminated memories. Their contributions are greatly appreciated.

Systems evaluation of laminated memories was conducted with the Cooperation of the RCA Information Systems Division, Advanced Development Laboratories, Camden, New Jersey. The effort was under the supervision of J. A. Brustman. The contributions of his staff are appreciated.

AN MOS-TRANSISTOR-DRIVEN LAMINATED-FERRITE MEMORY

By

I. GORDON, R. L. HARVEY, H. I. MOSS, A. D. ROBBI, J. W. TUSKA,
J. T. WALLMARK, AND C. WENTWORTH

RCA Laboratories
Princeton, N. J.

Summary—Results are presented of an exploratory investigation of a large-capacity, random-access, magnetic memory combining the large-scale integration of arrays of MOS transistors and batch-fabricated laminated-ferrite memory planes. The ferrite used has the composition of $0.38\text{MgO}-0.19\text{MnO}-0.05\text{ZnO}-0.38\text{Fe}_2\text{O}_3$. The laminated-ferrite planes were fabricated by "doctor blading" and embossing. To circumvent difficulties in packaging because of shrinkage of the ferrite sheet ($\approx 17\%$) during firing, pressure sintering at 1000°C and 4000 psi (typical values) has been used.

A memory cross section consisting of a ferrite array with 256×100 crossovers and a word driver strip with 64 MOS transistors was assembled. On the basis of experimental tests it is judged that operation at 1.5 to 3.5 microseconds cycle time with two crossovers per bit and 2048 to 8192 words per sense amplifier/digit circuit is feasible. Extrapolation of the results to large-capacity memories with 10^7 bits per module is considered. Some of the difficulties in packaging and in yield are discussed.

INTRODUCTION

THE laminated-ferrite technique¹⁻⁷ has been developed to take advantage of integrated-circuit principles, i.e., the simultaneous fabrication of large numbers of memory elements. Because the

¹ R. Shahbender, C. Wentworth, K. Li, S. Hotchkiss, and J. A. Rajchman, "Laminated Ferrite Memory," *RCA Review*, Vol. 24, p. 705, Dec. 1963.

² R. Shahbender, C. Wentworth, K. Li, S. Hotchkiss, and J. A. Rajchman, "Laminated Ferrite Memory," *Proc. Intermag. Conf.*, p. 5-6-1 April 1964.

³ I. Abeyta, M. M. Kaufman, and P. Lawrence, "Monolithic Ferrite Memories," *RCA Review*, Vol. 27, p. 77, 1966.

⁴ M. M. Kaufman, R. L. Pryor, and A. Gilwitz, "Monolithic Ferrite-Integrated Storage Diode Memory," *Proc. International Solid State Circuit Conf.*, Phila., Pa., p. 98 Feb. 1966.

⁵ R. Shahbender, "Laminated Ferrite Memory, Phase I," Final Technical Report, Contract NASw-979, NASA CR-398, National Aeronautics and Space Administration, Washington, D.C., March 1966.

⁶ R. C. Ricci, P. J. Truscello, "A Monolithic Ferrite Space Memory," *Proc. National Electronics Conf.*, Chicago, Ill., p. 758, Oct. 1966.

⁷ R. L. Harvey, I. Gordon, A. D. Robbi, "Laminated Ferrite Memory—Phase II," Final Technical Rep., Contract NASw-979, National Aeronautics and Space Administration, Washington, D.C., Aug. 1966. ("Low Drive, Temperature Stable Ferrite for Laminated Memory Array," *IEEE Trans. Magnetics*, Vol. MAG-3, p. 526, 1967.)

H. I. Moss, A. D. Robbi, "High-Pressure Sintering of Ferrites," Final Rep., Contract DA36-039-AMC 037 19 (E), United States Army Electronics Command, Fort Monmouth, New Jersey, July 1967.

laminated ferrite offers a simple way of fabricating what amounts to very small magnetic "cores", all properly interconnected, it is possible to use very low drive currents compared to those used for conventional cores. Because the drive currents are very low, MOS transistor switches can be used for routing word current, digit current, and address selection. The bidirectional characteristics of the MOS transistors make possible certain simplifications in the driving circuits. At the same time, they are somewhat simpler to fabricate than bipolar transistors. For these reasons, it was decided to investigate the possibility of constructing a word-organized, large-capacity (10^7 bits), medium-speed

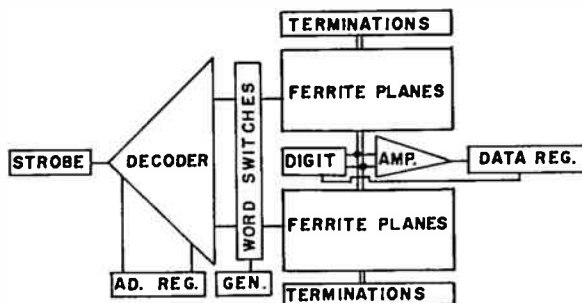


Fig. 1—Block diagram of memory system.

memory (2 microseconds cycle time).^{8,9} This paper reports the results of this investigation with respect to ferrite synthesis, ferrite plane fabrication, and systems design and testing.

The system organization is shown in Figure 1. The magnetic storage is divided into two parts to minimize the digit-sense electronics and the propagation delays and attenuation. MOS transistors have been used for memory address selection and for word and digit current switches. Word read-write currents are steered from a common bus to the selected word by an MOS switch.^{9,10} The switches are fabricated in integrated strips of 64 on 0.010-inch centers. The output terminal (drain) of each switch is connected to a grounded memory word line.

⁸ A. D. Robbi and J. W. Tuska, "Integrated MOS Transistor-Laminated Ferrite Memory," (Abstract), *IEEE Trans. Magnetics*, Vol. MAG-3, 1967, p. 329.

⁹ J. T. Wallmark, W. A. Bosenberg, E. C. Ross, D. Flatley, and H. Parker, "MOS Field-Effect Transistor Technology," Final Rep., Contract NAS 1-5794, National Aeronautics and Space Administration, Wash., D.C. Aug. 1967.

¹⁰ W. A. Bosenberg, D. W. Flatley, and J. T. Wallmark, "MOS Field-Effect Driver Strips for Laminated Ferrite Memories," to be published.

The switches are controlled by an MOS transistor quaternary tree decoder.¹¹ The decoder-tree branch selection is activated by the word-address register. A quaternary-based tree offers a reasonable compromise among the number of devices required, number of levels, integrated-circuit complexity, and ease of addressing. The unidirectional digit currents can be provided by scaled-down versions of the MOS word switches. A high-gain integrated bipolar transistor sense amplifier¹² converts the sense signal from the millivolt level to logic levels of about 1 volt.

For a 10^7 -bit module, the decoder tree would have 1024 outputs, each of which fans to 64 word switches. Word selection is accomplished by activating one of the 1024 decoder outputs and one of 64 word-current generators. This yields a module of 65,536 words. A 10^7 -bit module capacity would be achieved by utilizing a 150 to 200 bit memory word. The digit-sense system is segmented in blocks of 4096 or 8192 words, depending on the desired memory cycle time. Extrapolations from the data indicate that a cycle time of 2.3 or 3.5 microseconds is feasible.

A suggested approach to packaging¹³ is illustrated in Figure 2, which shows an exploded view of a representative subsystem. Each of the different components (laminated-ferrite array, word-driver strip, digit-driver strip, etc.) is mounted in an insulating frame with connection tabs (not shown) coming out through the sides of the frame. The frame consists of plastic molded in a form around the interconnecting metal fingers, or it may consist of Photoform glass. The metal connection tabs are fabricated in strips by photoresist techniques from 0.001-inch-thick copper. All interpackage connections are made on 0.010-inch centers using a solder reflow technique.

FERRITE COMPOSITION

To meet the requirements on the ferrite for this application, particularly operation at the relatively low drive currents available from MOS transistors and a temperature range of 0° to 50°C, a special ferrite (here called No. 47) was synthesized and produced in experimental quantities. In addition to good square-loop characteristics, the ferrite must meet the following requirements:

¹¹ J. T. Grabowski, "A 64 Output MOS selection Tree Using Large Scale Integration Technique," to be published.

¹² H. Beelitz, "A Monolithic Sense Amplifier," to be published.

¹³ J. P. Valentine and J. T. Wallmark, "Interconnection of Integrated Semiconductor Strips and Laminated Ferrite Arrays by an Impulse Solder Reflow Technique," to be published.

Remanent flux density ≥ 1000 gauss

$B_r/B_m \geq 0.9$

Switching coefficient, $S_{10} \leq 0.5$ oersted-microsecond

Coercive force, $H_c \leq 1.5$ oersted

Curie temperature, $T_c \geq 300^\circ\text{C}$

Grain size ≤ 10 micrometers

Resistivity $\geq 10^6$ ohm-cm

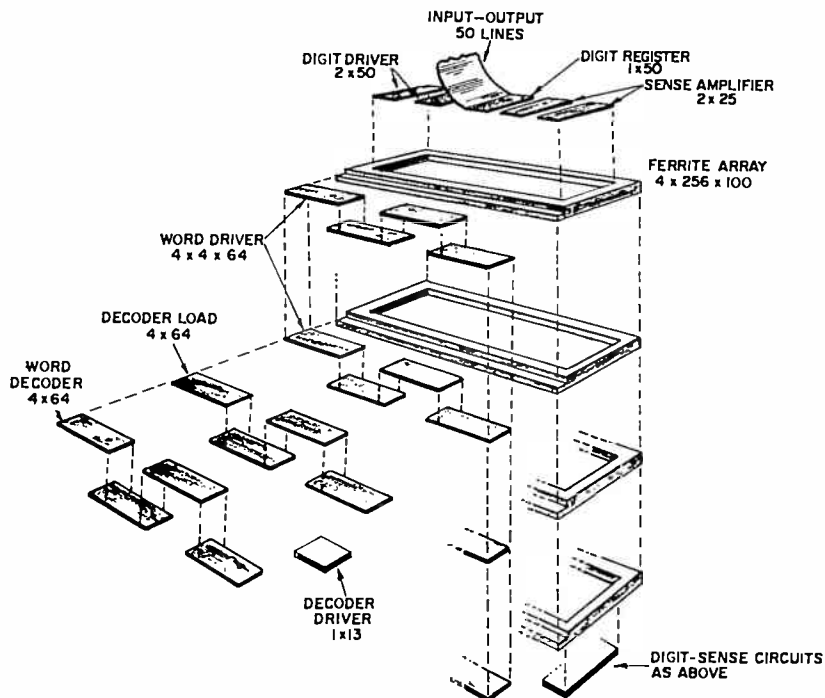


Fig. 2—Exploded view of a laminated-ferrite memory subsystem. Four ferrite planes, each containing 256 by 50 bits and associated circuitry, are shown.

The flux density, remanence ratio, Curie temperature, and switching coefficient parameters are normal requirements for memory applications. The remanence ratio B_r/B_m is the ratio of the remanence to the induction obtained by driving with a field five times the coercive force. The limitation on the coercivity for this application is imposed by the low drive currents. The Curie temperature value is established to assure adequate thermal stability. The need for a grain size restriction becomes clear when it is recalled that the laminate conductor planes are separated by a ferrite spacer that is 15 microns thick.

Were the grains allowed to grow to a size that spanned this gap, non-uniform operation of the array would result. It is the same small distance between conductor planes that makes necessary the imposition of the resistivity parameter. Troublesome leakage of pulses between conductor planes is avoided when the ferrite resistivity is maintained above 10^6 ohm-cm.

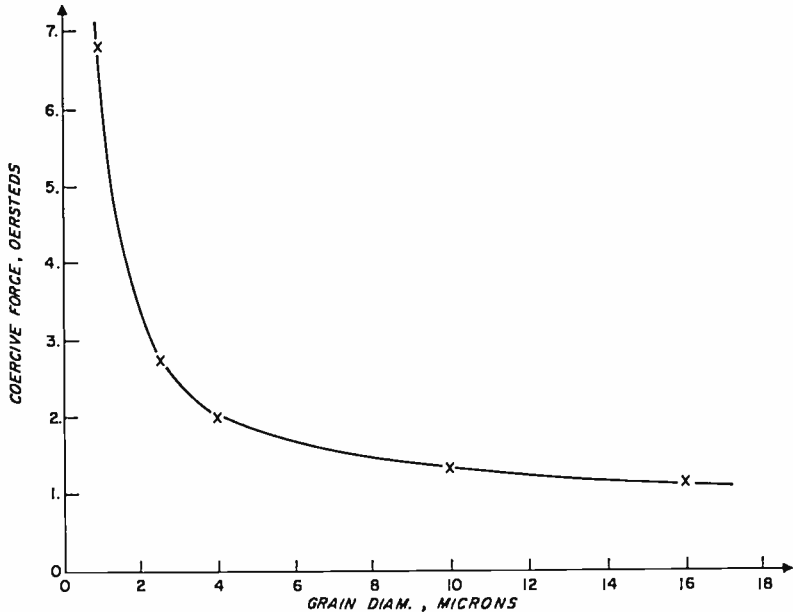


Fig. 3—Coercive force versus grain size for composition No. 47 ($0.38\text{MgO}-0.19\text{MnO}-0.05\text{ZnO}-0.38\text{Fe}_2\text{O}_3$).

The imposition of the grain size and resistivity parameters upon the more normal core requirements necessitated the developmental of a special ferrite composition. Certain of the prescribed parameters are mutually opposed—most importantly, the relationship between the coercive force and the grain size. For example, Figure 3 shows the observed dependence of coercive force on grain size for the preferred composition developed in this study. The grain size variation is the result of firing temperature. It is known that the coercive force decreases with increasing grain size over a substantial range of grain sizes.¹⁴

¹⁴L. Neel, "Properties of a Cubic Ferromagnetic of Fine Grains," *Comptes Rendus*, Vol. 224, p. 1488 (1947).

A number of compositional systems exhibiting square-loop characteristics were evaluated. To expedite the survey, a suitable binder was added to a portion of each composition prepared, and cores of 80 mils O.D., 50 mils I.D. were pressed and fired. All parameters of interest were measured using these test cores. When a composition appeared suitable, ferrite sheets were prepared, from which laminates and test toroids were fabricated.

Of the systems studied, the Mg-Mn-Zn ferrite system was found to have a region possessing a satisfactory compromise of all the desired characteristics. This region includes the composition $0.38\text{MgO}-0.19\text{MnO}-0.05\text{ZnO}-0.38\text{Fe}_2\text{O}_3$ referred to as composition No. 47, from which a number of planes were fabricated. In Table I, the core characteristics for Composition No. 47 are compared to the requirements listed above.

Table I

	Goal	Composition No. 47
Remanent flux density (gauss)	≥ 1000	1010
B_r/B_m	≥ 0.9	0.95
Switching coefficient (oersted-microseconds)	≤ 0.5	0.5
Coercive force (oersteds)	≤ 1.5	1.2
Curie temperature ($^{\circ}\text{C}$)	≥ 300	260
Grain size (microns)	≤ 10	< 10
Resistivity (ohm-cm)	$\geq 10^6$	2×10^7

Some performance values for laminates made from the preferred composition are given in Table II. The three laminates described differ in the temperature at which they were sintered. The test-core properties vary predictably; with increasing firing temperature, the grain size increases and the coercive force decreases. The effect of these changes may be correlated with the laminate operating characteristics. For the laminate fired at the lowest temperature, the write and digit currents (related to the coercive force) are all higher than for the laminate fired at a higher temperature. Since it is desired to reduce the magnitude of these parameters, a higher firing temperature is indicated. The laminate fired at the highest temperature, 1250°C , however, has an intolerable increase in grain size, which can be shown to produce nonuniformity of bit operation. Further, the back voltage has also increased to a higher value, acting to limit the word length that can be driven at a given voltage level.

Table II—Characteristics of Doctor-Bladed Ferrite Samples

	Samples		
	97F	97D	97B
Firing temperature (°C)	1200	1225	1250
H_r (oersted)	1.60	1.2	0.95
B_m (kilogauss)	1.44	1.01	1.08
B_r/B_m	0.79	0.95	0.92
Resistivity (ohm-cm)	3.2×10^7	2.2×10^7	7×10^8
Grain size (microns)	< 10	< 10	5 - 50
T_r (°C)	262	262	262
S_w (oersted-microseconds)	0.39/0.39	0.50/0.50	0.68/0.68
I_k (milliamperes)	100	85	90
I_n (milliamperes)	90	45	65
I_b (milliamperes)	± 12	± 10	± 10
Average signal (millivolts)	± 1.5	± 2.1	± 1.9
Back voltage (millivolts per bit)	9	8	27

The laminate fired at the intermediate temperature, 1225°C, results in optimized operation. The uniformity of operation of such a laminate is given by the histogram of Figure 4. Also, operation of this laminate does not vary appreciably with temperature, as shown in Figure 5. The reason for the upward slope of the curves is that the currents were optimized at 50°C. Higher digit and write currents at room temperature result in larger signals.

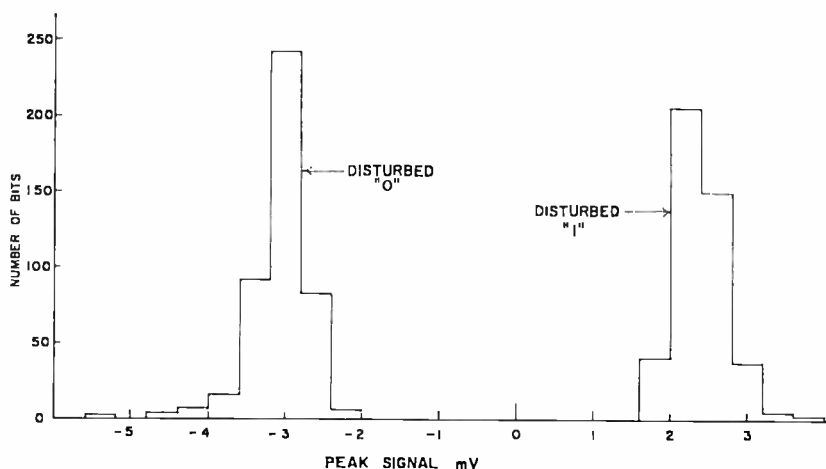


Fig. 4—Histogram for 448 scattered bits of laminate of composition No. 47 (one-crossover-per-bit operation).

LAMINATED-FERRITE PLANE FABRICATION

The laminated-ferrite planes contain 256 word and digit conductors on 0.010-inch centers. The overall thickness of the ferrite plane is 0.008 inch. The conductors have a cross section 0.0015×0.0025 inch and a resistance of 2.5 ohms per inch.

Ferrite-Powder Preparation

The constituents of the ferrite and methyl alcohol are placed in a steel mill and milled for two to three hours at 100 rpm. After milling,

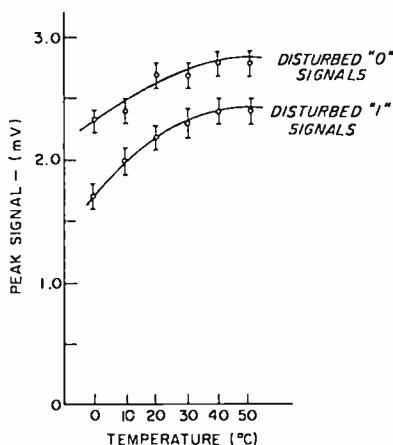


Fig. 5—Temperature stability of laminate operation without external compensation.

the mixture is dried at 150°C , passed through a coarse (4-mesh) screen, and placed in fire-clay crucibles for calcining. The material is heated to 900°C in 4 hours, held at this temperature for $2\frac{1}{2}$ hours, and is cooled with the kiln. The calcining atmosphere is air in a Globar kiln. The calcined powder is placed in the same mill used for mixing, methyl alcohol is added, and the mixture is again milled for 20 hours. After drying as before, the material is ready for use in preparing the blading slurry.

Ferrite-Slurry Preparation

A mixture of 640 grams of calcined ferrite, 44 grams of Butvar 76, 20 grams of Flexol D.O.P., 4 grams of Tergitol non-ionic TMN, and 480 ml of methyl ethyl ketone is placed in a mill identical to the mill used for mixing and grinding and is milled for 20 hours. After milling,

the slurry is put into a glass jar and rolled at 12 rpm until ready for use. This mixture is then used for doctor blading on silicone rubber. Slurries to be doctor-bladed on glass contain 580 ml of methyl ethyl ketone instead of 480 ml. Slurries are passed through a 200-mesh screen as they are loaded in front of the doctor blade to remove undissolved or unmixed clumps.

Ferrite-Sheet Manufacture

A ferrite sheet is made by drawing the doctor blade through a pool of slurry loaded in front of it as shown in Figure 6. The doctor blade has a smooth straight edge that can be set at any desired height above a suitable substrate surface. The height of the blade regulates the thickness of the ferrite slurry applied to the substrate. During drying, the adherence of the slurry to the substrate must be sufficient to prevent lateral shrinkage; all shrinkage should be vertical. Glass and silicone rubber have been found to be the most suitable substrates on which to doctor blade the film. Highly polished chromium surfaces are also satisfactory, but release of the film is more difficult. Thorough wetting of the dried film with water greatly facilitates release. The vertical drying shrinkage ranges from 5:2 to 7:1. Thus, to obtain a 3-mil-thick sheet, a doctor-blade setting of 15 to 20 mils must be used. The shrinkage depends upon the viscosity of the slurry and the speed of draw of the blade. The specific gravity of the doctor-bladed unfired sheet is about 2.8. During drying of the sheet, care must be taken to prevent drafts across the sheet. Drafts cause uneven drying and can cause the film to crack or craze. Drying should be slow enough to occur from the bottom to the top. If the top dries first, lateral shrinkage takes place on the surface causing peeling and crazing. Sheets thicker than 10 mils are not feasible due to the difficulty in drying the film slowly and uniformly. Thicker sheets can be made by laminating as many thin sheets as desired; blocks up to 1 inch thick have been made in this way.

Conductive-Line Fabrication

There are three methods of putting conductive lines in the ferrite: (1) to embed a solid wire, (2) to squeegee a conductive paste through a mask onto a flat surface and then doctor blade over the conductor pattern, and (3) to form grooves in the ferrite (embossing) and then fill with a conductive paste or powder. The material used for conductors must withstand ferrite firing temperatures and atmospheres. In most cases, this requires that platinum, palladium, rhodium, iridium, or

osmium be used. Gold is suitable for ferrites maturing below the melting point of gold.

Wires of platinum, palladium, or gold have been used. Shrinkage of the ferrite during firing (about 17% causes sufficient stress on the ferrite in the vicinity of the solid metal to crack the ferrite unless the ferrite wall is about ten times as thick as the diameter of the wire. If the ferrite is heavy enough not to crack, the compressive forces on the wire are sufficient to fracture the wire along slip planes in the metal. This has been shown by radiographs of such samples. In the case of gold conductors, the metal melts and then contracts into isolated segments along the line causing an open circuit. Gold-plated platinum, rhodium, and palladium wires have been used successfully. The gold melts, allowing the shrinking ferrite to slide along the wires. However, the mechanical problems involved in stretching many wires parallel seemed to make this method impractical.

In addition to its temperature characteristics, material No. 47 is unique among the materials used in fabricating laminated-ferrite memories in that usable magnetic properties can be obtained by firing entirely in nitrogen, air, carbon dioxide, or oxygen. The firing atmosphere has a considerable effect on the resistance of the embedded conductors. Different effects are observed for conductors of different materials. The two materials most commonly used are palladium and platinum. To achieve lowest conductor resistance a non-oxidizing atmosphere at temperatures below 800°C is required when palladium is used, and an oxidizing atmosphere is required until most of the firing shrinkage has been completed when platinum conductors are used. For materials other than No. 47, usable magnetic properties are obtained only when an oxidizing atmosphere is used, at least during the shrinkage phase. Since changing atmosphere complicates the firing schedule, No. 47 material is particularly desirable because it allows a wider range of firing atmospheres. If palladium conductors are used, the atmosphere should be CO₂ or N₂; if platinum is used, the atmosphere should be air or O₂. In either case, a nitrogen anneal during the cooling phase improves the loop squareness.

Pastes have been made of all suitable metallic powders. Patterns are photoetched in beryllium copper, stainless steel, or molybdenum masks. The paste is squeegeed through the masks onto a glass or silicone rubber substrate. Ferrite slurry is doctor-bladed over the conductor pattern. The dried ferrite film, which includes the conductive pattern, is then peeled off. This process is limited by the mechanics of the mask. Long, fine, closely spaced conductors are not feasible at the present state of the art. Masks with lines 3 inches long, 0.006 inch

wide on 0.018-inch centers are the longest that have been made and used successfully. In practice the masks are stretched tightly in a steel frame that straddles the glass substrate onto which the patterns are to be squeegeed. The frame and mask are held free above the glass surface by spring-loaded feet set into the frame. The entire assembly is located on a magnetic chuck which, when energized, pulls the steel frame and mask tightly against the glass substrate. Conductive paste is then forced through the mask by drawing a steel

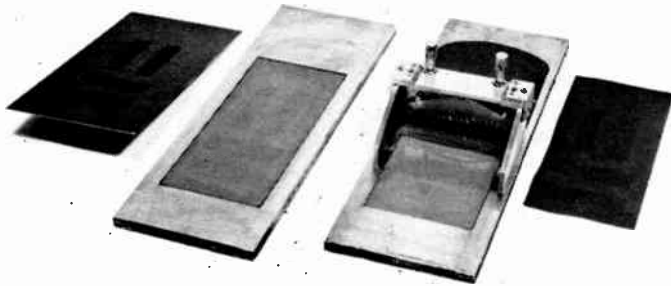


Fig. 6—Doctor-blading ferrite slurry over rubber masters to make grooved sheets. Shown, from left to right, are the lacquer master (positive), the rubber master (negative), the blading operation, and the finished grooved sheet.

straightedge loaded with the paste over the mask in a direction parallel to the mask openings. The mask is lifted vertically from the substrate by the spring-loaded feet when the chuck is de-energized. This leaves a clean pattern free of smears.

Grooves in the ferrite may be produced by machining the desired pattern in a lacquer phonograph record master (Figure 6). RTV60 silicone rubber is then cast over the master producing a male rubber master. Ferrite slurry is doctor bladed over the master, the dried film is peeled off, and the grooves are then filled with conductive powder.

Grooves may also be produced by embossing a plain unfired ferrite sheet. This is the preferred method. The embossing punch (Figure 7b) is made by electroplating nickel on a lacquer master (Figure 6). The nickel master is given a light chromium flash to facilitate removal of the embossed film. Prior to embossing, the embossing punch is coated with a 10% solution of Tergitol non-ionic TMN and dried. Referring to Figure 7, embossing is accomplished by loading the die (g) as fol-

lows: bottom punch (a), embossing punch (b), plain ferrite sheet (c), aluminum foil (d), rubber pad (e), and top punch (f). The loaded die is heated to 90°C and a pressure of 3000 psi is maintained for about 30 seconds. The die is immediately unloaded and the embossed sheet removed from the master by immersing in water and peeling. The grooves are then filled with conductive powder.

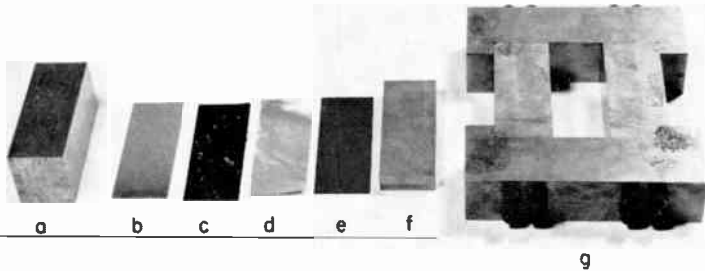


Fig. 7—Die and load to produce grooved ferrite sheet by embossing: (a) punch, (b) embossing punch, (c) ferrite sheet, (d) foil spacer, (e) rubber pressure pad, (f) punch, and (g) confining mold.

Laminating and Firing

All laminating is done in essentially the same way. The die (j in Figure 8) is filled in the following order: bottom punch (a), rubber pressure pad (b), aluminum foil (c), filled word-line sheet (d), blank spacer sheet (e), filled digit-line (f), aluminum foil (g), rubber pressure pad (h), and top punch (i). A pressure of 2000 psi is applied to the punches and the temperature is increased to 90°C. The stack is removed hot. All components are cooled before refilling.

Figure 9 shows a cross section of a laminate after firing. The light areas are conducting lines made by the embossing technique and consist of platinum. The line cross section is 0.0012×0.0024 inch. The trapezoidal shape is dictated by the procedure for grinding the cutting stylus used in producing the pattern on the lacquer phonograph record master.

Firing is done on flat-ground magnesium oxide setters. One green ferrite plane is placed between a pair of spaced setter plates. The

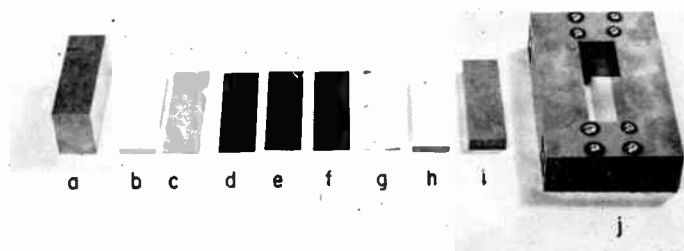
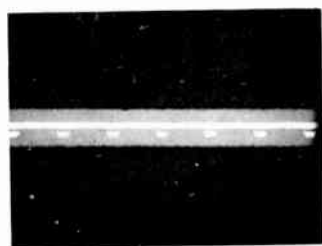
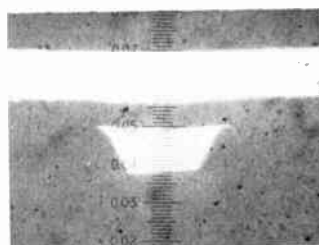


Fig. 8—Die and load for laminating green ferrite sheets: (a) punch, (b) rubber pressure pad, (c) foil spacer, (d) filled word-line ferrite sheet, (e) ferrite insulating sheet, (f) filled digit-line ferrite sheet, (g) foil spacer, (h) rubber pressure pad, (i) punch, and (j) confining mold.

spacing is about 0.002 inch greater than the thickness of the ferrite. This limits warping. The firing schedule is to go to 1260°C at 250°C per hour, hold 10 hours, and then cool with the kiln. The atmosphere is carbon dioxide. Annealing in nitrogen is preferred. The schedule for annealing is to go to 1120°C at the rate of 250°C per hour, hold 2 hours, and then cool with the kiln.



(a) DIGIT CONDUCTORS ARE ON 10 mil CENTERS



(b) SCALE: 0.0001 INCH PER SMALL DIVISION

Fig. 9—(a) Cross section of fired laminate with platinum conductors on 0.010-inch centers, (b) the same under larger magnification. Each small division on scale is 0.0001 inch.

PRESSURE SINTERING

The limitations inherent in the standard fabrication procedure of laminated-ferrite memory arrays may be eliminated to a considerable extent by use of pressure sintering. These limitations are that dimensional tolerances cannot be held to plus or minus 0.003 inch overall, usable magnetic properties cannot be produced at firing temperatures below 1150°C, and pre-fabricated conductors must be used. The dimensional tolerance is required to simplify interconnection problems, and lower firing temperatures are required to permit the use of conductive materials, such as gold, which reduce conductor resistance significantly below 2.5 ohms per inch. The use of solid gold, platinum, or palladium conductors in place of paste conductors would reduce the resistance by a factor of about 3. Briefly, the standard pressure-sintering process consists of applying pressure to the material (in powder or cold-pressed form) in a suitable die that is simultaneously heated to some optimum temperature for densification.

A major advantage of the pressure-sintering technique is that by proper selection of starting material, particle size, and processing parameters (i.e., temperature, pressure, and time), very high relative densities can be obtained at temperatures much below the conventional pressureless sintering techniques. In addition, pressure sintering permits the attainment of an increased rate of densification when compared with conventional sintering practices.

Microstructural control is another advantage inherent in the pressure-sintering technique. With proper selection of the pressure-sintering parameters, as mentioned above, high relative density can be obtained with a minimum of grain growth. Similarly, controlled levels of porosity can also be achieved.

Application of pressure during the sintering of laminated arrays can serve to neutralize the effect of firing shrinkage that would normally occur during conventional sintering. With solid conductors embedded in the ferrite, good interfacial contact can be maintained because of the applied pressure, even though shrinkage does take place in the pressing direction. Shrinkage in directions perpendicular to the pressing direction is neutralized by the application of pressure.

Pressure-Sintering Apparatus

A schematic diagram of the pressure-sintering chamber is shown in Figure 10. This chamber is designed to be evacuated to eliminate adsorbed gases in the pressed compacts.

Dies and rams are constructed of a molybdenum alloy and are heated

by means of a molybdenum-wound resistance furnace. The die is lined with a tight-fitting cylindrical graphite insert that has an inside diameter of 0.5 inch. The inside of the graphite insert is lined with a 0.002-inch-thick platinum sheet to separate the ferrite from the graph-

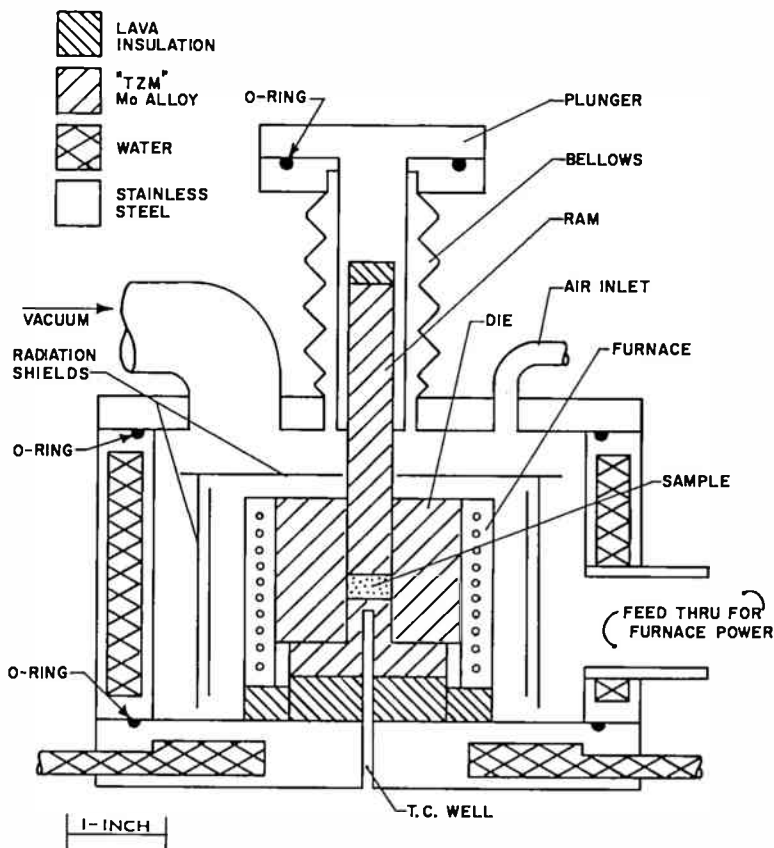


Fig. 10—Schematic view of pressure-sintering chamber.

ite and thereby prevent ferrite reduction. At the completion of an experiment, the sintered ferrite and its platinum container are easily pushed out from the graphite. To prevent any reaction between the ferrite and the rams, 0.002-inch-thick iridium disks are inserted between the ferrite and the ram faces.

Temperature is determined and controlled by means of a Pt-Pt13% Rh thermocouple that protrudes into the bottom ram to a point $\frac{1}{8}$ inch below the powder compact. Temperatures are controlled to $\pm 3^\circ\text{C}$ during an experiment. Uniaxial pressure is maintained during experi-

ments to within $\pm 12\%$ at the lowest pressure used in this work and to within $\pm 1\%$ at the highest pressure. A solid-state load cell situated in the pressure train gives continuous indication of applied force.

A linear differential transformer is used to measure small displacements of the bottom platen of the press. The output from this device is recorded continuously. In this manner, a record of linear shrinkage, at constant temperature and applied pressure, is obtained as a function of time. This record, together with the final sample height and the final bulk density, permits the calculation of the sample bulk density at any time during the experiment. Plots of relative density as a function of time are constructed from this information.

Materials and Procedures

The composition of the material used for most of the pressure-sintering experiments, which is somewhat different from material No. 47, was 12.5 mole % ZnO, 25.5 mole % MgO, 22 mole % MnO, and 40 mole % Fe_2O_3 . It is expected that No. 47 would behave similarly with minor process modifications. After a low-temperature calcine and subsequent milling, the powder was fired at 1150°C in air for two hours. The fired material was then milled in water for 50 hours to produce a ferrite powder with a particle size of about 0.5 micron.

An x-ray diffractometer trace was obtained from the fired and milled powder. The trace showed the powder to be single-phase spinel with a lattice constant of 8.420 Å. The theoretical density of the ferrite, on the basis of this lattice constant, is 4.812 grams/cm³.

The die was subjected to the action of a vibrating table after loading to ensure uniform packing of the powder and a level surface. Sufficient powder was used to provide a sintered specimen 0.120 to 0.150 inch high. The pressure-sintering chamber was evacuated for at least 16 hours while the ferrite was held at a temperature of 600°C . This served to expel adsorbed gases and moisture from the powder. The powder was then pressed for 2 minutes at a pressure of 12,000 psi. This pressure was released, and the temperature of the die and its contents was increased to the desired level. The rate of heating from 600°C to the temperature of the experiment was about $25^\circ\text{C}/\text{minute}$. A 5-minute soak period at temperature permitted equilibration to take place. Pressure was then applied, full pressure being achieved in about 5 seconds, for a period of one hour. At the end of a run, the pressure was released, the power to the furnace was reduced, and the die was cooled rapidly to 900°C and then at a rate of 5°C per minute to 500°C , at which point the furnace was turned off. Temperatures used in this study were: 850, 900, 950, 1000, 1050, and 1100°C . The pressures were

1000, 2000, 4000, 8000, and 12,000 psi. Not all temperature-pressure combinations were used, since some combinations would produce exceedingly low-density specimens.

Ring-shaped test specimens were ultrasonically cut from the sintered compacts. These cores had the following average dimensions: 0.1220-inch outer diameter, 0.0725-inch inner diameter, and 0.020-inch thickness. The dimensions of all the cores studied were within $\pm 3\%$ of the above values.

All specimens were subsequently annealed. Four cores from each temperature-pressure combination used for pressure sintering were first annealed in air for 6 hours at temperatures of 1000, 1050, 1100, and 1150°C, respectively. This was followed by a 2-hour anneal at 900°C in an N_2 atmosphere. The cores were then allowed to cool naturally in N_2 in the furnace at a rate of about 5°C/minute. Those with a pre-annealed density of less than 90% of theoretical exhibited some shrinkage during the higher-temperature anneals. This shrinkage, however, never amounted to more than 3% of the average dimensions given above.

Testing and Evaluation

Bulk densities of the pressure-sintered samples were calculated from their weight and volume, the latter being determined by a displacement method. The maximum error in the density determination is estimated to be $\pm 0.1\%$.

Annealed and pre-annealed pieces of ferrite were examined microscopically. Photomicrographs were taken so that the grain structure, size, and size distribution could be studied. Grain size was determined by the line intercept method. A correction factor of 1.5 was used to correct the average dimension, as measured across a randomly cut grain, to give the maximum diameter of the grain.¹⁵

A two-terminal method using silver-paste electrodes on the annealed cores was employed to determine the resistivity with an electrometer.

The cores were used to obtain dynamic hysteresis-loop data with a drive frequency of 400 Hz. The applied drive was approximately twice the coercivity. Static hysteresis-loop data also were obtained on several cores with special 50-turn windings. The static loops are more accurate because of the use of a chart recorder for displaying the loops and the elimination of phasing adjustments associated with the dy-

¹⁵ R. L. Coble, "Sintering Crystalline Solids: II, " *Jour. Appl. Phys.*, Vol. 32, p. 793 (1961).

dynamic method. For this reason, the 400-Hz loop equipment was calibrated against the static equipment. Values for the coercive force (H_c) and remanent flux density (B_r) were obtained from the dynamic loops. The maximum error in these measurements is estimated to be $\pm 10\%$.

The switching coefficient was measured for selected cores that exhibited good squareness. This measurement has been described elsewhere.⁷

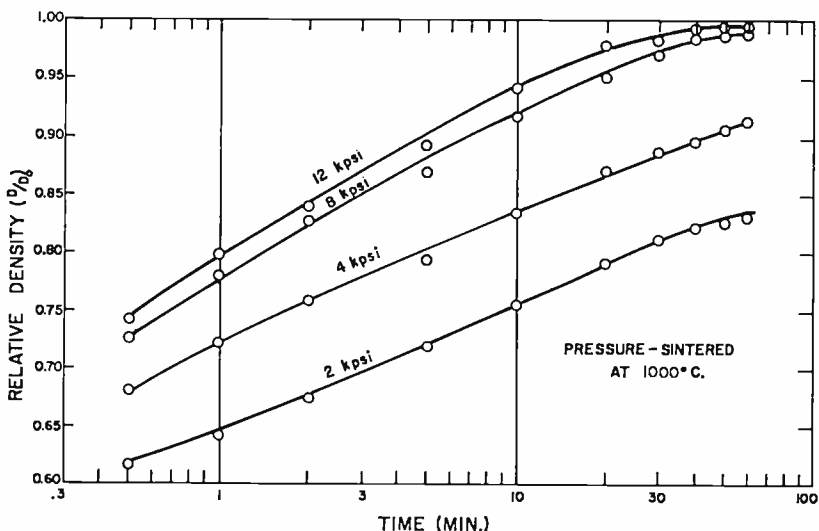


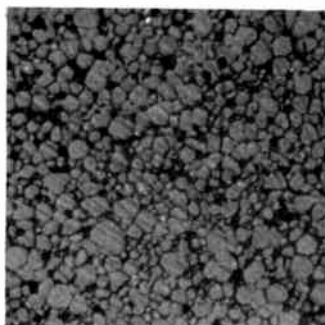
Fig. 11—Relative density versus time for Mg-Mn-Zn ferrite pressure sintered at 1000°C and 2000, 4000, 8000, and 12000 psi.

Density and Microstructure

Densities of the pre-annealed specimens prepared by pressure sintering for a period of 60 minutes at various temperatures and pressures ranged from 82 to 99.8% of theoretical. Typical densification curves for the Mg-Mn-Zn ferrite composition specified previously are shown in Figure 11. These curves show the pressure-time options that are available to obtain a particular density. For example, at 1000°C, a relative density of 0.9 can be achieved in approximately 5 minutes at 12,000 psi, 7 minutes at 8000 psi, or 40 minutes at 4000 psi. Pressing at a higher temperature will result in a larger grain size. However, for the same amount of applied pressure, a shorter time could suffice at the higher temperature, thus limiting the grain growth.

Microscopic observations of the pressure-sintered ferrites both before and after annealing showed the microstructure to consist of

equiaxed grains, i.e., grains that have approximately equal dimensions in the three coordinate directions. The average grain diameter of the pre-annealed specimens ranged from about 0.6 micron at the lowest pressure-sintering temperature to 1.7 microns at the highest temperature. The grain size of the annealed samples ranged from about 1 micron at the 1000°C anneal up to 6 microns at the 1150°C anneal. The greater the density of the sample before annealing at a particular temperature, the larger the grain size after annealing.



10 μ

Fig. 12—Photomicrograph of pressure-sintered Mg-Mn-Zn ferrite: temperature-1000°C, pressure-4000 psi, and anneal-1100°C.

Porosity levels in these specimens are probably influenced to only a very slight extent by gases entrapped within pores of the compact during the pressure-sintering operation. This is due to the vacuum conditions under which the powder is baked prior to densification and the maintenance of a vacuum during pressure sintering.

Figure 12 shows a photomicrograph of a polished and etched specimen. This specimen was pressure sintered at 1000°C, 4000 psi, for 60 minutes, and subsequently annealed at 1100°C.

Electrical and Magnetic Properties

The resistivity of ferrite samples annealed at 1000, 1050, and 1100°C is about 1×10^7 ohm-cm at room temperature. Resistivity decreases slightly as the annealing temperature increases. Samples annealed at 1150°C usually show an even lower resistivity, sometimes by as much as a factor of 10.

Figure 13 shows a typical dynamic hysteresis loop taken on the sample whose microstructure is shown in Figure 12. This loop exhibits good rectangular properties and also has fairly sharp knees.

Coercive force H_c ranged from a high of 3.2 oersteds to a low of 0.9 oersted and depends more on the anneal temperature than on the

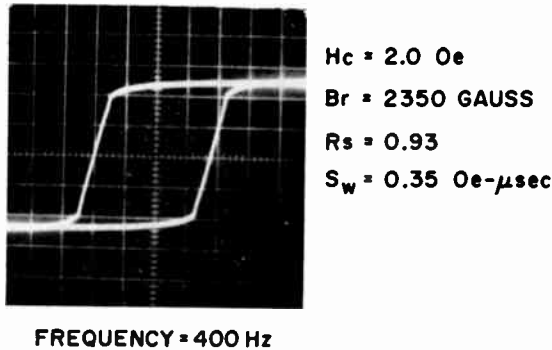


Fig. 13—Dynamic hysteresis loop of pressure-sintered Mg-Mn-Zn ferrite: temperature-1000°C, pressure-4000 psi, and anneal-1100°C.

pressure-sintering parameters. The coercive-force values were grouped according to the anneal temperature as follows:

Anneal Temperature (°C)	H_c (oersted)
1000	2.2 to 3.2
1050	2.2 to 2.5
1100	1.5 to 2.2
1150	0.91 to 1.7

This grouping is probably due to the more or less uniform grain size present at each anneal level. As expected, the coercive force is inversely proportional to grain size. H_c is also dependent on density. An increase in density (higher pressure) results in a slight decrease in coercive force. However, the increase of grain size with density, as pointed out above, masks the actual magnitude of the decrease of H_c . Coercive-force values obtained in this study are comparable to values obtained by conventional sintering methods. Laminated-ferrite memory arrays fabricated from ferrite compositions similar to the composition used in this work range from 1 to 2 oersted.^{1,5}

Values of remanent flux density B_r range from a low of 780 gauss

to a high of 2880 gauss and also fall into groupings that depend on the particular anneal temperature. The higher the anneal temperature of a particular set of pressure-sintering conditions, the higher the remanent flux density. In addition, there is some dependence of B_r on the sample density; an increase in density results in an increase in B_r .

The loop-squareness values obtained in this work were determined by combining dynamic-loop and pulse data and are, in general, quite high. Squareness, R_s , ranged from a low of 0.72 to a high of 0.98.

The switching coefficient S_w was measured for certain selected cores that appeared to have useful values of H_c and R_s . The values range from 0.32 to 0.58 oersted-microsecond. The S_w appears to increase at the highest anneal temperature where grain growth becomes significant. Also lower values of S_w are evident for the more porous specimens. Values of S_w obtained from measurements of ferrite laminates prepared in the conventional fashion are between 0.3 and 0.4 oersted-microsecond.^{1,5}

TEST-VEHICLE PERFORMANCE

This section summarizes the operation of a test vehicle combining a No. 47 laminated-ferrite memory plane with 256×100 crossovers on 0.01-inch centers and a simulated MOS transistor switch strip. The simulated switch strip consists of sixteen 10-lead sockets, partially populated with encapsulated MOS switch transistors. The transistors used are sections (4 drain contacts, 4 gate contacts, common source, and substrate) of integrated 64-switch strips. A complete frame-mounted 64-switch strip is shown connected to a laminated-ferrite 256×100 plane in Figure 14.

Ferrite-Plane Characteristics

The planes are operable with low word read-write currents (approximately 100 milliamperes for read and 60-70 milliamperes for write). With a read-current rise time of 0.2 microsecond, the typical disturb sense signal peaks at approximately ± 2 millivolts for binary "1" and "0", respectively. The word back voltage peaks at approximately 20 millivolts per crossover (40 millivolts per bit). The effect of read-current rise time on sense-signal amplitude is shown in Figure 15. The sense signal begins to fall off rapidly at a rise time greater than 0.3 microsecond. For this particular plane the optimum signal-to-back-voltage ratio occurs at a rise time of 0.2 to 0.4 microsecond. In low-power operation, the limitation of word-current amplitude imposed by the electronics causes the ferrite switching time to be more dependent on current amplitude than on rise time.

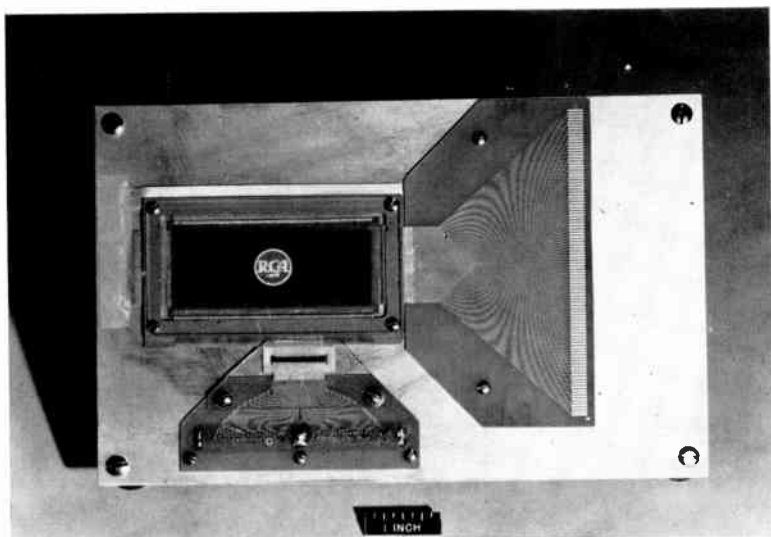


Fig. 14—Frame-mounted 256×100 crossover laminated-ferrite memory plane with integrated 64 MOS transistor switch strip.

MOS-Switch Characteristics

The MOS transistor is basically a three-terminal device with the gate voltage governing the conductance between source and drain. The source and drain terminals are similar and may be interchanged electrically. Furthermore since the MOS conducts equally well for both

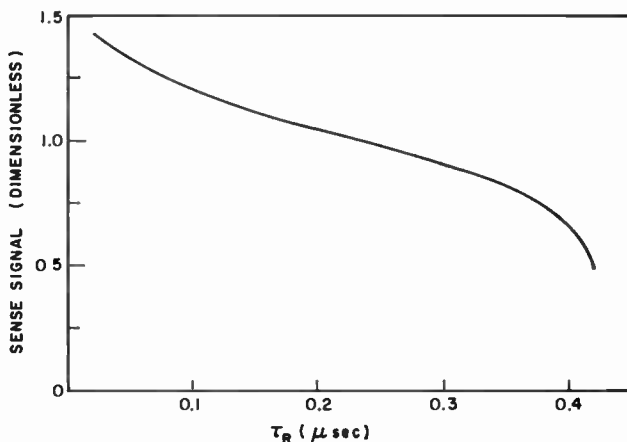


Fig. 15—Dependence of normalized signal amplitude on read-current rise time (normalized at 0.25 microsecond rise time).

current polarities, a single switch is capable of supplying the negative read current and positive write current. The I - V characteristics for a typical MOS transistor used in the test vehicle are shown in Figure 16.

For optimum memory performance, the write-current amplitude is approximately 60% of that of the read current. In the third quadrant in Figure 16, the channel conductance is increased by the voltage be-

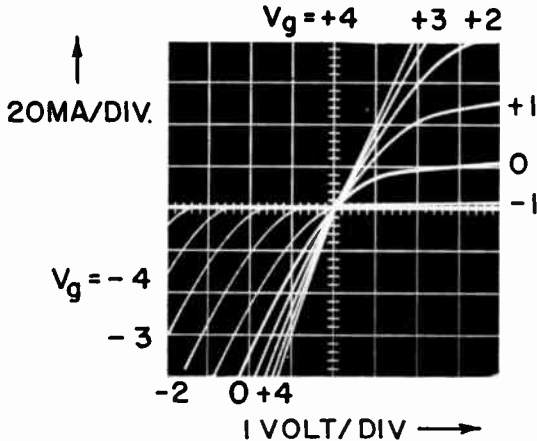


Fig. 16— V - I characteristics of MOS switch. Test conditions: with drain grounded and substrate at -9 volts, the source is swept negative to positive with the gate stepped from -8 to $+4$ in 1-volt steps.

tween source and drain in addition to the gate-bias voltage. For this reason, the greater current requirement of the read pulse is satisfied with a lower gate pulse voltage if the read current is negative.

The integrated MOS transistor word-switch strips measure approximately 0.7×0.1 inch. The source and drain contacts are n-type diffusions in p-p⁺ epitaxial wafers. Reverse-biased junction capacitance is $10 \mu\text{F}$ under operating conditions. The effective channel area per switch is 0.108×0.0002 -inch, with a gate capacitance of $20 \mu\text{F}$. The switch transistors are fabricated with the source terminal of each switch connected to a common bus.

Test Vehicle

The electrical connections for the test vehicle are shown in Figure 17. The MOS transistor word switches are held nonconducting by a negative gate bias applied to the MOS gate through a 10,000-ohm resistor. In cases of gate leakage or failure, the resistor functions as a current limiter and facilitates the identification of the faulty gate. Selection of an individual MOS switch is by application of a positive

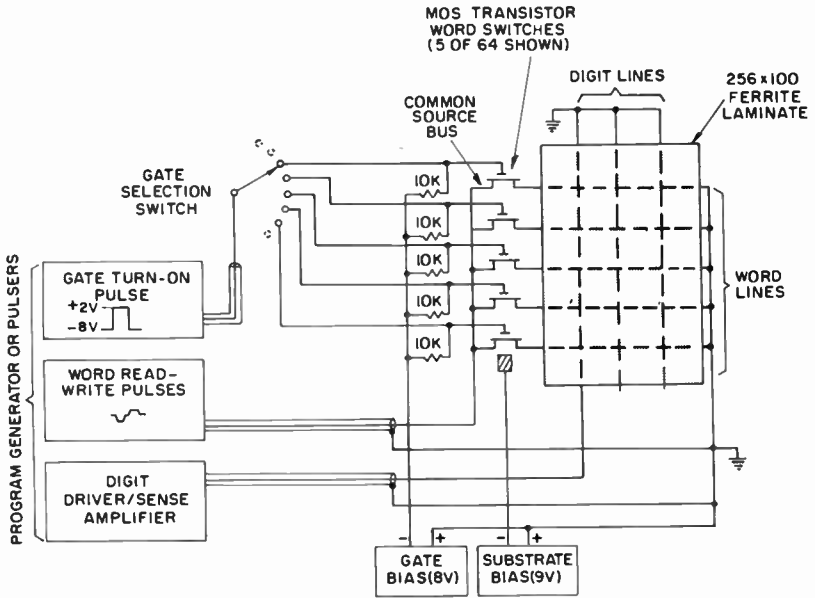


Fig. 17—Test-vehicle circuit diagram.

pulse whose amplitude is 10 volts above the 8-volt negative bias. The substrate is biased at -9 volts to isolate the drain junctions and minimize the junction capacitance. Implementation of the gate selection switch, shown in Figure 17, for the tests described is an electronically driven reed relay tree.

The 0.2-microsecond rise time of the gate pulse controls the word read-current rise time, and the fall time of the gate pulse controls the fall time of the word write current. Figure 18 illustrates the timing

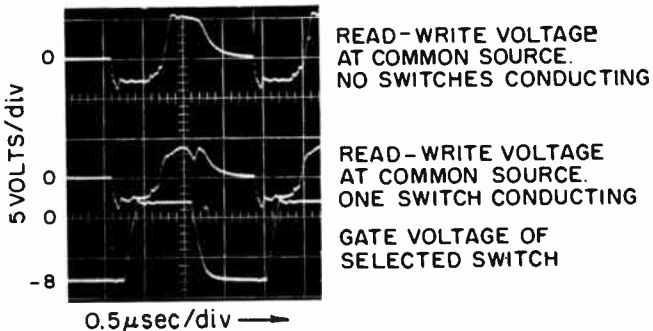


Fig. 18—Voltage waveforms for MOS-transistor word switch showing relative timing.

and voltage levels of the gate and read-write voltages applied to the MOS transistor switches. The -8 volt bias is ample to maintain the switch in a nonconducting state for the source voltage shown in Figure 18. The gate-pulse amplitude controls primarily the amplitude of the positive write current. The read-current amplitude is controlled by adjustment of the negative voltage level of the generator.

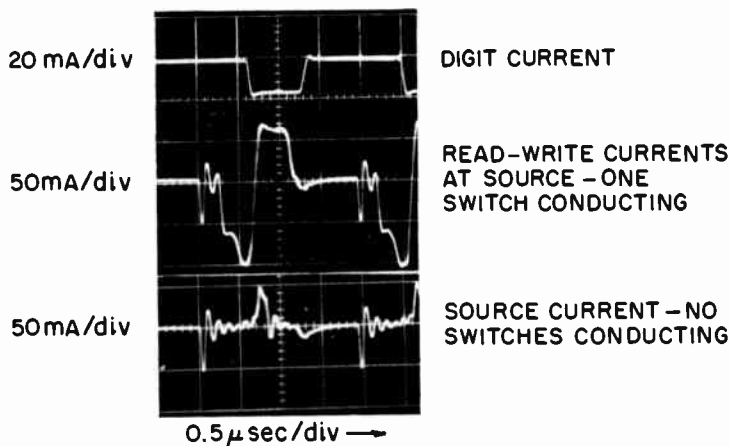


Fig. 19—System current waveforms.

The center trace of Figure 19 shows a typical source current resulting from the conduction of a single MOS switch under the voltage level conditions discussed above. The lower trace shows the capacitive charging currents resulting from the application of the generator voltages without switch conduction. Thus, the memory word-current waveform is the difference between those two traces. Peak word currents delivered to the memory plane by the 42 operable MOS switches in the test vehicle are given in Figure 20 in the form of a histogram quantized to the nearest 5 milliamperes. Variations in the currents are indicative of variation in the MOS switch terminal characteristics rather than nonuniformity of the laminate. The uniformity of the write currents is attributable to the negative feedback resulting from an increasing word-line back voltage dropping the source-drain voltage. The increasing back voltage also decreases the gate field. Both these effects reduce channel conductance. For the read current, only the reduction in source-drain voltage occurs, and the negative feedback is less effective in controlling current, as can be seen in Figure 20.

For memory operation, digit currents overlap the write current in time as indicated in the upper trace of Figure 19. The digit current

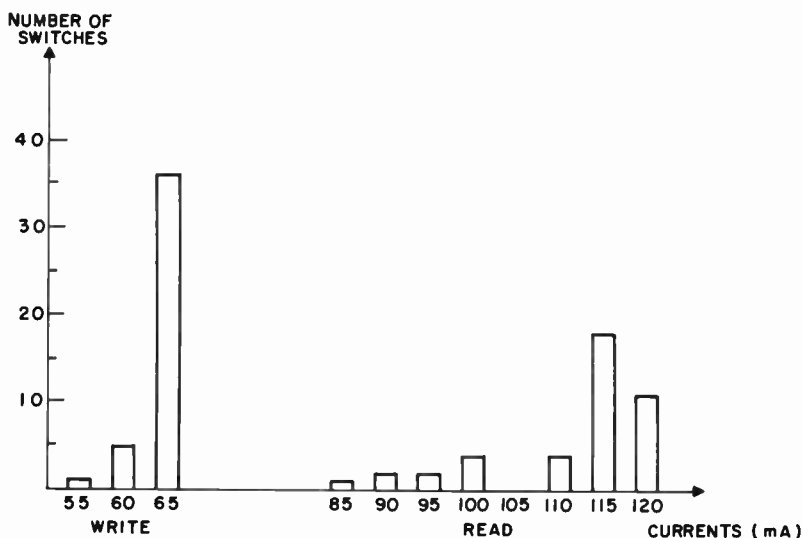


Fig. 20—Word-current uniformity.

is held constant at 16 milliamperes for all the data to follow. The test program of memory currents for two-crossovers-per-bit operation is shown in Figure 21. The system is operated in a unipolar-digit, two-

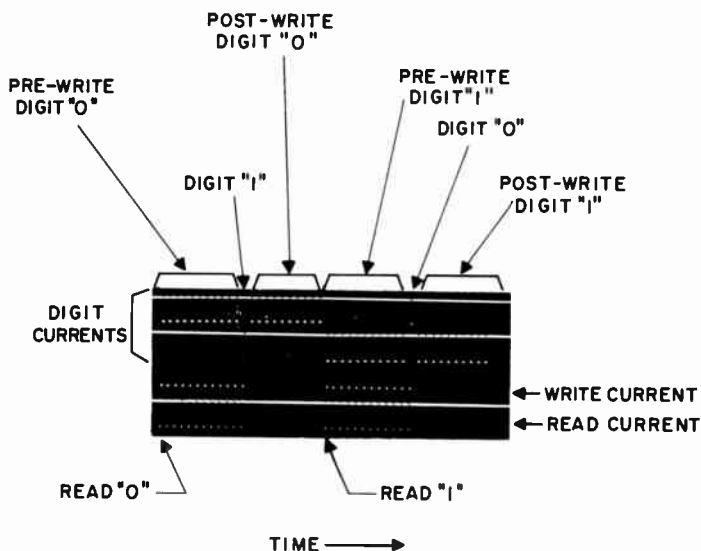


Fig. 21—Pulse program for 2-crossovers-per-bit memory operation.

crossovers-per-bit mode. In this mode, two adjacent digit lines are used to store one bit of information. The sense signal is the differential voltage between the two lines, resulting in cancellation of common inductive and capacitive noise. The capacitive noise is negligible at long rise time, so the benefit of this mode of operation is the cancellation of inductive noise. To store a binary "1", a negative digit current pulse is applied to one line of the pair; to store a "0", the other line is pulsed. Read and write currents occur as pairs as shown in Figure 19. The program yields pre- and post-disturbed output signals. The number of disturbs shown in Figure 19 was limited for convenience. The validity of the data has been verified for as many as 10^6 disturb pulses.

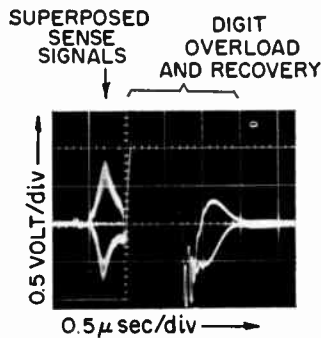


Fig. 22—Superposed amplified sense signals (29 words by one bit).

A reed relay tree is used for gate selection, and the program shown in Figure 21 is applied in time sequence to each of 29 different memory words (the tree scanned 32 MOS switches of which 29 were operable). Superposed "1" and "0" amplified sense signals from a typical bit location are shown in Figure 22. The amplifier is an integrated-circuit differential amplifier (TA 5196) specially designed for use in a medium-speed large-capacity memory.¹² The signals shown are taken from the output of the linear section (voltage gain of approximately 300). A positive signal is defined as a binary "1" and a negative as a binary "0". The extremes of the unamplified "1" and "0" peak signals for every usable digit location are plotted in Figure 23. Digit pairs (1, 2), and (49, 50) are edge pairs and are not usable in a memory system because of their differing transmission characteristics. There is a signal window of 1.5 millivolts between the minimum "1" and the minimum "0" signal, with the digit lines grounded.

Operation using one crossover per bit is also possible. In this mode a negative digit current writes a binary "1" and a positive digit current

writes a "0". Under the same test conditions as above (except for the digitizing technique), the signal window for a cross section of the memory bits is 0.8 millivolt. To make this mode of operation practical requires improved magnetic uniformity. The benefit would be a doubling of the bit-packing density.

When driving the common source bus of the MOS switching strip the load is essentially capacitive. It includes 640 pF resulting from

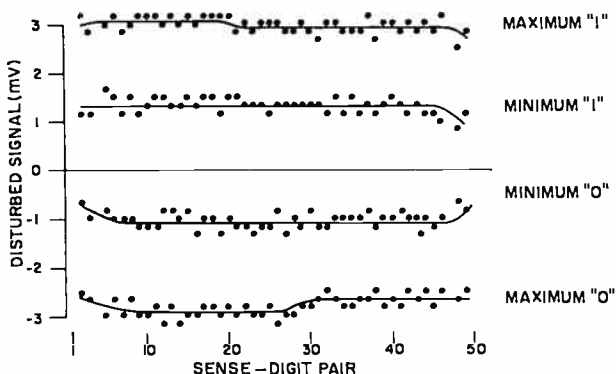


Fig. 23—Sense-signal extrema for 2-crossovers-per-bit operation of test vehicle.

the 64 reverse-biased source junctions and approximately 200 pF attributable to the source interconnection bus and end-terminal connections. A full memory plane of 1024 words requires 16 such switching strips. The total capacitive loading on the read-write current generator for the proposed system is then approximately 0.013 microfarad. A simulation of this system for the word current and voltage swings previously discussed resulted in a maximum charging current of 450 milliamperes.

An investigation of the allowable margins for the test vehicle confirmed that tight tolerances are not required for the currents and voltage levels of the memory. The test results are:

- (1) $\pm 10\%$ changes in digit current about the optimum value result in a 10% reduction in signal.
- (2) $\pm 10\%$ variation of the gate quiescent voltage has no effect on memory operation.
- (3) $\pm 10\%$ change in the magnitude of the gate turn-on pulse produced a 10% change in the signal window.
- (4) Varying the substrate bias from -7 to -9 volts has no effect.
- (5) $\pm 10\%$ change in source voltage leads to an $\pm 8\%$ change in read current and a $\pm 5\%$ change in write current as can be seen from

the MOS I - V characteristics of Figure 16. These current changes lead to slightly smaller changes in signal.

Transmission Properties

The maximum number of bits that can be serviced by a single sense-digit circuit (see Figure 1) is a function of the delay, attenua-

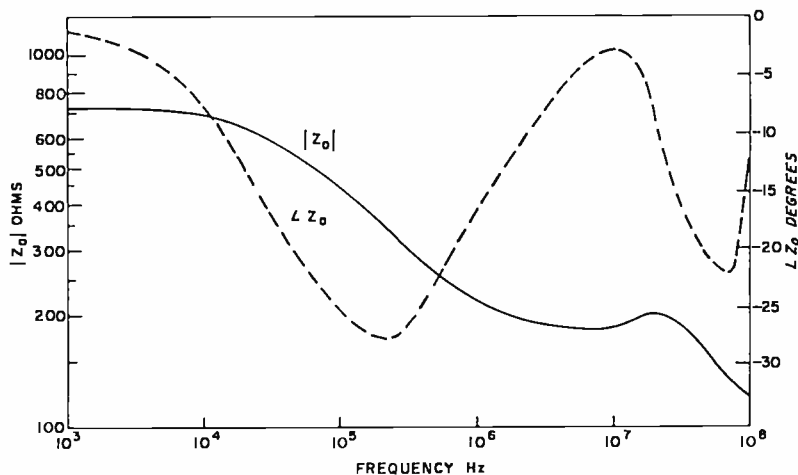


Fig. 24—Magnitude and phase of characteristic impedance of laminated-ferrite sense digit line as a function of frequency.

tion, and matching of line impedance by the terminations. The prediction of that number is complicated by the fact that the ferrite medium has frequency sensitive properties in the frequency spectrum of interest for a medium-speed mass memory.

Measurements of the characteristic impedance using the 256×100 crossover laminated-ferrite plane previously described were obtained using impedance bridges. The magnitude and angle of the characteristic impedance as a function of frequency are shown in Figure 24. The frequency dependence is attributable in part to the fact that this line is not distortionless, i.e., r/l is not equal to g/c where r , l , g , and c are the small-signal resistance, inductance, conductance, and capacitance, respectively. The frequency dependence of the small-signal parameters also contributes to the nonlinearity, particularly above 10 MHz. In general as frequency increases r and g increase, while l and c decrease.

On the basis of the impedance measurements, the attenuation and delay have been computed. Termination of the lines, as shown in Figure 1, reduces the signal by 6 dB. In addition, the lossy line con-

Table III—Attenuation and Delay at Selected Frequencies

Frequency (Hz)	α (dB/1024 words)	τ_d (n sec/1024 words)
10^5	0.015	57
10^6	0.030	33
5×10^6	0.038	29
10^7	0.047	32
2×10^7	0.158	43

tributes a component, α , that increases with frequency. The delay τ_d is also frequency dependent. The highlights of this data are presented in Table III.

The attenuation curve has a break frequency at 15 MHz; from 20 to 100 MHz, the attenuation increases at the rate of 1.32 dB/decade/1024 words. For a memory application where the generated sense signal has a base width of 0.2 microsecond, more than 90% of its energy lies below 10 MHz: at 0.3 microsecond base width, the corresponding frequency is less than 7 MHz. The essentials of the above data have been confirmed by pulse measurements on other laminated-ferrite planes.¹⁶

Given the organization of Figure 1, the transmission properties discussed above lead to the systems parameters listed in Table IV for 4096 and 8192 words/sense amplifier.

The signal reduction in a system of this size is not sensitive to the attenuation of the line itself, but is caused by the necessity to terminate to achieve reasonable cycle times. The major contribution to cycle time is the decay of digit noise from the write operation. The length of the decay is a function of how well the line is terminated and the transit time of reflected waves between terminations. The recovery shown in

Table IV—Extrapolated System Characteristics

	Number of Words	
	4096	8192
Worst-case signal reduction (dB)	6.1	6.2
Delay, amplifier to termination (nanosecond)	65	130
Read/write current duration (microsecond)	1.0	1.0
Recovery of line after digit (microsecond)	1.3	2.5
Read/write cycle estimate (microsecond)	2.3	3.5

¹⁶J. P. Gray, private communication.

Table IV assumed 200-ohm resistive terminations. The cycle times shown do not include certain "housekeeping" functions such as decoding and setting registers because these can be performed in parallel, for example during the decay of digit noise.

CONCLUSIONS

Extrapolations from test-vehicle operation and transmission data substantiate the feasibility of constructing a 10^7 bit random-access memory from low-drive laminated ferrites and MOS integrated-switches. The 0.010-inch center-to-center spacing in both the laminated ferrite and in the integrated arrays of MOS switches results in a compact assembly. The economical construction of 10^7 -bit modules will necessitate the development of an automated interconnection technique. The fabrication of monolithic arrays by pressure sintering will facilitate interconnections, because it is expected that solid leads will protrude from the memory planes at exact center-to-center distances. Further, the use of solid conductors in the arrays will lead to improved transmission properties, permitting shorter memory read-write cycle times. The packaging of the semiconductor devices requires hermetic sealing, which has not yet been attempted, and failures of MOS switches were experienced because of interaction of the frame plastic with the gate insulator. Whether the large gate area required for the MOS transistor could be fabricated with sufficient yield in practice is not now clear. An alternative solution employing integrated pairs of bipolar transistors is now being investigated.

In essence, the technical feasibility of a large capacity, low-power, and compact memory made of fully integrated magnetic and semiconductor structures, has been demonstrated. However, a great deal more work remains in evaluating the economics of the laminate technology with respect to other magnetic approaches, and in maximizing its relative advantages.

ACKNOWLEDGMENTS

The work reported here has been supported in part by the National Aeronautics and Space Administration under contracts NASw-979 and NAS1-5794, and by the US Army Electronics Command under contract DA36-039-AMC-037 19 (E).

The work on laminated ferrite was originated by J. A. Rajchman and R. Shahbender, whose constant encouragement and leadership are greatly appreciated. Valuable contributions by many colleagues and technical personnel are too numerous to be individually acknowledged, but were essential to the successful completion of this program.

HIGH-POWER FREQUENCY DOUBLERS USING COUPLED TEM LINES*

BY
C. SUN

RCA Electronic Components
Princeton, New Jersey

Summary—This paper describes a class of high-power doublers using two varactors and coupled TEM lines. A 1.04 to 2.08 GHz circuit was designed to provide power output of 20 watts with 58% efficiency and 30 watts with 50% efficiency. The measured input and output impedances of the diode are in reasonable agreement with theory.

INTRODUCTION

NOW that high-power transistors are available in the 500-MHz range, high-power multipliers have become increasingly important in the development of solid-state power sources. This paper describes a class of high-power doublers using two varactors in a circuit employing coupled TEM lines. These doublers have the following advantages.

- (1) Two diodes with good heat sinks provide high-power-handling capability.
- (2) The TEM lines provide good impedance transformation for matching the diodes to the source and load.
- (3) The circuit is compact and is suitable for integrated-circuit applications.
- (4) The circuit provides good efficiency at microwave frequencies.

The first part of this paper describes the conditions for equal distribution of the input power between the diodes. It is shown that, with a proper configuration, the input-signal currents to the two diodes are of equal amplitude and 180 degrees out of phase; thus the output currents are in phase. Design considerations of the impedance matching for both the input and output circuits are then discussed. For the input circuit, where two coupled TEM lines are used, a two-port equivalent circuit is derived to determine the effects of the relevant parameters.

* The work reported in this paper was sponsored by the Air Force Avionics Laboratory, Research and Technology Division, Air Force Systems Command, Wright-Patterson Air Force Base, Ohio, under Contract Number AF 33 (615)-3036.

The theory of punch-through varactors is also reviewed. Finally, the experimental work is presented, and theory and experimental results are correlated.

ANALYSIS OF THE COUPLED TEM LINES

Input Circuit

Figure 1 shows the configuration of the four-port input circuit of a varactor doubler and indicates the direction of current flow for each

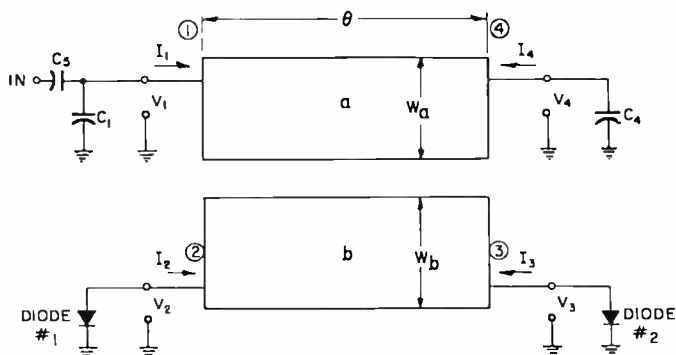


Fig. 1—Configuration of an input circuit of a varactor doubler using coupled TEM lines.

port. The input circuit consists of two coupled TEM lines (a) and (b) in a triplate structure, matched varactor diodes 1 and 2 mounted at ports 2 and 3, respectively, and a capacitor C_4 at port 4. The currents I_2 and I_3 to diodes 1 and 2 may be analyzed by use of an impedance matrix¹ if two assumptions are made: (1) that the output circuit does not couple to the input circuit, and (2) that two matched diodes provide the same input impedance Z_{in}' . The impedance matrix is

$$V_1 = Z_{11}I_1 + Z_{12}I_2 + Z_{13}I_3 + Z_{14}I_4 \quad (1)$$

$$V_2 = Z_{21}I_1 + Z_{22}I_2 + Z_{23}I_3 + Z_{24}I_4 \quad (2)$$

$$V_3 = Z_{31}I_1 + Z_{32}I_2 + Z_{33}I_3 + Z_{34}I_4 \quad (3)$$

$$V_4 = Z_{41}I_1 + Z_{42}I_2 + Z_{43}I_3 + Z_{44}I_4 \quad (4)$$

¹ H. Ozaki and J. Ishii, "Synthesis of a Class of Stripline Filters," *IRE Trans. on Circuit Theory*, Vol. CT-5, p. 104, June 1958.

where

$$\left. \begin{aligned} Z_{11} = Z_{44} &= \frac{(Z_{oc}^a + Z_{oo}^a) 1}{2 s} \\ Z_{12} = Z_{33} &= \frac{(Z_{oc}^a - Z_{oo}^a) 1}{2 s} \\ Z_{13} = Z_{32} &= \frac{(Z_{oc}^a - Z_{oo}^a) \sqrt{1 - s^2}}{2 s} \\ Z_{14} = Z_{41} &= \frac{(Z_{oc}^a + Z_{oo}^a) \sqrt{1 - s^2}}{2 s} \end{aligned} \right\} \quad (5)$$

$$\left. \begin{aligned} Z_{21} = Z_{34} &= \frac{(Z_{oc}^b - Z_{oo}^b) 1}{2 s} \\ Z_{22} = Z_{33} &= \frac{(Z_{oc}^b + Z_{oo}^b) 1}{2 s} \\ Z_{23} = Z_{32} &= \frac{(Z_{oc}^b + Z_{oo}^b) \sqrt{1 - s^2}}{2 s} \\ Z_{24} = Z_{31} &= \frac{(Z_{oc}^b - Z_{oo}^b) \sqrt{1 - s^2}}{2 s} \end{aligned} \right\} \quad (6)$$

Z_{oc}^a is the even-mode impedance of line a, Z_{oo}^a is the odd-mode impedance of line a, Z_{oc}^b and Z_{oo}^b are the impedances of line b, the term s is equal to $j \tan \theta$, and θ is the electrical length of the lines. Because the circuit is reciprocal, the following relationship exists between the impedances of lines a and b:

$$Z_{oc}^a - Z_{oo}^a = Z_{oc}^b - Z_{oo}^b. \quad (7)$$

The constraints for ports 2, 3, and 4 are given by

$$V_2 = -I_2 Z_{1n}' \quad (8)$$

$$V_3 = -I_3 Z_{1n}' \quad (9)$$

$$V_4 = -I_4 \frac{1}{j\omega C_4} \quad (10)$$

where Z_{in}' is the input impedance of the matched diodes.

For a solution of I_2/I_1 and I_3/I_1 in terms of I_4/I_1 , the simultaneous Equations (2), (3), (8), and (9) are used as follows:

$$\frac{I_2}{I_1} = - \frac{Z_{in}' \left(Z_{21} + Z_{24} \frac{I_4}{I_1} \right) + \frac{(Z_{oc}^b)^2 - (Z_{oo}^b)^2}{4}}{\Delta} \quad (11)$$

$$\frac{I_3}{I_1} = - \frac{Z_{in}' \left(Z_{31} + Z_{34} \frac{I_4}{I_1} \right) + \frac{[(Z_{oc}^b)^2 - (Z_{oo}^b)^2] \frac{I_4}{I_1}}{4}}{\Delta} \quad (12)$$

The following relations are used to derive Equations (11) and (12):

$$Z_{24}Z_{33} - Z_{23}Z_{34} = Z_{22}Z_{31} - Z_{32}Z_{21} = 0 \quad (13)$$

$$Z_{21}Z_{33} - Z_{23}Z_{31} = Z_{22}Z_{34} - Z_{32}Z_{24} = \frac{(Z_{oc}^b)^2 - (Z_{oo}^b)^2}{4} \quad (14)$$

$$\Delta = (Z_{22} + Z_{in}') (Z_{33} + Z_{in}') - Z_{23}Z_{32} \quad (15)$$

Substitution of Equations (11), (12), and (10) into Equation (4), yields

$$\frac{I_4}{I_1} = - \frac{Z_{41}\Delta - Z_{42} \left(Z_{21}Z_{in}' + \frac{(Z_{oc}^b)^2 - (Z_{oo}^b)^2}{4} \right) - Z_{43}Z_{in}'Z_{31}}{\left(\frac{1}{j\omega C_4} + Z_{44} \right) \Delta - Z_{43} \left(Z_{34}Z_{in}' + \frac{(Z_{oc}^b)^2 - (Z_{oo}^b)^2}{4} \right) - Z_{42}Z_{in}'Z_{24}} \quad (16)$$

If all the impedances are known in Equation (16), I_4/I_1 can be found; I_2/I_1 and I_3/I_1 in Equations (11) and (12) can then be computed. In

varactor multiplier applications, two matched varactors should share the input power equally, i.e., $I_2/I_1 = \pm I_3/I_1$. An examination of Equations (11) and (12) shows three possible solutions:

$$(i) \quad \frac{I_4}{I_1} = -1, \quad \frac{I_2}{I_3} = -1$$

$$(ii) \quad \frac{I_4}{I_1} = +1, \quad \frac{I_2}{I_3} = +1$$

(iii) The length of the line θ is selected so that $I_2/I_1 = I_3/I_1$ and is relatively independent of value of I_4/I_1 .

A detailed calculation of I_2/I_1 , I_3/I_1 , and I_4/I_1 as a function of C_4 for three different line lengths is given in Tables I, II and III. In computations of tables, the following values of impedances were assumed: $Z_{oc}^a = 98.1$, $Z_{oo}^a = 34.8$, $Z_{ec}^b = 86.5$, $Z_{eo}^b = 23.2$, and diode impedance $Z_{in}' = 5.87 - j13.85$. If an arbitrary input power of 50 watts is assumed, P_2 and P_3 are the powers absorbed by diodes No. 1 and No. 2. Also included in the tables is the calculation of the input impedance at port 1, $Z_1 = R_1 + jX_1 = V_1/I_1$ from Equation (1). P_2 and P_3 are computed by the following procedure:

$$I_1^2 = \frac{50}{R_1}$$

$$P_2 = I_2^2 \times 5.87 = \left(\frac{I_2}{I_1} \right)^2 \times I_1^2 \times 5.87$$

$$P_3 = \left(\frac{I_3}{I_1} \right)^2 \times I_1^2 \times 5.87$$

The value of θ is 0.277 radian in Table I and 0.833 radian in Table II; in both, C_4 is varied from 1 to 20 picofarads. As C_4 ranges from 8 to 20 picofarads, I_4/I_1 approaches $1 \angle 180^\circ$; therefore I_2/I_1 and I_3/I_1 have approximately equal amplitude and are about 180 degrees out of phase, corresponding to mode (i) operation. At the same time, P_2 and P_3 are approximately equal and the input impedance has an inductive value that may be matched to a 50-ohm generator impedance by a matching network, C_1 and C_5 , as shown in Figure 1.

Table I—Input Frequency = 1.04 GHz, $P_{in} = 50$ watts, $\theta = 0.277$ radian

C_1 (pF)	$\frac{I_2}{I_1}$	$\frac{I_3}{I_1}$	$\frac{I_4}{I_1}$	P_2 (watts)	P_3 (watts)	Z_1 (ohms)
1	0.324) -58.69°	0.499) 145.95°	0.56) 179.73°	14.85	35.15	2.09 - $j68.3$
2	0.398) -51.20°	0.504) 142°	0.73) 179.6°	19.2	30.8	2.43 - $j36.9$
4	0.458) -47.11°	0.50) 139°	0.868) 179.56°	22.37	27.63	2.77 - $j12.67$
8	0.498) -44.99°	0.513) 137°	0.956) 179.52°	24.28	25.72	3.02 + $j3.16$
10	0.507) -44.56°	0.514) 136.8°	0.976) 179.51°	24.68	25.31	3.08 + $j6.72$
12	0.514) -44.27°	0.514) 136.52°	0.99) 179.50°	24.96	25.04	3.12 + $j9.18$
20	0.527) -43.70°	0.516) 135.92°	1.01) 179.48°	25.5	24.5	3.21 + $j14.3$

Table II—Input frequency = 1.04 GHz, $P_{in} = 50$ watts, $\theta = 0.833$ radian

C_1 (pF)	$\frac{I_2}{I_1}$	$\frac{I_3}{I_1}$	$\frac{I_4}{I_1}$	P_2 (watts)	P_3 (watts)	Z_1 (ohms)
1	0.93) -156.76°	0.62) 36.45°	0.318) 175.72°	34.53	15.47	7.39 - $j28.68$
2	1.00) -155.24°	0.77) 31.83°	0.51) 174.88°	31.40	18.60	9.42 - $j16.40$
4	1.08) -153.88°	0.94) 27.99°	0.73) 173.92°	28.45	21.54	12.21 - $j2.29$
8	1.16) -152.93°	0.94) 27.99°	0.94) 173.03°	26.28	23.72	15.19 + $j10.57$
10	1.18) -152.72°	1.14) 24.61°	0.99) 172.79°	25.76	24.24	16.06 + $j14.03$
12	1.20) -152.57°	1.18) 24.15°	1.03) 172.62°	25.40	24.50	16.73 + $j16.58$
20	1.23) -152.26°	1.25) 23.16°	1.13) 172.22°	24.64	25.36	18.29 + $j22.33$

Table III—Input frequency = 1.04 GHz, $P_{in} = 50$ watts, $\theta = 3.6$ radians

C_1 (pF)	$\frac{I_2}{I_1}$	$\frac{I_3}{I_1}$	$\frac{I_4}{I_1}$	P_2 (watts)	P_3 (watts)	Z_1 (ohms)
1	0.92) -92.87°	0.94) -74.51°	0.45) -3.28°	24.29	25.71	10.27 - $j44.27$
2	1.05) -89.26°	1.05) 78.87°	0.65) -3.87°	25.00	25.00	13.08 - $j21.90$
4	1.18) -86.77°	1.15) -82.30°	0.84) -4.41°	25.52	24.48	16.10 - $j11.48$
6	1.24) -85.80°	1.20) -83.70°	0.93) -4.46°	25.74	24.26	17.66 + $j8.67$
8	1.27) -85.30°	1.23) -84.54°	0.98) -4.81°	25.86	24.13	18.62 + $j14.39$
10	1.30) -84.99°	1.25) -85.05°	1.01) -4.91°	25.93	24.07	19.26 + $j18.14$
12	1.31) -84.77°	1.26) -85.40°	1.04) -4.98°	25.98	24.02	19.73 + $j20.79$
20	1.35) -84.34°	1.29) -86.13°	1.09) -5.13°	26.09	23.91	20.73 + $j26.47$

In Table III, the electrical length θ is 3.6 radians. As C_4 varies between 8 and 12 picofarads, I_4/I_1 has values around $1 \angle 0^\circ$; I_2/I_1 and I_3/I_1 have about the same magnitude and phase, a condition corresponding to mode (ii) operation. However, because the length of the line is 3.6 radians in this case, I_2/I_1 and I_3/I_1 are almost equal for all values of C_4 from 1 to 20 picofarads, or for all values of I_4/I_1 , a condi-

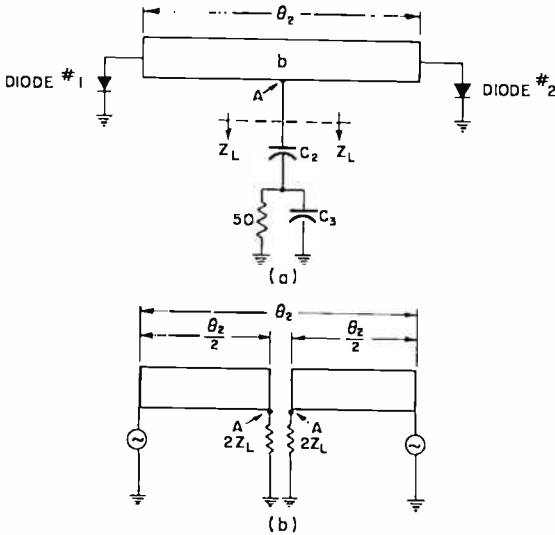


Fig. 2—The configuration and the equivalent circuit of the output circuit.

tion corresponding to mode (iii) operation. Therefore, in mode (i) and (ii) operation, C_4 provides a matching impedance and distributes power equally between the two diodes; in mode (iii) operation, C_4 matches impedance only.

Output Circuit

Because the two diodes with the matched characteristics are driven by fundamental currents of any of the modes (i), (ii), or (iii), the magnitudes and phases of the second-harmonic current to the two diodes must be equal. Thus the use of a suitable matching network will provide a power output that is symmetrical with respect to the two diodes. One possible configuration of the output circuit for the doubler is shown in Figure 2(a). Line b is used in both the input and output circuits. Z_L is an effective load impedance consisting of a capacitance-matching network (C_2, C_3) and a 50-ohm load referred to the center of the line b , as indicated by point A . Separate equivalent output circuits are

shown in Figure 2(b) for the two diodes, each having its own load impedance $2Z_L$. Impedance $2Z_L$ is so selected that after transformation by the transmission line length $\theta_2/2$, the impedance for each diode is the complex conjugate of its optimum output impedance.

DESIGN CONSIDERATIONS

Equivalent Circuit of the Diode

The equivalent circuit of the diode is shown in Figure 3. L_p is the lead inductance and C_p is the case capacitance. For the input circuit, the optimum input impedance of the diode Z_{in} is used and Z_{out} is used as the optimum output impedance of the diode. Z_{in}' and Z_{out}' are the total input and output impedances.

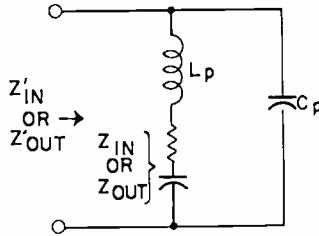


Fig. 3—The equivalent circuit of a diode.

Output Circuit

Because line b is used in both the input circuit and the output circuit, its length and impedance should be selected to meet the requirements of the two circuits. In the output circuit, the effective load impedance Z_L is a series-parallel capacitance network with the matched load of 50 ohms, as shown in Figure 2(a). In Figure 4, the locus of $2Z_L$ is shown in the shaded area bounded by the two semicircles AB and BC. The position of point B depends on the characteristic impedance Z_o of line b; in Figure 4, Z_o is 35 ohms. When the complex conjugate of the diode output impedance (Z_{out}')* is known, the length of the line having a proper characteristic impedance should be chosen to match $2Z_L$ with (Z_{out}')*. The characteristic impedance Z_o of the line b can be obtained from Getsinger.²

² W. J. Gestinger, "Coupled Rectangular Bars between Parallel Plates," *IRE Trans. on Microwave Theory and Techniques*, Vol. MTT-10, p. 65, Jan. 1962.

Input Circuit

The analysis of the coupled TEM lines in the earlier part of this paper is useful for determining the currents and power distribution between the diodes. However, these computations are both involved

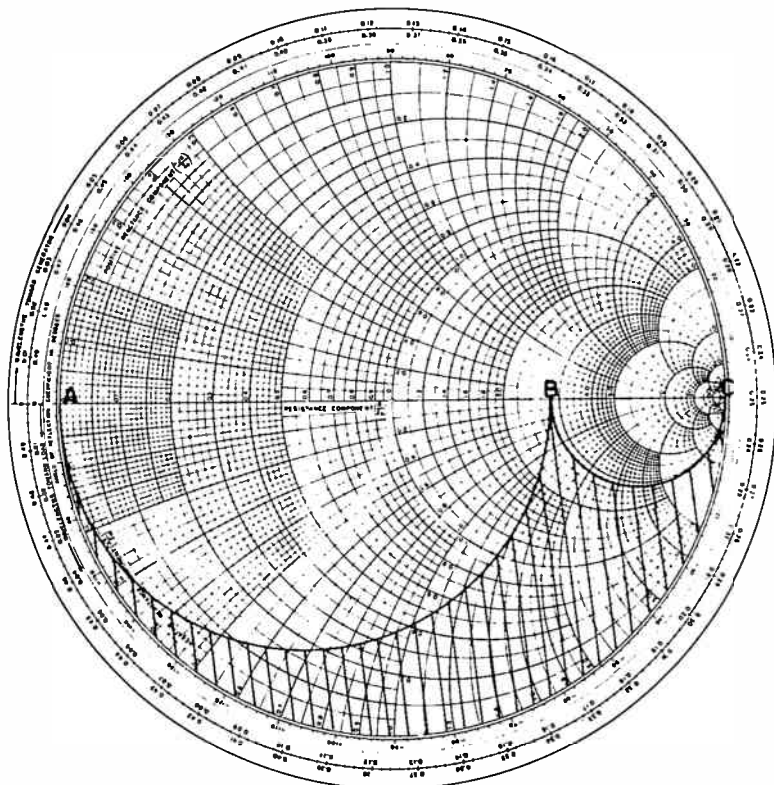


Fig. 4—The matching of output circuit.

and tedious. For establishing the importance of some of the parameters, a two-port equivalent circuit may be derived by the following steps: (a) I_3 and I_4 are solved in terms of I_1 and I_2 from Equations (9), (10), (3), and (4), and (b) I_3 and I_4 are substituted into Equations (1) and (2). The resulting equations are

$$V_1 = A_{11}I_1 + A_{12}I_2 \quad (17)$$

$$V_2 = A_{21}I_1 + A_{22}I_2 \quad (18)$$

where

$$A_{11} = Z_{11} + \frac{jx_4 Z_{13} Z_{31} - Z_{in}' Z_{14} Z_{41} - Z_{14} \Delta_1 \sqrt{1 - s^2}}{\Delta_2} \quad (19)$$

$$A_{12} = Z_{12} + \frac{jx_4 Z_{13} Z_{32} - Z_{in}' Z_{14} Z_{42} - Z_{13} \Delta_1 \sqrt{1 - s^2}}{\Delta_2} \quad (20)$$

$$A_{21} = Z_{21} + \frac{jx_4 Z_{31} Z_{23} - Z_{in}' Z_{41} Z_{24} - Z_{24} \Delta_1 \sqrt{1 - s^2}}{\Delta_2} \quad (21)$$

$$A_{22} = Z_{22} + \frac{jx_4 Z_{23} Z_{32} - Z_{in}' Z_{24} Z_{42} - Z_{23} \Delta_1 \sqrt{1 - s^2}}{\Delta_2} \quad (22)$$

$$x_4 = \frac{1}{\omega C_4} \quad (23)$$

$$\Delta_2 = (Z_{33} + Z_{in}') (Z_{44} - jx_4) Z_{34} Z_{43} \quad (24)$$

$$\Delta_1 = Z_{33} Z_{44} - Z_{34} Z_{43} \quad (25)$$

As given in Equations (20) and (21), $A_{12} = A_{21}$. The input impedance Z_1 at port 1 is given by

$$Z_1 = A_{11} - \frac{A_{12}^2}{A_{22} + Z_{in}'} \quad (26)$$

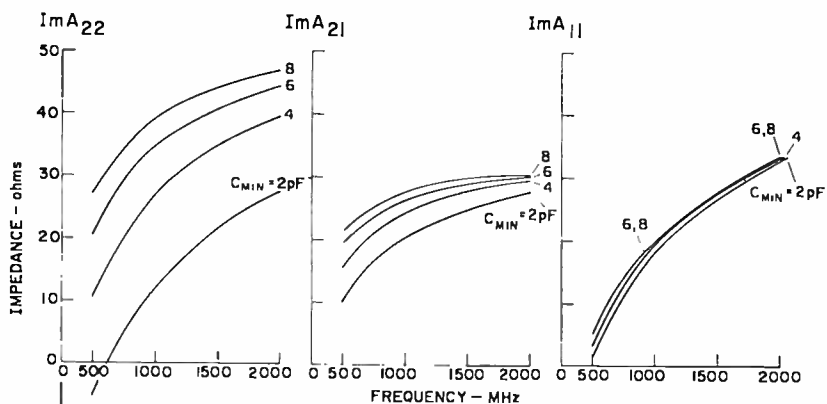
where A_{11} , A_{12} , and A_{22} are all complex and contain the input impedance Z_{in}' of diode 2; and Z_{in}' in the denominator of Equation (26) is the load impedance or input impedance of diode 1.

Before A_{11} , A_{12} , and A_{22} shown in Equations (19) to (22) are plotted as a function of frequency, the values of some parameters are chosen to reduce the number of figures.

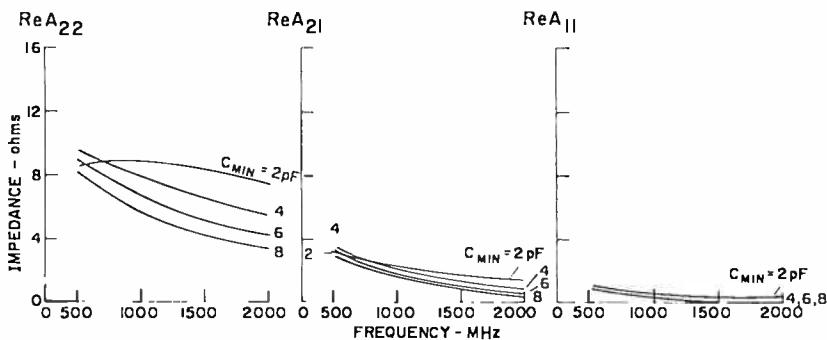
The length θ used for lines a and b are 0.7979 radian for all the figures. Even and odd impedances of lines a and b are made equal without loss of generality: $Z_{oe}^a = Z_{oe}^b = 86.5$ ohms, and $Z_{oo}^a = Z_{oo}^b = 23.2$ ohms. The values of the length and impedance of line b are suitable for both the input and output circuits. The diodes are assumed to have a capacitance variation $\gamma = 0$ for a drive level of 2.0 (γ and drive level are defined later) with an optimum input imped-

ance^{3,4} given by
$$Z_{in} = \frac{2}{3\pi} \frac{1}{\omega_0 C_{min}} - j \frac{1}{2\omega_0 C_{min}} \quad (27)$$

where C_{min} is the minimum capacitance of the diode and ω_0 is the input angular frequency. The lead inductance and case capacitance are ne-



(a) Imaginary



(b) Real

Fig. 5—(a) Imaginary and (b) real parts of A_{11} , A_{21} , and A_{22} as a function of frequency, with C_{min} as a parameter and $C_4 = 5$ pF ($Z_{oe}^a = Z_{oe}^b = 86.5$ ohms, $Z_{oo}^a = Z_{oo}^b = 23.2$ ohms, and $\theta = 0.7979$ radian).

glected in the computations because these parameters vary from diode to diode; therefore, $Z_{in}' = Z_{in}$.

At $C_4 = 5$ pF, Figure 5(a) shows the reactive part of the impedances

³ C. B. Burckhardt, "Analysis of Varactor Frequency Multipliers for Arbitrary Capacitance and Drive Level," *Bell System Tech. Jour.*, Vol. 44, p. 675, April 1965.

⁴ R. P. Rafuse, "Recent Developments in Parametric Multipliers," *Proc. National Electronics Conf.*, p. 461, Oct. 1963.

of A_{11} , A_{21} , and A_{22} as a function of frequency with C_{min} as a parameter; Figure 5(b) illustrates the real part of the impedances A_{11} , A_{21} , and A_{22} . These figures indicate that the use of a different C_{min} causes very little change of A_{11} , a slight variation of A_{12} , and an appreciable change of A_{22} . However, the imaginary part of A_{22} increases with the increase of C_{min} , and the real part of A_{22} decreases except for the

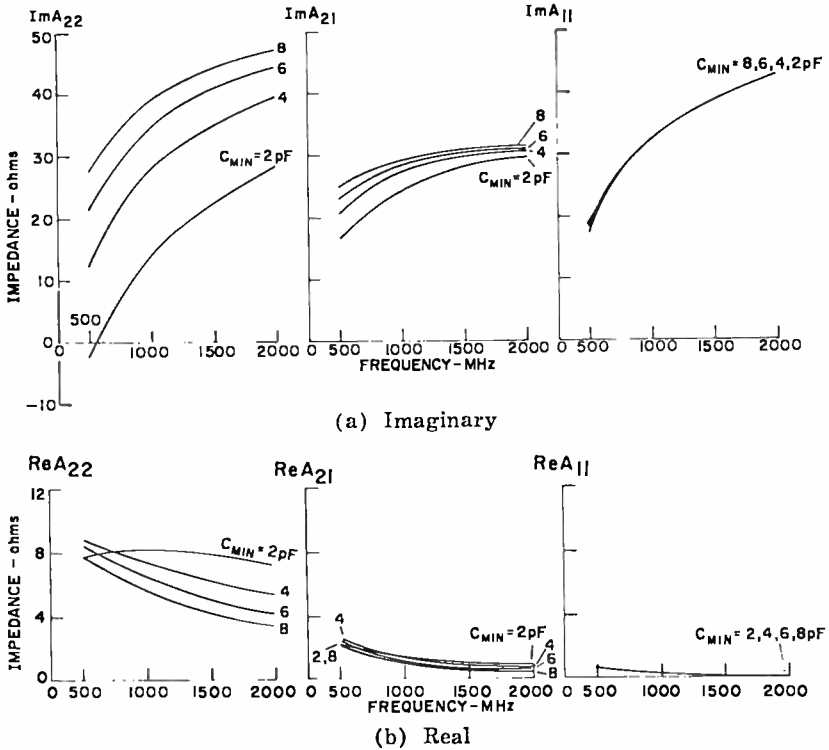


Fig. 6—(a) Imaginary and (b) real parts of A_{11} , A_{21} , and A_{22} as a function of frequency with C_{min} as a parameter and $C_4 = 10$ pF ($Z_{oe}^a = Z_{oe}^b = 86.5$ ohms, $Z_{oo}^a = Z_{oo}^b = 23.2$ ohms, and $\theta = 0.7979$ radian).

case where $C_{min} = 2$ pF. As the value of C_4 is changed from 5 to 10 pF, the real and imaginary parts of impedances A_{11} , A_{21} , A_{22} change as shown in Figures 6(a) and 6(b), respectively. A comparison of Figures 5 and 6 shows that the main differences is in A_{11} , with only a small change in A_{21} , and very little change in A_{22} . Therefore, the value of A_{11} is most sensitive to the changes of C_4 .

The effects of impedance levels Z_{oe}^a , Z_{oo}^a , Z_{oe}^b , and Z_{oo}^b on impedances A_{11} , A_{21} , and A_{22} are shown in Figures 7(a) and 7(b). In three case studies, Z_{oe}^a was made equal to Z_{oe}^b and Z_{oo}^a equal to Z_{oo}^b . Z_{oo}^a

C $Z_{0e}^a = Z_{0e}^b = 86.5 \Omega$, $Z_{0o}^a = Z_{0o}^b = 23.2 \Omega$

B $Z_{0e}^a = Z_{0e}^b = 66.5 \Omega$, $Z_{0o}^a = Z_{0o}^b = 23.2 \Omega$ $C_{MIN} = 4 \text{ pF}$

A $Z_{0e}^a = Z_{0e}^b = 46.5 \Omega$, $Z_{0o}^a = Z_{0o}^b = 23.2 \Omega$ $\theta = 0.7979 \text{ RADIAN}$

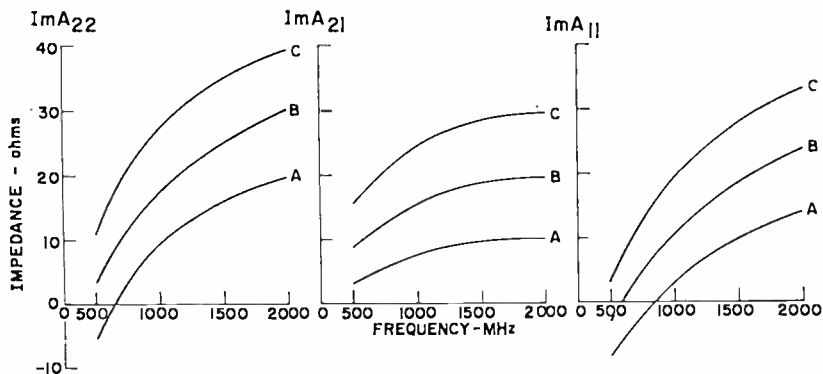


Fig. 7a—Imaginary part of A_{11} , A_{21} , and A_{22} as a function of frequency, with Z_{0e} as a parameter.

and Z_{0o}^b were 23.2 ohms in all three cases. A_{11} , A_{21} , and A_{22} all showed increases with increasing Z_{0e} s. A_{11} and A_{22} increase because they are related to the sum of Z_{0e} and Z_{0o} , as given by Equations (19) and (22); A_{21} increases because of the increase of the values of $(Z_{0e} - Z_{0o})$, as

C $Z_{0e}^a = Z_{0e}^b = 86.5 \Omega$, $Z_{0o}^a = Z_{0o}^b = 23.2 \Omega$

B $Z_{0e}^a = Z_{0e}^b = 66.5 \Omega$, $Z_{0o}^a = Z_{0o}^b = 23.2 \Omega$ $C_{MIN} = 4 \text{ pF}$

A $Z_{0e}^a = Z_{0e}^b = 46.5 \Omega$, $Z_{0o}^a = Z_{0o}^b = 23.2 \Omega$ $\theta = 0.7979 \text{ RADIAN}$

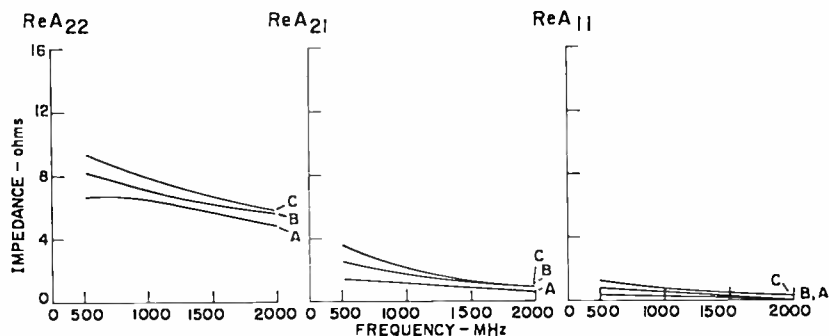


Fig. 7b—Real part of A_{11} , A_{21} , and A_{22} as a function of frequency, with Z_{0e} as a parameter.

suggested by Equation (20) or (21). These values of Z_{oc} 's and Z_{os} 's can also be obtained from Getsinger.²

Review of the Theory on Punch-Through Varactors

Rafuse⁴ analyzed the punch-through varactor-type doubler for the case where the average charge on the junction is zero and the minimum and maximum charge just reach the breakdown charge. This analysis corresponds to Burckhardt's analysis³ of drive level equal to 2.0 and capacitance-voltage variation $\gamma = 0$. Assuming a constant series resistance R_s , he found that this type of varactor having $\gamma = 0$ with a drive level of 2.0 provides the highest efficiency. Drive level and γ are defined as follows:

$$\text{Drive level} = \frac{Q_{\max} - Q_{\min}}{Q_B - q_\phi}, \quad (28)$$

$$C_j = C_{\min} \left[\frac{V_B - \phi}{V_j - \phi} \right]^\gamma, \quad (29)$$

where C_j is the junction capacitance, C_{\min} is the minimum junction capacitance, V_B is the breakdown voltage, ϕ is the contact potential, V_j is the voltage across the capacitance, Q_{\max} is the maximum charge, Q_{\min} is the minimum charge, Q_B is the breakdown charge, and q_ϕ is the charge at contact potential.

The optimum input and output resistance of the varactor are given by

$$R_{\text{in}} = R_{\text{out}} = \frac{2}{3\pi} \frac{1}{\omega_o C_{\min}}. \quad (30)$$

The average capacitance of the varactor diode for the input and output circuits are related as follows:

$$C_{\text{in}} = C_{\text{out}} = 2C_{\min}. \quad (31)$$

The bias voltage required for this mode of operation ($\gamma = 0$ and drive level = 2.0) is given by

$$V_{\text{bias}} \cong \frac{V_B}{4}. \quad (32)$$

The input and output power-handling capacity at the junction of each diode is given by

$$P_{\text{in}} = P_{\text{out}} = 0.0628 V_n^2 C_{\text{min}} \omega_n \quad (33)$$

If two diodes are used and the circuit loss and diode loss are also considered for the present case, the total input power P_1 , and total output power P_2 of the circuit are as follows:

$$P_1 = 2P_{\text{in}} + 2P_{d1} + P_{c1}, \quad (34)$$

$$P_2 = 2P_{\text{out}} - 2P_{d2} - P_{c2}. \quad (35)$$

P_{d1} and P_{d2} are the dissipation losses of the two diodes at the input and output frequency, respectively, and are given by

$$P_{d1} = P_{d2} = \frac{16}{27} Q_n^2 \omega_n^2 R_x; \quad (36)$$

P_{c1} and P_{c2} are the input and output circuit losses. If a circuit can be designed so that $P_{c1} \approx P_{c2}$, then Equations (34) and (35) can be added to determine the required input power for a drive level of 2.0, as follows:

$$P_1 + P_2 = 4P_{\text{in}} \quad (37)$$

or

$$P_1 = \frac{4P_{\text{in}}}{(1 + \eta)}, \quad (38)$$

where η is the measured over-all circuit efficiency.

EXPERIMENTAL WORK

Diode Selection

On the basis of the design considerations, a 1.04 to 2.08 GHz doubler circuit was constructed with an objective of delivering power output of more than 20 watts. Two diodes having low thermal resistance were selected so that the circuit would not be thermally limited at 20 watts of output power. The two diodes also have almost identical capacitance characteristics, as shown in Figure 8. The capacitance-voltage variation γ of the two diodes is nearly zero from approximately zero voltage to breakdown voltage. The diodes have a breakdown voltage of 80 volts

and a minimum capacitance of 5.5 pF. For a drive level of 2.0, each diode can handle input or output power of 14.5 watts at an input frequency of 1.04 GHz, as determined by Equation (33).

Lead inductance of the diode is approximately 1 nH, measured at 1.04 GHz. The case capacitance is 0.5 pF, measured on a capacitance bridge. (At 1.04 and 2.08 GHz, the effect of case capacitance may be neglected.) The total input impedance of the diode shown in Figure 3 is given by

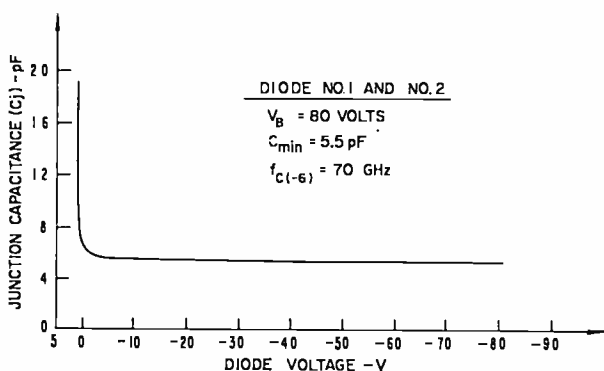


Fig. 8—Junction capacitance versus voltage of diode No. 1 and No. 2.

$$Z_{in}' = \frac{2}{3\pi} \frac{1}{\omega_0 C_{min}} - j \frac{1}{2\omega_0 C_{min}} + Z_{lead\ inductance} = 5.87 - j7.29\ \text{ohms}, \quad (39)$$

$$(Z_{out}')^* = \left(\frac{2}{3\pi} \frac{1}{\omega_0 C_{min}} - j \frac{1}{4\omega_0 C_{min}} + Z_{lead\ inductance} \right)^* \\ = 5.87 - j6.15\ \text{ohms}. \quad (40)$$

Circuit Configuration

The geometry of the triplate circuit shown in Figure 9 is determined by the analysis described previously. Lines a and b are selected to be 1.5 inches long, a value corresponding to an electrical length θ of 0.833 radian at the input frequency. For the output circuit, the characteristic impedance of line b is 35 ohms. This value is based on the consideration that line a may now be regarded as a ground plane because the second harmonic does not propagate on line a. A tunable

capacitor network C_2 and C_3 connected to the center of line b can be adjusted to make the impedance equal to the $(Z_{out}')^*$ value given by Equation (40). For the input circuit, several sets of Z_{oc} and Z_{oo} are used in Equation (16) to study the current balance between the diodes and the input impedance Z_1 at port 1; that is, whether Z_1 can be matched to the 50-ohm generator impedance. In this circuit, the

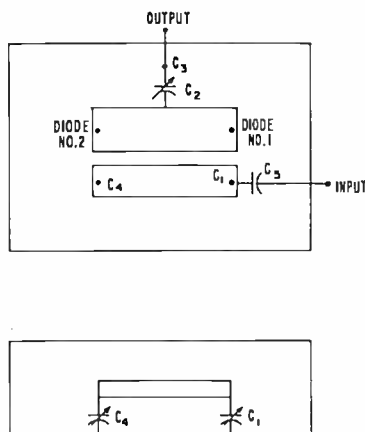


Fig. 9—Circuit configuration of a 1.04 GHz to 2.08 GHz doubler circuit.

coupled-lines geometry was chosen to provide equal odd- and even-mode impedances, as follows:

$$Z_{oc}^a = Z_{oc}^b = 86.5 \text{ ohms} .$$

$$Z_{oo}^a = Z_{oo}^b = 23.2 \text{ ohms}$$

In the course of the experiments, however, a small modification of line a resulted in the following slight impedance unbalances:

$$Z_{oc}^a = 98.1 \text{ ohms}, \quad Z_{oc}^b = 86.5 \text{ ohms}$$

$$Z_{oo}^a = 34.8 \text{ ohms}, \quad Z_{oo}^b = 23.2 \text{ ohms}$$

For realization of the above impedances, only the width of line a and the spacing between line a and the ground plane can be adjusted, because the dimension of line a and the spacing between the two lines are fixed by the characteristic impedance of the output line. The capaci-

tor C_4 at the end of line a is tunable, so that the division of input power between the two diodes and the input impedance Z_1 of port 1 can be controlled without change of the configuration of the lines. The input impedance Z_1 is matched to a 50-ohm generator by use of a tunable capacitor C_1 and a fixed capacitor C_5 .

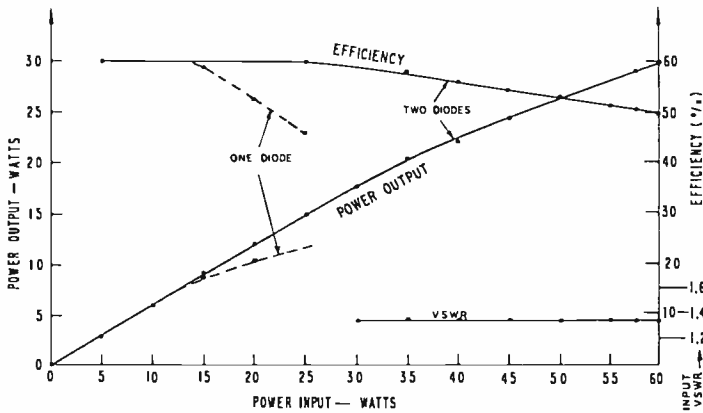


Fig. 10—Power output, efficiency and input VSWR versus power input of L to S band doubler.

Experimental Results

The power output and efficiency performance curves of the two-diode doubler are shown in Figure 10. For comparison, Figure 10 also shows the performance of a single diode operated in a similar circuit.⁵ The two-diode circuit handles an input power of 60 watts with 50% efficiency. The measured input VSWR is 1.35 at all power levels up to 60 watts, and the measured total input and output circuit loss is about 0.5 dB.

In the design of the multiplier, it was assumed that the two matched diodes have the same optimum impedances, i.e., that they share the input and output power equally. The r-f voltage probed on line b for an input power level of 37.5 watts (drive level = 2.0) shows that this assumption is justified. The magnitudes of the r-f voltage at the two diodes are equal within a measurement accuracy of 0.3 dB, as shown in Figure 11. The same figure shows that the r-f voltage at the

⁵ J. R. Collard, C. Sun, and T. E. Walsh, "High-Power Microwave Varactors and Varactor Multipliers," *Wescan/66 Technical papers*, Aug. 1966.

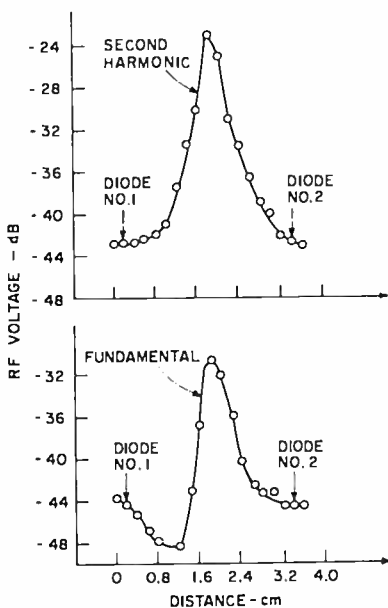


Fig. 11—Distribution of r-f voltages on line b.

second harmonic frequency also has the same amplitude at the plane of the two diodes. In the analysis of the input circuit, it was also assumed that the output circuit does not couple to the input circuit at the fundamental frequency. This decoupling of the two circuits is reflected in the low unwanted harmonic content at the output. All detected harmonic signals are summarized in Table IV.

Table IV

Unwanted Signals	dB Below Reference Output Signal (20.6 watts at 2.08 GHz)
Fundamental	32
3rd harmonic	48
4th harmonic	41
5th harmonic	60
6th harmonic	60
7th harmonic	52
8th harmonic	64
9th harmonic	90
10th harmonic	72

Comparison between Theory and Experiment

For a drive level of 2.0, and an over-all circuit efficiency of about 55%, Equation (38) predicts a required power input of 37.5 watts, where P_{in} for the varactor diode is 14.5 watts. It is interesting to note in Figure 10 that the circuit can handle an input power of more than 60 watts, corresponding to drive level > 2.0 , with only a slight decrease in efficiency.

At a drive level of 2.0, the measured d-c bias is 20 volts, the value predicted by Equation (32). The measured input VSWR is 1.35. For a comparison of the measured VSWR with the theoretically predicted value, the following steps are used. The circuit is first tuned for the maximum output at a drive power of 37.5 watts. All the values of capacitors are measured at the operating frequency of 1.04 GHz; $C_1 = 6.13$ pF, $C_5 = 5.75$ pF, and $C_4 = 9$ pF. The capacitors have a VSWR of 90 at this frequency.

The circuit parameters A_{11} , A_{12} , and A_{22} , calculated by use of Equations (19), (20), and (22), are as follows: $A_{11} = 0.18 + j45.50$, $A_{12} = 1.12 + j31.05$, $A_{22} = 7.00 + j36.94$. These values are based on $C_4 = 9$ pF, $Z_{oc}^a = 98.1$ ohms, $Z_{oc}^a = 34.8$ ohms, $Z_{oc}^b = 86.5$ ohms, $Z_{oc}^b = 23.2$ ohms, $\theta = 0.833$ radian and $Z_{in}' = 5.87 - j7.29$ ohms, as given by Equation (39). The input impedance at port 1 in Figure 1 is calculated by Equation (26): $Z_1 = 10.07 + j17.30$. For $C_1 = 6.13$ pF and $C_5 = 5.75$ pF, an input VSWR of 1.5 is obtained rather than the measured value of 1.35.

As a check of the output impedance of the circuit, the output matching capacitors C_2 and C_3 were replaced by a slide-screw tuner connected to the center of line b through a d-c blocking capacitor; it was thought that the series-connected capacitor C_2 might distort fields appreciably and cause inaccurate results. The slide-screw tuner was adjusted to provide the same efficiency provided by the capacitor C_2 and C_3 arrangement. The impedance of the slide-screw tuner was calculated, and the complex conjugate of the optimum output impedance of the diode was deduced to be $(Z_{out}')^* = 8.2 - j10.5$ ohms. The theoretically predicted value is $(Z_{out}')^* = 5.87 - j6.15$ ohms, as given by Equation (40).

The discrepancy between theory and experiment is probably caused by the following factors:

(1) The diodes do not have a capacitance-voltage variation γ precisely equal to zero.

(2) The theoretical calculations were made with the assumption that the output port is tuned to the average diode capacitance, follow-

ing Penfield and Rafuse⁶ for the case of abrupt-junction varactors. It is not clear that this assumption is valid for the overdriven punch-through varactors.

CONCLUSIONS

A double circuit using two varactors and coupled TEM lines has been analyzed. A 1.04 to 2.08 GHz circuit was designed to provide power output of 20 watts with 58% efficiency and 30 watts with 50% efficiency. By use of the same approach, high-power doublers at output frequencies beyond 2 GHz are feasible. The input and output impedances of the diode have been compared with the theory with reasonable agreement. The circuit configuration is compact and is suitable for integrated-circuit application if all the values of the tunable capacitors can be properly realized.

⁶ P. Penfield and R. P. Rafuse, *Varactor Applications*, pp. 329-412, M.I.T. Press, 1962.

MULTIPLE-LOOP FREQUENCY-COMPRESSIVE FEEDBACK FOR ANGLE-MODULATION DETECTION*

BY

H. HEINEMANN, A. NEWTON, AND J. FRANKLE

RCA Communications Systems Division
New York, N. Y.

Summary—A formal procedure is presented for the synthesis of compound frequency-compressive loops. This is an extension of the FM Feedback (FMFB) and phase-locking principles, leading to iterative FMFB and FMFB-PLD (Phase-Locked Discriminator) loops. Reduced threshold of angle-modulation detection is achieved by virtue of the low threshold of the detection device enclosed within the loop. A criterion for minimum threshold is applied, and optimum loop parameters are obtained, including the synthesis of base-band filters. Although principal consideration is given to FMFB-PLD and FMFB-FMFB double loops, the synthesis procedure can be extended to demodulators of an arbitrary number of feedback paths.

Experimental verification of predicted results was obtained. A threshold Carrier-to-Noise Ratio (CNR) of 2–3 dB was achieved in the Carson's rule predetection bandwidth for deviation ratios in the range of 2.5–7. This represents an extension of 3–4 dB relative to the FMFB or PLD.

INTRODUCTION

THIS PAPER deals with an extension of the frequency-feedback principle in FM detection. Figure 1 shows a frequency-compressive loop and its principal elements. Negative feedback is used to compress the deviation of the angle-modulated input signal. The return voltage-controlled oscillator (VCO) signal tracks the input frequency with a finite frequency error, resulting in a compressed deviation signal being transmitted through the i-f filter. This permits reduced bandwidth in the forward path and reduced noise power applied to the FM detector. In the conventional FMFB system, the FM detector is comprised of a limiter and discriminator.

It was demonstrated by Enloe¹ that two nearly independent thresholds are at play in the FMFB demodulator. The open-loop threshold is due to noise capture in the limiter and is determined by the "com-

* The work reported herein was supported in part by USAECOM Contract DA 28-043 AMC-00167 (E).

¹L. H. Enloe, "Decreasing Threshold FMFB," *Proc. IRE*, Jan. 1962 and *NEC Proc.*, 1962, p. 497.

pressed" bandwidth of the band-pass filter preceding the limiter-discriminator. The feedback threshold is due to the noise being presented to the VCO, and is determined by the closed-loop noise bandwidth. An increasing feedback factor results in greater i-f bandwidth compression and reduced open-loop threshold. On the other hand, the closed-loop noise bandwidth and, hence, the feedback threshold, increases with increasing feedback factor. An optimum is achieved when the two thresholds are coincident. Based on this rule, the overall

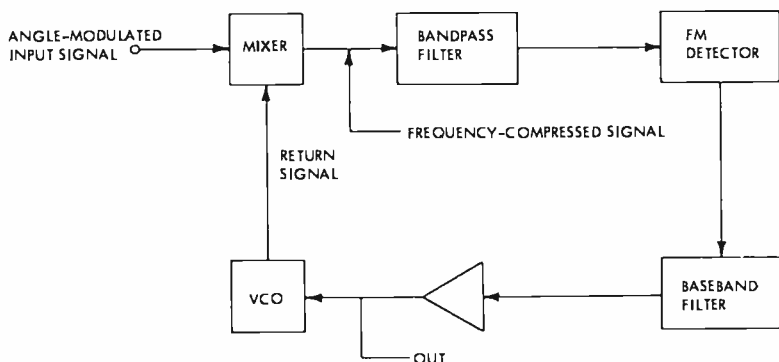


Fig. 1—Block diagram of frequency-compressing loop.

threshold performance is fundamentally limited by the threshold performance of the demodulating device within the loop. By replacing the limiter-discriminator within the loop with a lower-threshold device, and reducing the loop gain to make the feedback threshold coincide with the "new" open-loop threshold, an overall threshold reduction for the FMFB system will result. This article describes the theoretical and experimental results as well as filter synthesis for compound loops enclosing a phase-locked discriminator (PLD) and an FMFB demodulator, denoted FMFB-PLD and FMFB-FMFB, respectively.

REVIEW OF FMFB SYNTHESIS

The synthesis of compound loops presented in this paper derives from Enloe's procedures, with appropriate modifications for open-loop threshold. It will be useful, therefore, to review the FMFB synthesis according to this procedure.

The threshold carrier-to-noise ratio (CNR) of the limiter discriminator is in the range of 6 – 14 dB in the noise bandwidth of the pre-detection band-pass filter. In terms of the peak input modulation index,

M , and the feedback factor, F , the predetection noise bandwidth for a Carson's rule design and a single-pole filter is

$$B_n = \frac{\pi}{2} \left(1 + \frac{M}{F} \right) 2f_b, \quad (1)$$

where f_b is the top base-band frequency and $\pi/2$ is the ratio of the noise-to-nominal (3 db) bandwidths.

It is found in practice that the distortion-reducing properties of the feedback loop permit a tighter fit of the information channel in the predetection filter. This results in a lower open-loop threshold. The

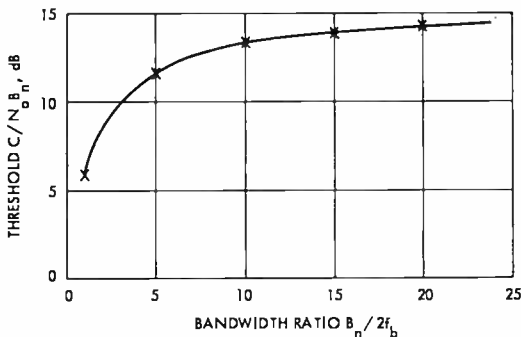


Fig. 2—Threshold $C/(N_o B_n)$ in the i-f noise bandwidth as a function of $B_n/(2f_b)$ (Based on Reference (1)).

design denoted by "Minimum CNR" implies a single-pole bandwidth of

$$B_n = \frac{\pi M}{2 F} 2f_b. \quad (2)$$

Given the CNR threshold in B_n of $[C/(N_o B_n)]_T$, where N_o is the noise power density, the threshold CNR's in $2f_b$ in dB are:

$$\left(\frac{C}{N_o 2f_b} \right)_T = \left(\frac{C}{N_o B_n} \right)_T + 10 \log \frac{\pi}{2} \left(1 + \frac{M}{F} \right), \quad (3)$$

and

$$\left(\frac{C}{N_o 2f_b} \right)_T = \left(\frac{C}{N_o B_n} \right)_T + 10 \log \frac{\pi}{2} \left(\frac{M}{F} \right), \quad (4)$$

for the Carson's Rule and the Minimum CNR designs, respectively.

$[C/(N_o B_n)]_T$ is the threshold CNR within the compressed i-f bandwidth. Figure 2 presents a graph of $[C/(N_o B_n)]_T$ versus $B_n/2f_b$. Figure 3 presents a family of open loop curves of F versus $[C/(N_o 2f_b)]_T$ for various values of M using the Carson's Rule design, while Figure 4 presents the corresponding plots for the Minimum CNR design.

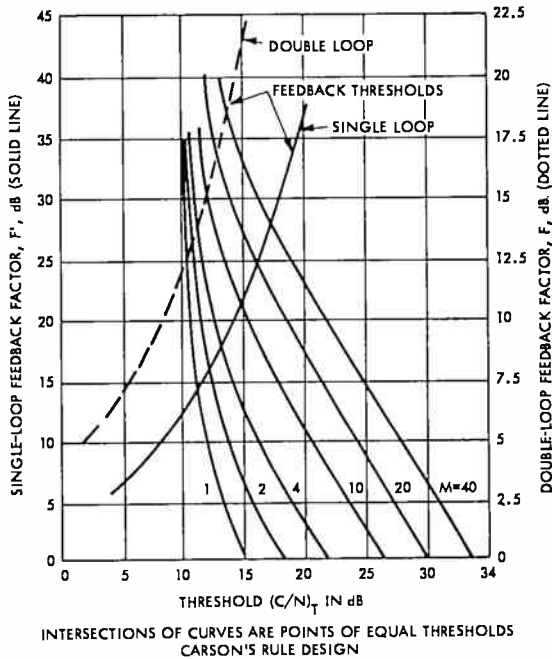


Fig. 3—Open-loop and feedback thresholds referred to $2f_b$ versus feedback factor for single and double loops using Carson's Rule design (based on Reference (1)).

The closed-loop bandwidth is an increasing function of F . Figure 5 shows the normalized two-sided closed-loop noise bandwidth, B_c , as a function of F . The parameter ϕ_b is excess phase shift at f_b . Compensation (added zeroes) is introduced to minimize B_c . A noise penalty is incurred when delay is present. For simplicity this paper considers only the case of zero delay.

It was found experimentally¹ that feedback threshold occurs when the CNR in the closed loop bandwidth, B_c , is

$$\left(\frac{C}{N_o B_c}\right)_T = 4.8 \left(\frac{F-1}{F}\right)^2 \tag{5}$$

It is now possible to relate $[C/(N_o 2f_b)]_T$ to F for the feedback threshold. This is represented by the feedback threshold curves in Figures 3 and 4 for zero delay. Note that for a given open-loop response (2-pole Butterworth), the feedback threshold depends solely on F .

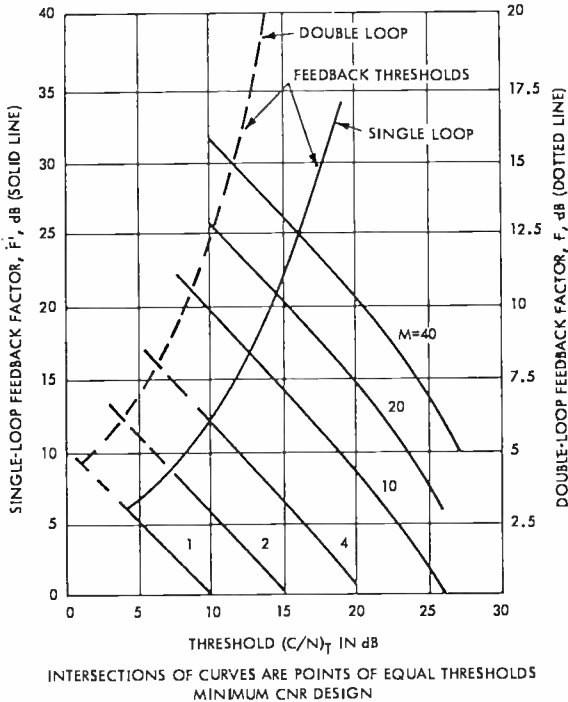


Fig. 4—Open-loop and feedback thresholds referred to $2f_b$, versus feedback factor for single and double loops using Minimum CNR design (based on Reference (1)).

The optimum threshold is obtained from the intersections of the open loop and feedback threshold curves.

There remains the synthesis of the base-band filter $H(S)$ to realize a prescribed open loop response $G_o(S)$. A maximally flat response is desired, to maintain the prescribed feedback gain over the base bandwidth. A two-pole Butterworth function is a common choice for the open-loop response, as it provides sufficiently flat response with adequate phase margin for stability. To realize this response in an FMFB system, the base-band filter must furnish the two poles of the Butterworth response and a zero to cancel the pole associated with the i - f

filter (assuming a single-pole filter). This yields an under-damped second-order closed-loop response.

The two-pole Butterworth open-loop response is given by

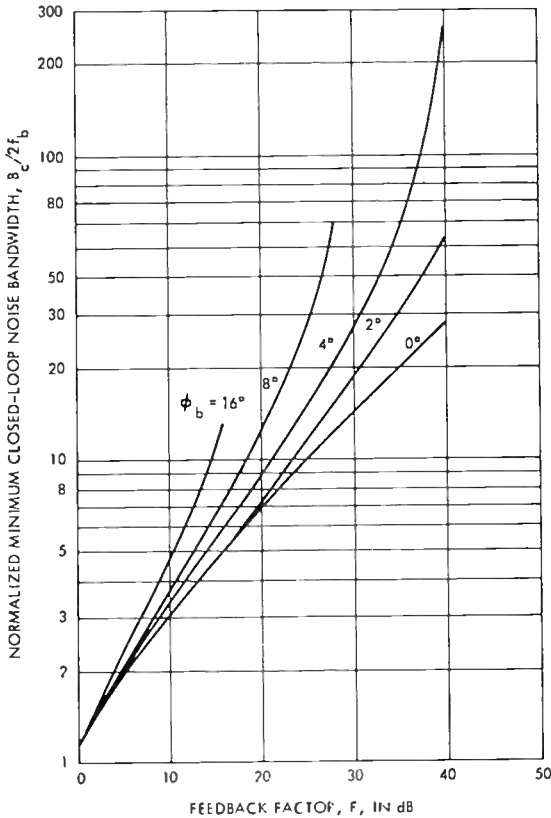


Fig. 5—Normalized minimum closed loop noise bandwidth versus feedback factor for different ϕ_b , the excess linear phase shift at top base-band frequency.

$$G_n(S) = \frac{A\omega_b}{a} \frac{S + a\omega_b}{S^2 + \sqrt{2}\omega_b S + \omega_b^2} \tag{6}$$

Where A is the open loop gain and is equal to $F - 1$. The factor a defines the added zero for minimum B_c .

The low-pass analog of the single-pole i-f filter is given by

$$A_L = b\omega_b / (S + b\omega_b) \tag{7}$$

To cancel the i - f pole and realize the desired $G_o(S)$, the prescribed response is of the form

$$H(S) = \frac{(S + b\omega_b)(S + a\omega_b)}{S^2 + \sqrt{2}\omega_b S + \omega_b^2} \left(\frac{1}{ab} \right) \tag{8}$$

The term b can be expressed as $k + (M/F)$, where k is 0 for the Minimum CNR design and 1 for the Carson's Rule design.

Realization of $H(S)$ for the base-band filter is discussed later.

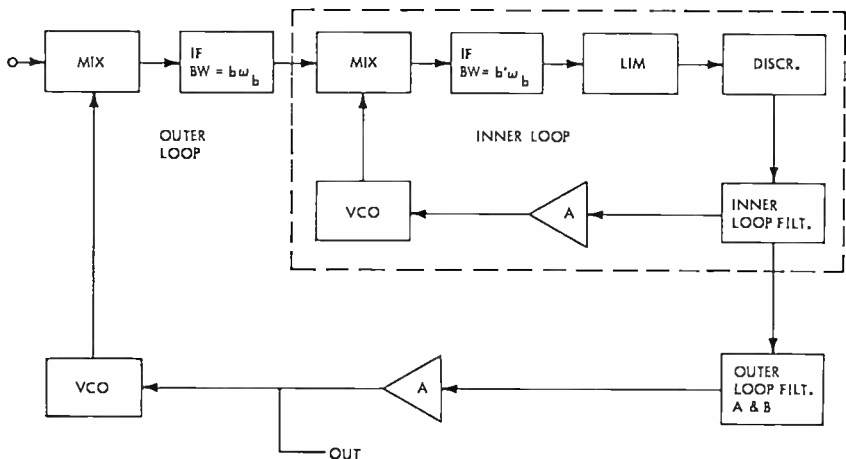


Fig. 6—Block diagram of iterative FMFB.

THE DOUBLY APPLIED FMFB LOOP

The block diagram of the FMFB-FMFB loop is shown in Figure 6. The loop will exhibit three independent thresholds, two feedback and one open-loop threshold. Again we wish to bring all thresholds into coincidence. Since the feedback threshold is a function of F only, for a given base band we require that both feedback factors be equal. This results in a frequency-compression factor F^2 , and the open-loop threshold is given by

$$\left(\frac{C}{N_o 2f_b} \right)_T = \left(\frac{C}{N_o B_n} \right)_T + 10 \log \frac{\pi}{2} \left(1 + \frac{M}{F^2} \right), \tag{9}$$

for the Carson's Rule design, and

$$\left(\frac{C}{N_o 2f_b}\right)_T = \left(\frac{C}{N_o B_n}\right)_T + 10 \log \frac{\pi}{2} \left(\frac{M}{F^2}\right) \quad (10)$$

for the Minimum CNR design. Returning to Figures 3 and 4, the right-hand ordinate is scaled by a factor of 2, in dB, and the feedback threshold curve is replotted (dotted line). The new intersections represent threshold for the FMFB-FMFB loop.

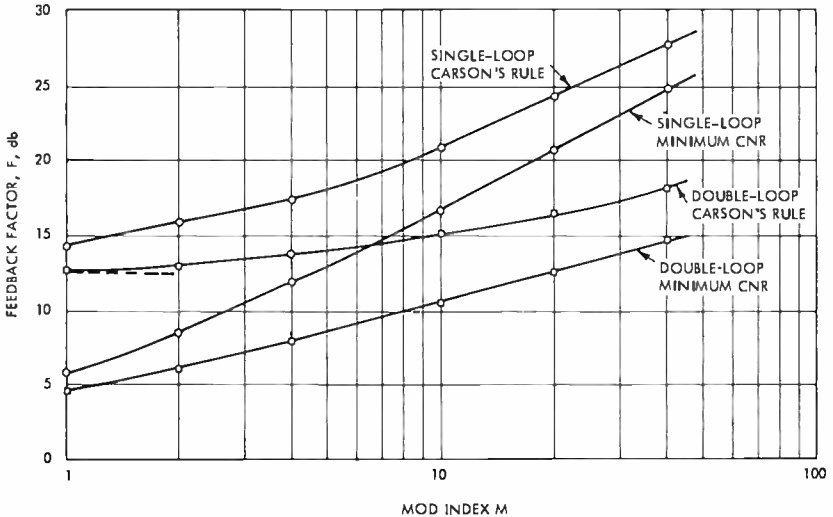


Fig. 7—Plots of feedback factor versus input modulation index.

Plots of F versus M are shown in Figure 7. Figure 8 shows $[C/(N_o 2f_b)]_T$ versus M for the FMFB-FMFB, and Figure 9 shows test tone signal-to-noise ratios versus $[C/(N_o 2f_b)]_T$ loci for the FMFB-FMFB systems.

THE FMFB-PLD COMPOUND LOOP

The treatment of the FMFB demodulator enclosing the PLD is analagous. The open-loop threshold CNR of the PLD in the compressed bandwidth is the principal parameter, and the feedback factor, F , of the FMFB is adjusted for equal feedback threshold.

Figure 10 shows the SNR versus CNR threshold locus for the PLD.² Figure 11 presents the threshold $[C/(N_o 2f_b)]_T$ and the feedback

² R. E. Heitzman, "A Study of the Threshold Power Requirements of FMFB Receivers," *IRE Trans. on Space Electronics and Telemetry*, Vol. SET-8, Dec. 1962.

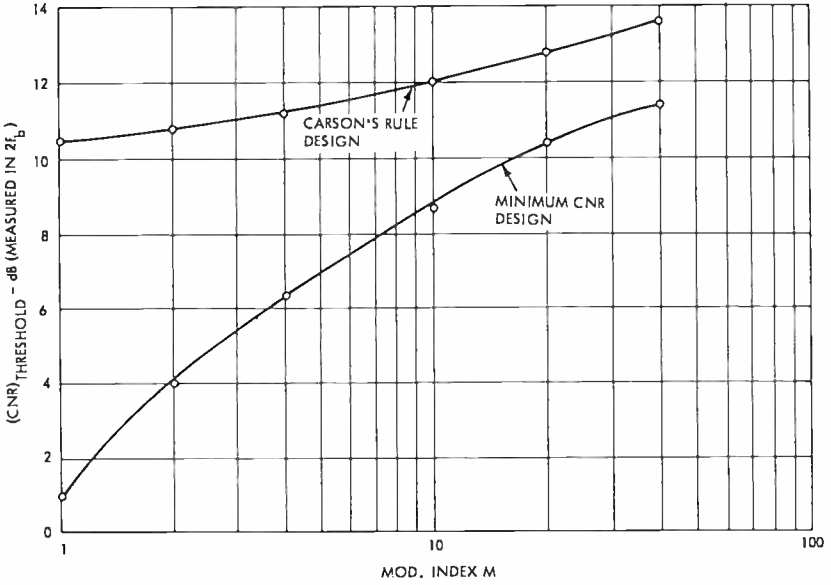


Fig. 8— $[C/(N_0 \cdot 2f_b)]_r$ versus M for the FMFB-FMFB.

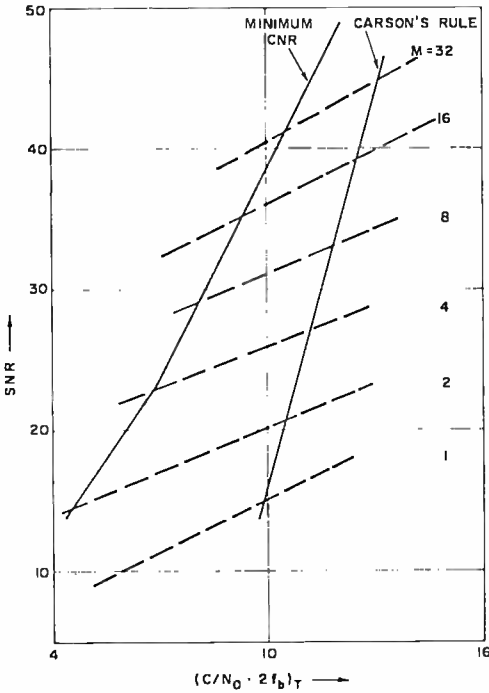


Fig. 9—FMFB-FMFB threshold bounds.

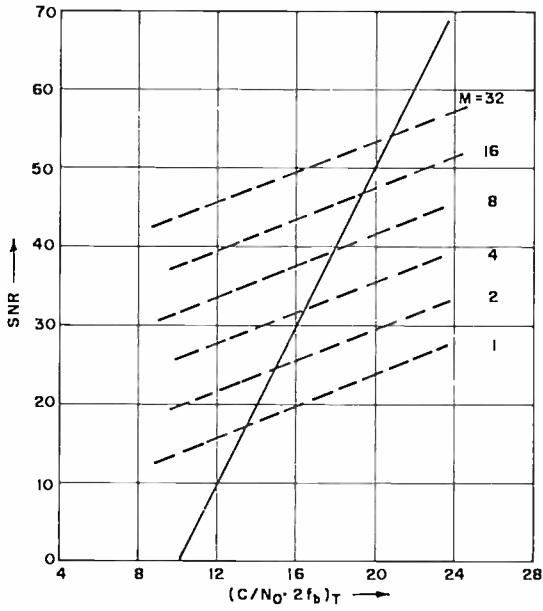


Fig. 10—Threshold bound of second-order PLD (damping factor—0.5).

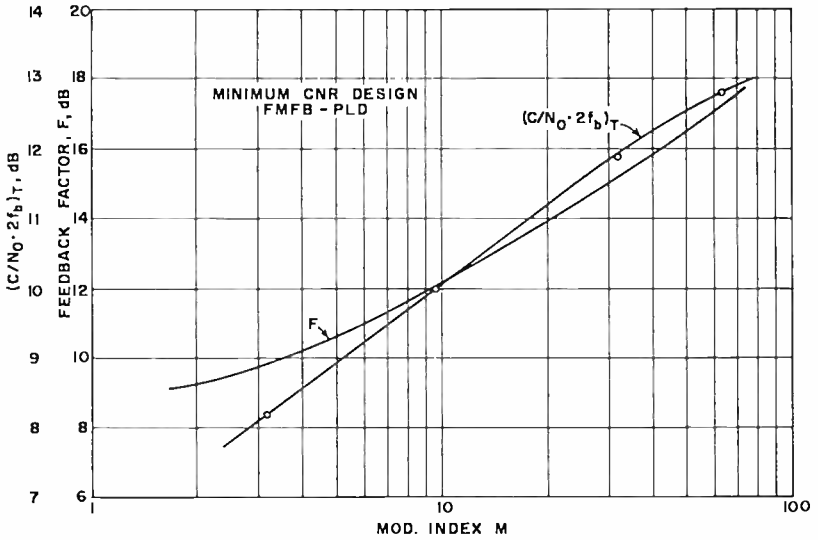


Fig. 11— $[C/(N_0 2f_b)]_T$ and feedback factor versus M for FMFB-PLD.

factor, F , as functions of the input modulation index, M . Minimum CNR design is assumed for the FMFB loop.

THE CLOSED-LOOP RESPONSE OF THE INNER LOOP

Both the PLD and FMFB present a second-order closed loop response of the form

$$K(S) = K \frac{S + S_1}{S^2 + 2 \xi \omega_o S + \omega_o^2}. \quad (11)$$

For a damping factor, ξ , of 0.5 in the PLD, the response reduces to

$$K(S) = K \frac{S + S_1}{S^2 + S_1 S + S_1^2}. \quad (12)$$

S_1 is the zero of the PLD open-loop transfer function;

$$H(S)_p = \frac{S_1(S + S_1)}{S^2}.$$

For the FMFB demodulator whose open-loop response is $G_o(S)$ in Equation (6), and given the feedback factor $F = A + 1$, the closed-loop response is

$$K(S) = \frac{G_o(S)}{1 + G_o(S)} = \frac{\frac{A\omega_b}{a} (S + a\omega_b)}{S^2 + \left(\sqrt{2} + \frac{A}{a} \right) \omega_b S + (1 + A)\omega_b^2}. \quad (13)$$

To realize the prescribed flat open-loop response in the compound loop, the base-band filter of the outer loop must be designed to include additional zeroes to cancel the second-order closed-loop poles associated with the inner loop. In addition, the transfer function of the filter includes the canceling zero for the i-f single-pole network and the two poles of the Butterworth response. The desired outer-loop filter transfer response is

$$H(S) = \frac{1}{K(S)} \frac{S + b'\omega_b}{S^2 + \sqrt{2} \omega_b S + \omega_b^2} \frac{A\omega_b}{b'}. \quad (14)$$

BASE-BAND FILTER SYNTHESIS

The objectives of the outer-loop synthesis can be summarized as follows:

- To secure a two-pole closed loop Butterworth response.
- To provide a canceling zero for the i-f pole in the outer loop.
- To provide the inverse response of the inner loop closed-loop response.

The grouping of the zeroes and poles in the desired base-band filter is a matter of realizability and, to some extent, convenience. It was found desirable to insert an isolating stage and realize the overall response as a product of two transfer functions:

$$H_o(S) = H_1(S)H_2(S)$$

$H_1(S)$ is designed to produce a set of complex zeroes corresponding to the complex poles of the closed-loop response of the inner loop. Incidental to this synthesis are two real poles. One of the poles is chosen to cancel the zero of the inner-loop response. The second is a dummy pole that is cancelled by a zero of the $H_2(S)$ filter.

The $H_2(S)$ transfer function contains the set of Butterworth complex poles, a real zero to cancel the i-f pole of the outer loop and a zero to cancel the dummy pole of $H_1(S)$.

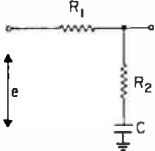
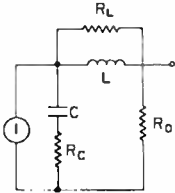
Table I presents the pertinent open-loop and closed-loop transfer functions. Figure 12 shows the Dasher Synthesis³ realization of $H_1(S)$ for the FMFB-FMFB. Column 1 of Figure 13 specifies the parameters for the inner loop. Column 2 specifies the parameters of $H_2(S)$ in the outer-loop filter. The constants a , b , and b' are plotted in Figures 14 and 15, and F is plotted versus M in Figure 7 for the Carson's Rule and Minimum CNR designs. Active filter synthesis procedure may also be applied to realize the required transfer functions using simpler networks. This implementation excludes the bandwidth minimizing zero.

EFFECT OF MODULATION

Some important qualifications are in order with respect to the effect of modulation. If noise in the SNR expression is measured with the modulation removed, we obtain optimistic results. It is known that the presence of modulation degrades threshold. The threshold performance calculated for the PLD accounts for the degradation due to signal modulation. The effect of modulation on the threshold of the FMFB has

³ J. G. Truxall, *Automatic Feedback Control System Synthesis*, McGraw Hill Book Co., 1965.

Table I—Base-Band Filter Realizations

	PLD	FMTB
FM Detector Loop (Inner Loop)		
Open-Loop Response of Inner Loop	$\frac{S_1(S + S_1)}{S^2}$	$\frac{A\omega_b}{\alpha} \frac{S + \alpha\omega_b}{S^2 + \sqrt{2}\omega_b S + \omega_b^2}$
Base-Band Filter of Inner Loop		
Closed-Loop Response of Inner Loop	$K \frac{S + S_1}{S^2 + S_1 S + S_1^2}$ for $\xi = 0.5$	$\frac{A\omega_b}{\alpha} (S + \alpha\omega_b)$ $S^2 + \left(\sqrt{2} + \frac{A}{\alpha} \right) \omega_b S + (1 + A)\omega_b^2$
Outer Loop Base-Band Filter $H(S) = H_1(S)H_2(S)$		
Section 1 $H_1(S)$	$\frac{S^2 + S_1 S + S_1^2}{(S + S_1)(S + dS_1)}$	$S^2 + \left(\sqrt{2} + \frac{A}{\alpha} \right) \omega_b S + (1 + A)\omega_b^2$ $(S + \alpha\omega_b)(S + d\omega_b)$
Section 2 $H_2(S)$	$\frac{(S + b'\omega_b)(S + d\omega_b)}{S^2 + \sqrt{2}\omega_b S + \omega_b^2}$	$\frac{(S + b'\omega_b)(S + d\omega_b)}{S^2 + \sqrt{2}\omega_b S + \omega_b^2}$

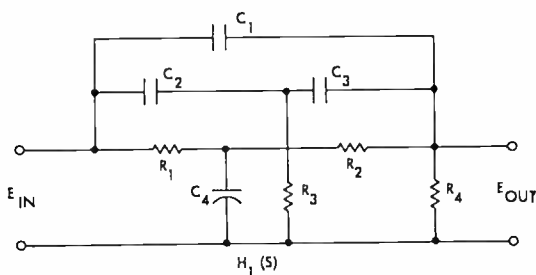


Fig. 12—The $H_1(S)$ section of the base-band filter.

Dasher Synthesis³ Realization of $H_1(S)$ for the FMFB-FMFB

$$C_1 = \frac{2\alpha_o}{\sigma_o}$$

$$R_1 = \frac{\alpha_o}{1 + \alpha_o}$$

$$C_2 = \frac{1 + \alpha_o}{\alpha_o} \left(\frac{\sigma_o - 2\alpha_o}{\sigma_o} \right)$$

$$R_2 = \frac{R_1}{\alpha_o}$$

$$C_3 = \alpha_o C_2$$

$$R_3 = \frac{1}{(1 + \alpha_o)(1 + 1/\alpha_o)(\sigma_o - 2\alpha_o)}$$

$$C_4 = (1 + \alpha_o) \left(1 + \frac{1}{\alpha_o} \right) \frac{1}{\sigma_o}$$

$$R_4 = \frac{1}{\sigma_o} \frac{da}{F - 1}$$

Divide all C 's by $m\omega_o\sqrt{F-1}$, all R 's by m ; m is any scale factor. Values a , b , b' are obtained from Figures 14 and 15, and F from Figure 7.

$$d = \frac{1}{2} + \frac{\sqrt{2} F - 2}{4} \frac{1}{a} + \frac{\sqrt{F-1}}{2}$$

$$\sigma_o = \frac{a + d}{2\sqrt{F-1}}$$

$$\alpha_o = \frac{\sqrt{2} + \frac{F-2}{a}}{2\sqrt{F-1}}$$

$$\alpha_o = \frac{1}{\sigma_o} \left(\frac{ad}{F-1} + 1 \right) \frac{1}{\sigma_o + \frac{1}{\sigma_o} - 2\alpha_o\sigma_o}$$

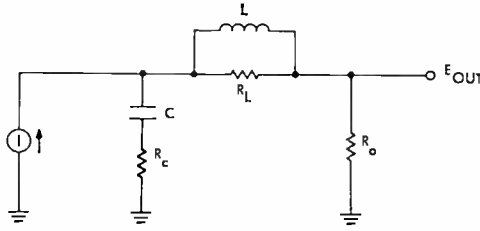


Fig. 13—Inner-loop filter and $H_2(S)$ section of outer-loop filter.

Parameters of the Inner Loop and of $H_2(S)$ in the Outer Loop

	Inner Loop	Outer Loop— $H_2(S)$
$R_c C$	$\frac{1}{b\omega_b}$	$\frac{1}{d\omega_b}$
$R_o C$	$\frac{1}{\omega_o}$	$\frac{1}{\omega_o}$
LC	$\frac{1}{\omega_b^2}$	$\frac{1}{\omega_n^2}$
R_L/L	$a\omega_b$	$b'\omega_b$
$\frac{\omega_b}{\omega_o}$	$\sqrt{2} - \frac{1}{b} - \frac{1}{a}$	$\sqrt{2} - \frac{1}{d} - \frac{1}{b}$
$\left(\frac{\omega_b}{\omega_n}\right)^2$	$1 - \frac{\sqrt{2}}{a} + \frac{1}{a^2}$	$1 - \frac{\sqrt{2}}{b'} + \frac{1}{b'^2}$
Values From Figs. 14, 15, and 7	a, b	a, b', F

$$d = \frac{1}{2} \frac{\sqrt{2}}{4} \frac{F - 2}{a} + \frac{\sqrt{F - 1}}{2}$$

not been found tractable, but it is known from experimental evidence that it is significant for the Minimum CNR design and much less significant for the Carson's Rule design.

It should not be concluded, therefore, that the Minimum CNR design produces, in all cases, lower threshold. In practice, an intermediate design defined by

$$B_i = 2f_b \left(k + \frac{M}{F} \right)$$

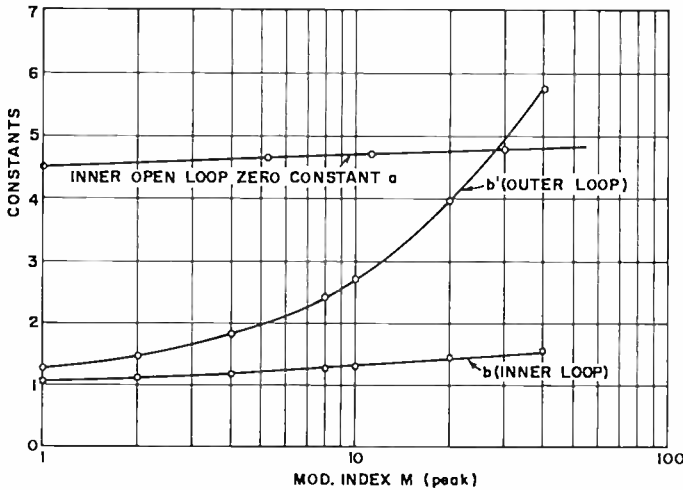


Fig. 14—Carson's rule design, constants a , b , and b' versus M .

is found more suitable, where k lies in the range of zero and one, depending on M . Except for the factor b , the synthesis procedure remains the same.

EXPERIMENTAL RESULTS

Compound loops were synthesized for a variety of signals. A FMFB-FMFB loop designed for single-voice-channel transmission was tested. The peak deviation was 10 kHz and the top base-band frequency 4 kHz; it had a deviation ratio of 2.5. A test tone of 1 kHz with ± 10 kHz deviation was used. The threshold CNR (1-dB down from linear extension) in a 28-kHz predetection bandwidth (Carson's rule) was 3 dB. Under identical conditions, the limiter discriminator exhibited a 10-dB threshold CNR and a second-order PLD a 5.5-dB threshold CNR.

A compound loop enclosing an improved PLD (extended range PLD or ERPLD, see Ref. (4)) was tested using single-voice-channel parameters and the test signal described above. A threshold CNR of 2 dB was realized in the 28-kHz bandwidth. The ERPLD device alone had a threshold CNR of 3 dB for the stated conditions.

The same loop was tested (after rescaling) for a base bandwidth of 15 kHz, and a threshold of 0 dB was realized in a 44-kHz Carson's rule predetection bandwidth.

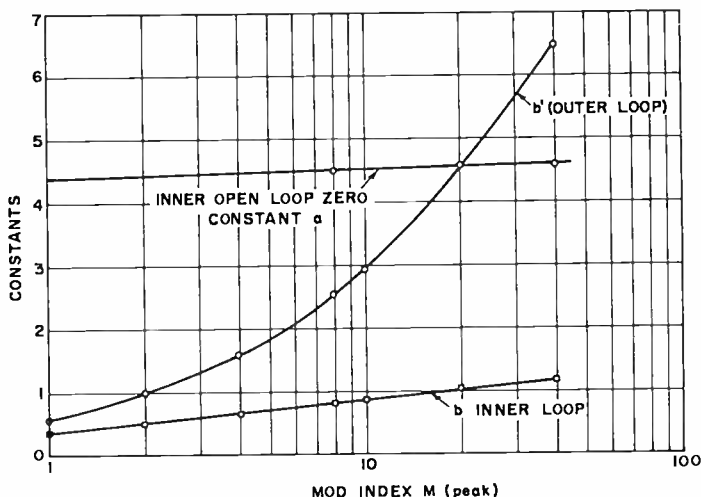


Fig. 15—Minimum CNR design, constants a , b , and b' versus M .

An FMFB-PLD loop was synthesized for a 12-channel FDM baseband having a 60-kHz base bandwidth. A threshold CNR of 4.5 dB in a 2.0 MHz predetection bandwidth was realized. The PLD threshold for the stated condition is 7 dB.

CONCLUSIONS

Reduced threshold is realized in multiple-FMFB and compound loops by means of a favorable trade off in open-loop and feedback thresholds. When the inner loop exhibits a lower threshold, a reduced feedback factor is required to bring the feedback threshold into coincidence. Conversely, applying iterative compressive feedback in a multistage FMFB system results in increased bandwidth compression

⁴ A. Acampora, A. Newton, "Use of Phase Subtraction to Extend the Range of a Phase Locked Demodulator," *RCA Review*, Vol. 27, p. 577, Dec. 1966.

and reduced open-loop threshold for a given feedback factor. It is then possible to bring the individual feedback and open-loop thresholds into coincidence at a lower level of CNR.

It was determined that minimum threshold is realized when all feedback factors are equal. A base-band filter synthesis was realized that provides the established optimal open-loop transfer function for a loop enclosing a second-order system.

Threshold extension was demonstrated experimentally for an FMFB-FMFB and FMFB-PLD loops for single voice channel and FDM-FM operation.

DOUBLE-STREAM INTERACTION IN A THIN SEMICONDUCTOR LAYER

BY

B. B. ROBINSON AND B. VURAL*

RCA Laboratories
Princeton, New Jersey

Summary—The two-fluid model is used, with the aid of the quasistatic approximation, to derive the dispersion relation for slow waves in a semi-conducting slab. It is assumed that the two fluids experience relative drift in the plane of the slab while under the influence of a static magnetic field that lies in the slab with arbitrary orientation. Particular emphasis is placed on the limit of a thin plasma layer, because of the possible relevance to radiation observed from InSb under conditions where Suhl or pinch effect creates a dense plasma of small dimensions. It is concluded that, neglecting diffusion, the dispersion relation for streaming in a thin layer with arbitrary magnetic field orientation is identical to the dispersion relation for an infinite system under the influence of a transverse magnetic field. It has already been shown that this dispersion relation predicts instability at frequencies pertinent to InSb observations. It is further concluded that the thermal damping, which necessitates extremely high drift velocities in the infinite case, can be reduced in a finite system.

INTRODUCTION

IN this paper we derive the dispersion relation for slow waves supported by a plasma layer consisting of electrons and holes drifting in the plane of the layer. The carriers are subjected to a static magnetic field that lies in the layer and is oriented at an arbitrary angle with respect to the drift direction (see Figure 1). The analysis is based on the two-fluid hydromagnetic model and the quasistatic approximation. Particular emphasis is placed on the limit of a very thin layer, $ka \rightarrow 0$. It is shown that a set of slow waves supported by the thin layer system obey a dispersion relation that, neglecting diffusion, is identical to the relation for slow waves in an infinite electron-hole plasma acted on by a transverse magnetic field.¹ It has already been shown that this dispersion relation admits of two potentially unstable roots, one of which, a collision-induced mode, shows correlation

* Presently with the Department of Electrical Engineering, The City College of The City University of New York, New York.

¹ B. B. Robinson, "A Collision Induced Instability in Semiconductor Plasmas," *RCA Review*, Vol. 28, p. 366, June 1967.

with observed microwave emission from InSb.^{1,2} Unlike the modes in the infinite system, the thin-layer modes are transverse waves and are not essentially space charge in nature. For this reason, they are less subject to the thermal damping effects that severely restrict the possible instability in the infinite system.

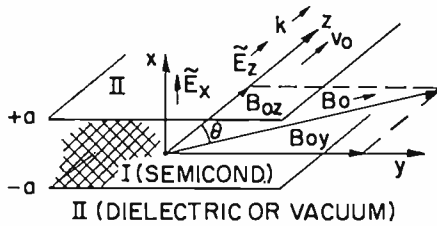


Fig. 1—Geometry, coordinate system and field configuration, $\mathbf{E}(E_x, 0, E_z)$, \mathbf{B}_0 is in zy -plane, and makes an angle θ with z -axis.

THE DISPERSION RELATION

We assume the validity of the hydrodynamic model for the plasma, and consider the self-consistent solution of the Maxwell's equations and the linearized equations of motion for the geometry shown in Figure 1. We further make the quasistatic and small-signal assumptions with all the perturbations of the form $\phi \sim \phi(x) \exp(i\omega t - ikz)$. Finally, we shall neglect diffusion. The perturbations in the plasma layer are described by a linearized equation of momentum conservation.

$$i(\omega - k v_{oa} - i\nu_a) \mathbf{v}_a^1 = \frac{q_a}{m_a} (\mathbf{E}^1 + \mathbf{v}_a^1 \times \mathbf{B}), \tag{1}$$

and a linearized equation of particle conservation,

$$i(\omega - k v_{oa}) n_a^1 = n_{oa} \left(ik v_{az}^1 - \frac{\partial v_{ax}^1}{\partial x} \right) \tag{2}$$

where ω is the active frequency of the system, k is the wave number, \mathbf{E}^1 is the a-c electric field, and \mathbf{B} is the applied magnetic field. Each

² G. A. Swartz and B. B. Robinson, "Coherent Microwave Emission from Indium-Antimonide Structures," *Appl. Phys. Letters*, Vol. 9, p. 232, 15 Sept. 1966.

³ G. A. Swartz, "Coherent Microwave Emission from Bulk P-Type InSb," *Bull. of Am. Phys. Soc.*, Vol. 12, p. 384, 27 March 1967.

carrier species (a) is characterized by a steady-state drift velocity in the z -direction (v_{0a}), a velocity perturbation (v_a^1), a steady-state density (n_{0a}), a density perturbation (n_a^1), a charge per carrier (q_a), an effective carrier mass (m_a), and a collision frequency for momentum transfer (ν_a). Finally, with the quasi-static approximation, Maxwell's equations reduce to

$$\mathbf{E}^1 = \nabla \phi^1 \quad (3)$$

and

$$\frac{\partial^2 \phi^1}{\partial x^2} - k^2 \phi^1 = - \frac{1}{\epsilon_l} \sum_a n_a^1 q_a \quad (4)$$

where ϵ_l is the lattice dielectric constant in region I of Figure 1.

Equation (1) can be rewritten as an expression for the a-c velocity,

$$\mathbf{v}_a^1 = \frac{q_a}{m_a(\omega_{ca}^2 - \Omega_a^2)} \left[i\Omega_a \mathbf{E}^1 + \mathbf{E}^1 \times \omega_{ca} - \frac{i}{\Omega_a} \left(\mathbf{E}^1 \cdot \frac{q_a}{m_a} \mathbf{B} \right) \frac{q_a}{m_a} \mathbf{B} \right] \quad (5)$$

where $\Omega_a = \omega - kv_{0a} - i\nu_a$ and $\omega_{ca} = \frac{q_a}{m_a} \mathbf{B}$. Combining Equations (2)

and (5), one obtains an expression for n_a^1 ,

$$n_a^1 = \frac{n_{0a} q_a}{m_a(\omega - kv_{0a})(\Omega_a^2 - \omega_{ca}^2)\Omega_a} \left[\Omega_a^2 \frac{\partial^2 \phi}{\partial x^2} - k^2 \phi (\Omega_a^2 - \omega_{ca}^2) \right], \quad (6)$$

which, upon substitution into Equation (4), leads to

$$\frac{\partial^2 \phi}{\partial x^2} - \beta^2 \phi = 0 \quad (7)$$

where

$$\beta^2 = \frac{\alpha_2}{\alpha_1} k^2$$

$$\alpha_1 = \left[1 - \sum_a \frac{\omega_{pa}^2 \Omega_a}{(\omega - kv_{0a})(\Omega_a^2 - \omega_{ra}^2)} \right], \quad (8)$$

$$\alpha_2 = \left[1 - \sum_a \frac{\omega_{pa}^2 (\Omega_a^2 - \omega_{ra}^2)}{\Omega_a (\omega - kv_{0a})(\Omega_a^2 - \omega_{ra}^2)} \right], \quad (9)$$

$$\omega_{pa}^2 = \frac{n_{0a} q_a^2}{\epsilon_f m_a}.$$

In the plasma layer, region I in Figure 1, the fields are of the form

$$E^1_{x'} = [A \exp \{\beta x\} + B \exp \{-\beta x\}] \exp \{i\omega t - ikz\} \quad (10)$$

$$E^1_{z'} = -\frac{ik}{\beta} [A \exp \{\beta x\} - B \exp \{-\beta x\}] \exp \{i\omega t - ikz\}. \quad (11)$$

In the dielectric region, one has

$$\frac{\partial^2 \phi}{\partial x^2} = k^2 \phi \quad (12)$$

$$E^1_x = \begin{cases} C \exp \{-kx\} \exp \{i\omega t - ikz\} & (x > a), \\ D \exp \{kx\} \exp \{i\omega t - ikz\} & (x < -a), \end{cases} \quad (13)$$

$$E^1_z = \begin{cases} iC \exp \{-kx\} \exp \{i\omega t - ikz\} & (x > a), \\ -iD \exp \{kx\} \exp \{i\omega t - ikz\} & (x < -a). \end{cases} \quad (14)$$

At the plasma-dielectric interfaces, one must match the components E_z and D_x where \mathbf{D} is the displacement vector. In the dielectric, the displacement vector is defined by

$$D^1_{x'} = \epsilon_f E^1_{x'} \quad (15)$$

and in the plasma it is defined by⁴

$$D^1_{x'} = \epsilon_f E^1_{x'} - i \sum_a \frac{n_{0a} q_a v^1_{ax}}{(\omega - kv_{0a})} \quad (16)$$

$$= \epsilon_f [\alpha_1 E^1_{x'} + \alpha_2 E^1_{z'}],$$

⁴ B. J. Maxum and A. W. Trivelpiece, "Two-Stream Cyclotron and Plasma Wave Interactions," *Jour. Appl. Phys.*, Vol. 35, p. 481, Feb. 1965.

where

$$\alpha_3 = i \sum_a \frac{\omega_{pa}^2 \omega_{ca\eta}}{(\omega - kv_{oa})(\omega_{ca}^2 - \Omega_a^2)}. \quad (17)$$

The boundary conditions of $x = \pm a$ provide four equations. Elimination of the constants C and D reduces these equations to

$$0 = \left(1 + \frac{\epsilon_I}{\epsilon_{II}} \alpha_1^{1/2} \alpha_2^{1/2} - i \frac{\epsilon_I}{\epsilon_{II}} \alpha_3 \right) A \exp \{ \beta a \} \quad (18)$$

$$+ \left(-1 + \frac{\epsilon_I}{\epsilon_{II}} \alpha_1^{1/2} \alpha_2^{1/2} + i \frac{\epsilon_I}{\epsilon_{II}} \alpha_3 \right) B \exp \{ -\beta a \},$$

and

$$0 = \left(1 - \frac{\epsilon_I}{\epsilon_{II}} \alpha_1^{1/2} \alpha_2^{1/2} + i \frac{\epsilon_I}{\epsilon_{II}} \alpha_3 \right) A \exp \{ -\beta a \} \quad (19)$$

$$+ \left(-1 - \frac{\epsilon_I}{\epsilon_{II}} \alpha_1^{1/2} \alpha_2^{1/2} - i \frac{\epsilon_I}{\epsilon_{II}} \alpha_3 \right) B \exp \{ \beta a \},$$

which admit of a nontrivial solution only if

$$\left(1 + \frac{\epsilon_I}{\epsilon_{II}} \alpha_1^{1/2} \alpha_2^{1/2} - i \frac{\epsilon_I}{\epsilon_{II}} \alpha_3 \right) \left(1 + \frac{\epsilon_I}{\epsilon_{II}} \alpha_1^{1/2} \alpha_2^{1/2} + i \frac{\epsilon_I}{\epsilon_{II}} \alpha_3 \right) \exp \{ 2\beta a \} \quad (20)$$

$$- \left(1 - \frac{\epsilon_I}{\epsilon_{II}} \alpha_1^{1/2} \alpha_2^{1/2} - i \frac{\epsilon_I}{\epsilon_{II}} \alpha_3 \right) \left(1 - \frac{\epsilon_I}{\epsilon_{II}} \alpha_1^{1/2} \alpha_2^{1/2} + i \frac{\epsilon_I}{\epsilon_{II}} \alpha_3 \right) \exp \{ -2\beta a \} = 0.$$

For the special case of a transverse magnetic field ($\theta = \pi/2$), Equations (7), (8) and (9) indicate that $\beta = k$, and Equation (20) becomes

$$\left[1 + \left(\frac{\epsilon_I}{\epsilon_{II}} \alpha_1 \right)^2 + \left(\frac{\epsilon_I}{\epsilon_{II}} \alpha_3 \right)^2 \right] \sinh ka + 2 \frac{\epsilon_I}{\epsilon_{II}} \alpha_1 \cosh ka = 0. \quad (21)$$

Equation (21) is a quadratic equation for α_1 . In the limit of an infinitely thin layer, the root of interest is†

$$\alpha_1 \approx -\frac{ka}{2} \frac{\epsilon_I}{\epsilon_{II}} \alpha_3^2 \xrightarrow{ka \rightarrow 0} 0 \quad (22)$$

or

$$1 - \sum_a \frac{\omega_{pa}^2 \Omega_a}{(\omega - kv_{aa})(\Omega_a^2 - \omega_{ca}^2)} \approx 0. \quad (23)$$

It is shown in the Appendix that Equation (23) is the dispersion relation in the thin-layer limit ($ka \rightarrow 0$) with arbitrary magnetic field orientation when diffusion is neglected. When comparing the theory to a specific experimental situation, one must consider whether or not the actual layer is sufficiently thin to make the right-hand side of Equation (22) negligible. For example, numerical calculations using parameters appropriate for InSb with $n \approx 10^{14} \text{ cm}^{-3}$, $p \approx 3 \times 10^{14} \text{ cm}^{-3}$ and $B \approx 1000$ gauss (parameters pertinent to the observation of coherent emission when electrons are injected into p-InSb at 77°K³) indicates that the correction term is negligible if $a \lesssim 10^{-4} \text{ cm}$. The Suhl layer created by injecting electrons into a 1000-gauss transverse field is about $2.5 \times 10^{-5} \text{ cm}$ thick.⁵ On the other hand, initial calculations using the much higher densities and magnetic fields pertinent to the microwave noise observed under breakdown conditions in n-InSb⁶ indicate that although Equation (23) may be useful for qualitative discussion, the correction term must be included in any quantitative considerations. In the remainder of this paper we shall consider the thin-layer limit, Equation (23).

† In this discussion of limits, we have assumed that α_n remains finite. Thus, we cannot accept the roots $\omega - kv_n = 0$ or $\omega_{ca} = \Omega_a^2$. Since these are stable roots, they do not interest us. In our discussion of the physical nature of the collision-induced mode, we shall consider the hypothetical collisionless case in order to illustrate the role of collisions. Strictly speaking, in any layer of nonzero thickness, we can only consider this mode when some collisions, however small, are present. This difficulty with the $ka \rightarrow 0$ limit disappears when one considers real semiconductors, which have large collision frequencies and for which $\alpha_1 = 0$ has no root of the form $\omega - kv_n = 0$.

³ W. Shockley, *Electrons and Holes in Semiconductors*, D. Van Nostrand, Co., Princeton, 1950, p. 327.

⁶ R. D. Larrabee and W. A. Hicinbotham, "Current Oscillations and Microwave Emission in Indium Antimonide," *IEEE Trans. on Electron Devices*, Vol. ED-13, p. 121, Jan. 1966.

DISCUSSION

It is concluded that, neglecting diffusion, the dispersion relation, Equation (23), for waves in a thin electron-hole plasma layer with relative streaming and applied magnetic field in the plane of the layer is identical to the dispersion relation for space-charge waves in an infinite electron-hole plasma with streaming transverse to the magnetic field.¹ It is important to stress that, in spite of this similarity of dispersion relation, the waves in the two systems are quite different.

The waves in the infinite system are purely longitudinal, the E -fields are parallel to the direction of propagation, and are, by their very nature, space-charge waves. Thermal damping due to the diffusion of the associated space-charge imposes the stringent condition that the electron drift velocity must be comparable to or exceed the electron thermal velocity for instability to occur. In addition, because of the longitudinal nature of the waves, a microscopic theory reveals additional thermal damping of the Landau type. The latter damping can be reduced by the presence of a strong transverse component of magnetic field.⁷

Space charge is not an essential feature of the waves in the thin layer. In fact, the space charge is identically zero in the limit $\theta \rightarrow \pi/2$ and in the limit $B \rightarrow 0$. This can be seen immediately from Equation (4) by noting that, when $\beta = k$, $\nabla^2\phi = 0$. Thermal restrictions will not be as severe for these waves.

Consider the configuration of the waves in the thin layer. The coordinate system is defined in Figure 1. Examination of the Equations (10), (11) and (19) in the limit $ka \rightarrow 0$, $\beta a \rightarrow 0$ and $\alpha_1 \rightarrow 0$ leads to

$$\mathbf{E}^{11} = [E \hat{e}_r - i k r E \hat{e}_z] \exp \{i\omega t - ikz\} \quad (24)$$

$$\begin{aligned} ka \rightarrow 0 \\ \longrightarrow E \exp \{i\omega - ikz\} \hat{e}_r. \end{aligned}$$

The waves are transverse waves in the limit $ka \rightarrow 0$. The associated fluid velocities, Equation (5), are

$$\mathbf{v}_a^1 = \frac{q_a}{m_a(\omega_{ca}^2 - \Omega_a^2)} \left[i\Omega_a E \hat{e}_r + E \hat{e}_r \times \frac{q_a}{m_a} \mathbf{B} \right]. \quad (25)$$

The fluid velocities, in general, have a component in the r -direction, a

⁷ I. B. Bernstein, "Waves in a Plasma in a Magnetic Field," *Phys. Rev.*, Vol. 109, p. 10, Jan. 1958.

rippling of the fluid layer, and in the layer a component perpendicular to the magnetic field.

The field configuration in the dielectric can be determined by the boundary conditions,

$$E_{z'}^{(1)} = E_{z'}^{(2)} = 0, \quad (26)$$

and

$$E_{x'}^{(1)} = \frac{D_x}{\epsilon_{11}} = \frac{\epsilon_1}{\epsilon_{11}} \alpha_1 E_{x'}^{(2)} = 0. \quad (27)$$

The external fields vanish in the limit $ka \rightarrow 0$. Surface charges form that are sufficient to confine the field energy in the plasma layer.

It has already been demonstrated, in the context of the infinite plasma model, that dispersion relation, Equation (23), admits of two potentially unstable roots.¹ An analogous pair of unstable roots must also exist for the thin plasma layer. Of particular interest to our present discussion is the collision-induced mode, which has already been shown to have some correlation with experiments. If one assumes $\omega - kv_m = 0$, and $v_e \ll \omega_{ce}$, Equation (22) becomes

$$kv_m = \omega - \frac{i\nu_e \omega_{pe}^2}{\omega_{ce}^2 \left[1 + \frac{\omega_{ph}^2}{\omega_{ch}^2 - \omega^2} + \frac{\omega_{pe}^2}{\omega_{ce}^2} \right]}. \quad (28)$$

Equation (28) indicates a convective instability when

$$v_e < 0$$

and

$$\omega_{ch}^2 < \omega^2 < \omega_{ch}^2 + \frac{\omega_{ph}^2 \omega_{ce}^2}{\omega_{ce}^2 + \omega_{pe}^2}. \quad (29)$$

To understand this collision-induced instability, it is useful to consider the problem from the mode interaction point of view.¹ In this picture, the hole and electron fluids are considered as semi-independent systems that are weakly coupled. Each fluid supports a set of plasma

waves. When their relative drift is sufficient to Doppler shift an electron wave into synchronism with a hole wave, an unstable resonant coupling between the two systems is possible under appropriate conditions determined by energy considerations. When no collisions are present, each fluid supports waves described by the relation

$$0 = 1 + \frac{\omega_{pu}^2(\omega - kv_{ou})}{(\omega - kv_{ou})[\omega_{ru}^2 - (\omega - kv_{ou})^2]} \quad (30)$$

where again diffusion has been omitted. This relation yields three solutions:

$$kv_{ou} = \omega \pm \sqrt{\omega_{ru}^2 + \omega_{pu}^2} \quad (31)$$

and

$$kv_{ou} = \omega \quad (32)$$

The first two roots are the thin-layer analogs of the familiar fast and slow hybrid waves in the infinite system. As indicated by Equations (24) and (25), the wave configuration is completely different in the thin layer. Since the third solution, Equation (32), plays a central role in the collision-induced instability, it is useful to consider its significance. The third root implies that in the rest frame of the electron fluid ($v_{oc} = 0$) there are two steady-state ($\omega = 0$) solutions to the equations of motion. In addition to the usual homogeneous steady state ($\mathbf{E} = 0$, $n = n_0$, $\mathbf{v} = 0$), there is an inhomogeneous steady state with

$$\mathbf{E} = E \exp\{-ikz\} \hat{e}_z \quad (33)$$

and, from Equation (5),

$$\mathbf{v} = \frac{q}{m_e \omega_{ce}^2} [\mathbf{E} \times \omega_{ce} \hat{e}_z] \quad (34)$$

The inhomogeneous E field is exactly balanced by the Lorentz force, created by the inhomogeneous fluid velocity, that lies in the plasma layer ($v_{cx} = 0$) and is perpendicular to the applied magnetic field. When this inhomogeneous steady state is drifted along the z -axis ($v_{oc} \neq 0$), it takes the form of a wave traveling at the electron drift velocity. The a-c currents associated with this wave are transverse to

all of the electric fields associated with the mode coupling problem ($v_{r,r} = 0$ and $\mathbf{E} \sim E \hat{e}_r$). When collisions are added, one obtains

$$\mathbf{E} = E e^{-ikz} \hat{e}_r \quad (35)$$

and

$$\mathbf{v} \approx \frac{q_c}{m_c \omega_{ce}^2} \left[- \frac{v_c \omega_{ce}^2}{\omega_{ce} + \omega_{pc}} \mathbf{E} + \mathbf{E} \times \frac{q_c}{m_c} \mathbf{B} \right] \quad (36)$$

The collisions have introduced an x component of a-c current to the wave configuration. It can now interact with the fields associated with the waves carried by the hole system and, as dispersion relation Equation (28) indicates, unstable interaction with the fast hole-hybrid wave is now possible.

CONCLUSION

The double-stream interaction in a very thin plasma layer subjected to a magnetic field oriented at an arbitrary angle with respect to the drifting direction is described by the same dispersion relation, Equation (23), which, neglecting diffusion, describes double-stream interaction in an infinite plasma subjected to a transverse field. This dispersion relation admits of two potentially unstable roots. One of these roots is a collision-induced interaction that predicts instability in the frequency range of interest for the conditions pertinent to observed microwave emission from InSb, i.e., where high drift velocities in the presence of a transverse component of magnetic field create a thin plasma layer via the Suhl effect. The waves in the thin layer are transverse waves and are free of space-charge when the applied magnetic field is perpendicular to the streaming direction. They are, therefore, less subject to the thermal damping effects that suppress instability in the infinite model.

The predicted collision-induced mode has been compared in detail to the coherent microwave radiation emitted from p-InSb. This comparison, which indicates good correlation between theory and experiment, will be the subject of a forthcoming paper.

APPENDIX

In This Appendix, the general dispersion relation for the plasma layer of Figure 1, Equation (20), will be examined for the case $\theta \neq \pi/2$ in the thin-layer limit.

Since, in general, $\beta \neq k$, one must explore the limits of βa as $ka \rightarrow 0$. For this purpose, it will be assumed that†

$$\frac{\beta}{k} = \frac{\alpha_2^{1/2}}{\alpha_1^{1/2}} \xrightarrow{ka \rightarrow 0} \frac{\bar{\beta}}{(ka)^n}$$

where $\bar{\beta}$ is some finite number. When $n > 0$, Equation (8) implies that either $\alpha_1 \rightarrow 0$, $\Omega_h \rightarrow 0$, or $\Omega_w \rightarrow 0$. Since the last two possibilities indicate damped waves, only the possibility $\alpha_1 \rightarrow 0$ will be considered. When $n < 0$, Equation (9) implies that $\alpha_2 \rightarrow 0$. The quantity βa can conceivably go to three limits:

(i) $\beta a \rightarrow \infty$, $n > 1$, $\alpha_1 \rightarrow (ka)^{2n}$: with these limits, Equation (20) leads to $1 + [(\epsilon_I' \epsilon_{II}) \alpha_3]^2 \rightarrow 0$, which is inconsistent with $\alpha_1 \rightarrow 0$.

(ii) $\beta a \rightarrow \text{finite}$, $n = 1$, $\alpha_1 \rightarrow (ka)^{2n}$. With these limits, Equation (20) leads to the same result as (i).

(iia) $\beta a \rightarrow 0$, $0 < n < 1$, $\alpha_1 \rightarrow (ka)^{2n}$. Equation (20) leads to $\alpha_1 \sim \bar{\beta}^2 (ka)^{2-2n}$, which is consistent if $n = 1/2$.

(iib) $\beta a \rightarrow 0$, $n = 0$, $\bar{\beta}^2 \alpha_1 = \alpha_2$. Equation (20) leads to $\bar{\beta}^2 \alpha_1 = \alpha_2 \rightarrow 0$, which is inconsistent.

(iic) $\beta a \rightarrow 0$, $n < 0$, $\alpha_2 \rightarrow (ka)^{-2n}$. Equation (20) leads to $\alpha_2 \sim (ka)^{2-2n}$, which is not consistent for any value of n .

Possibility (iia) is the only self-consistent one. It is concluded that for arbitrary values of θ ,

$$\alpha_1 = 1 + \sum_a \frac{\omega_{pa}^2 \Omega_a}{(\omega - kv_{aa})(\omega_{ca}^2 - \Omega_a^2)} = 0.$$

This is identical to the dispersion relation, Equation (23), derived in the text for the case $\theta = \pi/2$. It should be noted that when $\theta \neq \pi/2$,

$$\nabla^2 \phi \neq 0$$

There is, in general, space charge associated with the wave. The space charge is identically zero only in the limit $\theta = \pi/2$ and in the limit $B = 0$.

MANIPULATION OF SCULPTURED SURFACES

BY

E. P. HELPERT

RCA Laboratories
Princeton, New Jersey

Summary—The maximum normal curvature of a surface $x = x(s,t)$, $y = y(s,t)$, $z = z(s,t)$ is found by utilizing the first and second fundamental forms of the surface. The differential geometry is further exploited to derive the directions of principal curvature at any surface point. These directions are then used to compute maximum and minimum normal curvature at any point on the surface.

INTRODUCTION

IN machining a part using a numerically controlled milling machine, the optimum radius of the ball cutter is, ideally, the smallest radius of curvature that occurs on the part surface. This value of the ball radius is optimum because a smaller ball would increase computing time and obviously increase machining time, while a larger ball would undercut the desired surface.

This paper mathematically defines the radius of curvature of a "sculptured surface" (a term frequently used to refer to intricate part surfaces) and gives a formula to determine the minimum radius of curvature at any point on the surface.

In addition to the determination of the optimum cutter diameter, the minimum radius of curvature can also be used to determine the number and coarseness of cuts to be made with the milling machine. In more theoretical applications involving sculptured surfaces, curvature information is of use in determining the closeness of fit of a given surface to a desired mesh of points. The metric in this instance might be the integral of the curvature squared over a given surface path.

The paper concludes with a discussion of the implementation of the radius of curvature calculation in FMILL, a part-design programming language.

MATHEMATICAL COMPUTATIONS

We are given a surface represented in parametric form,

$$\mathbf{R} = \mathbf{R}(s,t) = x(s,t)\mathbf{i} + y(s,t)\mathbf{j} + z(s,t)\mathbf{k},$$

where x , y and z are single-valued functions of s and t , possess con-

tinuous partial derivatives of all orders in s and t , and have Taylor series expansions about any point on the surface. We would like to machine a solid piece of material using a hemispherical cutting tool of radius R so that the resulting work conforms to this surface. A single point of the tool center locus can be generated by considering a point on the surface

$$(x_o, y_o, z_o) = (x(s_o, t_o), y(s_o, t_o), z(s_o, t_o)),$$

calculating the normal vector to the surface at this point, then moving out a distance R from the point along the direction of the normal vector. This would guarantee tangency of the cutting sphere to the surface at (x_o, y_o, z_o) . The entire cutter center locus can be generated by repeating the calculation for each point on the surface. (In practice, a mesh of points would constitute the cutter locus, with a predetermined tolerance determining the coarseness of this mesh).

It seems obvious that a necessary condition for faithful reproduction of the desired surface is that the hemispherical cutter have a radius less than or equal to R , where $1/R$ is the maximum normal curvature of the desired surface. The condition above is necessary (but not sufficient) since the differential geometric theory used here is local in nature.

We now proceed to calculate the maximum normal curvature of the surface.

Consider a surface $\mathbf{R} = \mathbf{R}(s, t) = x(s, t)\mathbf{i} + y(s, t)\mathbf{j} + z(s, t)\mathbf{k}$ at the point

$$x_o = x(s_o, t_o), y_o = y(s_o, t_o), z_o = z(s_o, t_o).$$

We assume that $R(s, t)$ has continuous derivatives of all orders and has a Taylor series expansion about the point (s_o, t_o) . Since the vectors $\partial\mathbf{R}/\partial s$ and $\partial\mathbf{R}/\partial t$ are tangent to the surface along the curves $R(s, a)$ and $R(b, t)$ respectively, where a and b are constants, the vector $(\partial\mathbf{R}/\partial s) \times (\partial\mathbf{R}/\partial t)$ is normal to the surface. We now construct the normal unit vector

$$\mathbf{N} = \frac{\frac{\partial\mathbf{R}}{\partial s} \times \frac{\partial\mathbf{R}}{\partial t}}{\left| \frac{\partial\mathbf{R}}{\partial s} \times \frac{\partial\mathbf{R}}{\partial t} \right|}$$

at the point (s_o, t_o) and consider one of an infinite number of planes

containing this normal. The intersection of this plane with the surface is a curve called a *normal section*. This curve can be represented by $R = R[s(u), t(u)]$ where there can be some degree of arbitrariness in the variable u (e.g., u may be arc length along R). Along this curve, we have

$$d\mathbf{R} = \left(\frac{\partial \mathbf{R}}{\partial s} \frac{ds}{du} + \frac{\partial \mathbf{R}}{\partial t} \frac{dt}{du} \right) du, \tag{1}$$

so that $d\mathbf{R}$ is completely specified when ds and dt are known. Hence the notation (ds, dt) specifies a given direction on the surface. The curvature of this particular normal section at the point (s_0, t_0) is called the *normal curvature* of the surface at (s_0, t_0) in the direction (ds, dt) .

NORMAL CURVATURE CALCULATION

To compute the curvature of one of these normal sections in the direction (ds, dt) we start by defining $d\sigma$ as the length of arc along the normal section. The unit tangent vector to this curve is given by the relation

$$\mathbf{T} = \frac{d\mathbf{R}}{d\sigma} = \frac{\partial \mathbf{R}}{\partial s} \frac{ds}{d\sigma} + \frac{\partial \mathbf{R}}{\partial t} \frac{dt}{d\sigma}. \tag{2}$$

The normal curvature unit vector \mathbf{N} and the normal curvature K_n are defined by the equation

$$\frac{d\mathbf{T}}{d\sigma} = K_n \mathbf{N}, \tag{3}$$

and since \mathbf{T} is a unit vector,

$$\mathbf{N} \cdot \mathbf{T} = 0. \tag{4}$$

Differentiating Equation (2) with respect to σ yields

$$\begin{aligned} \frac{d\mathbf{T}}{d\sigma} = K_n \mathbf{N} = \frac{d^2\mathbf{R}}{d\sigma^2} = \frac{\partial^2\mathbf{R}}{\partial s^2} \left(\frac{ds}{d\sigma} \right)^2 + 2 \frac{\partial^2\mathbf{R}}{\partial s \partial t} \frac{ds}{d\sigma} \frac{dt}{d\sigma} + \frac{\partial^2\mathbf{R}}{\partial t^2} \left(\frac{dt}{d\sigma} \right)^2 \\ + \frac{\partial \mathbf{R}}{\partial s} \frac{d^2s}{d\sigma^2} + \frac{\partial \mathbf{R}}{\partial t} \frac{d^2t}{d\sigma^2} \end{aligned} \tag{5}$$

and

$$K_n = \mathbf{N} \cdot (K_n \mathbf{N}) = \left(\mathbf{N} \cdot \frac{\partial^2 \mathbf{R}}{\partial s^2} \right) \left(\frac{ds}{d\sigma} \right)^2 + 2 \left(\mathbf{N} \cdot \frac{\partial^2 \mathbf{R}}{\partial s \partial t} \right) \frac{ds}{d\sigma} \frac{dt}{d\sigma} + \left(\mathbf{N} \cdot \frac{\partial^2 \mathbf{R}}{\partial t^2} \right) \left(\frac{dt}{d\sigma} \right)^2, \quad (6)$$

since

$$\mathbf{N} \cdot \frac{\partial \mathbf{R}}{\partial s} = \mathbf{N} \cdot \frac{\partial \mathbf{R}}{\partial t} = 0.$$

Hence,

$$K_n = \frac{e(ds)^2 + 2f(ds)(dt) + g(dt)^2}{(d\sigma)^2}, \quad (7)$$

where

$$e = \mathbf{N} \cdot \frac{\partial^2 \mathbf{R}}{\partial s^2} \quad (8)$$

$$f = \mathbf{N} \cdot \frac{\partial^2 \mathbf{R}}{\partial s \partial t} \quad (9)$$

$$g = \mathbf{N} \cdot \frac{\partial^2 \mathbf{R}}{\partial t^2} \quad (10)$$

Now

$$(d\sigma)^2 = d\mathbf{R} \cdot d\mathbf{R} = \left(\frac{\partial \mathbf{R}}{\partial s} \cdot \frac{\partial \mathbf{R}}{\partial s} \right) ds^2 + 2 \left(\frac{\partial \mathbf{R}}{\partial s} \cdot \frac{\partial \mathbf{R}}{\partial t} \right) ds dt + \left(\frac{\partial \mathbf{R}}{\partial t} \cdot \frac{\partial \mathbf{R}}{\partial t} \right) dt^2 \quad (11)$$

so that Equation (7) reduces to

$$K_n = \frac{e(ds)^2 + 2f(ds)(dt) + g(dt)^2}{E(ds)^2 + 2F(ds)(dt) + G(dt)^2} \quad (12)$$

where

$$E = \frac{\partial \mathbf{R}}{\partial s} \cdot \frac{\partial \mathbf{R}}{\partial s} \quad (13)$$

$$F = \frac{\partial R}{\partial s} \cdot \frac{\partial R}{\partial t} \tag{14}$$

$$G = \frac{\partial R}{\partial t} \cdot \frac{\partial R}{\partial t} \tag{15}$$

The denominator of Equation (12) is called the first fundamental form of the surface, and the numerator of Equation (12) is called the second fundamental form of the surface. From Equation (12), we obtain the relation

$$\frac{1}{2} (K_n E - e) ds^2 + (K_n F - f) ds dt + \frac{1}{2} (K_n G - g) dt^2 = 0 .$$

Consider Equation (16) as a quadratic equation in ds and fix K_n at some value. Depending upon the value of K_n , Equation (16) has

- (a) no real roots,
- or (b) one multiple root
- or (c) two distinct real roots.

The discriminant of Equation (16) is

$$(K_n F - f)^2 - (K_n E - e)(K_n G - g) \tag{17}$$

If K_n is chosen so that this discriminant is zero, i.e., if K_n assumes one of the two values

$$K_n^\pm = \frac{-(eG + gE - 2fF) \pm \sqrt{(eG + gE - 2fF)^2 - 4(F^2 - EG)(f^2 - eg)}}{2(F^2 - EG)} , \tag{18}$$

condition (b) is satisfied and Equation (16) has a multiple real root. The direction (ds, dt) obtained by solving Equation (16) for K_n^+ is called a principal direction of normal curvature and is the only direction with unique normal curvature K_n^+ . Similarly, there is a principal direction corresponding to K_n^- (which, in general, does not agree with the K_n^+ direction). Since the roots of Equation (16) are continuous functions of K_n , K_n^+ and K_n^- are, respectively, the maximum and minimum values for the normal curvature of the surface at the point (s_0, t_0) in the direction (ds, dt) . An interesting result of the theory is that

for surfaces that locally are not spheres or planes at (s_0, t_0) , the two principal directions are orthogonal.^{1,2}

Having derived a formula for the maximum normal curvature at any surface point, the only remaining problem is to determine the maximum of this function over the entire surface. Since Equation (18) gives an explicit formula for the normal curvature in terms of s and t , any one of several well-known techniques can be used to maximize this function. For example, a two-dimensional Newton scheme should prove effective here.

IMPLEMENTATION IN THE FMILL SYSTEM

FMILL is a computer program that can be used in conjunction with the APT (Automatically Programmed Tool) system to produce a control tape for a numerical control tool. It will accept a mesh of points in 3-space as input and will fit a parametric surface through these points with a degree of smoothness dependent on tolerances specified by the user. The radius of curvature computations have been implemented successfully in the FMILL program by M. E. White and G. E. Blake.³ Their algorithm samples the radius of curvature on a mesh of points whose size is approximately that of the input mesh. Several test surfaces showed that the minimum radius found by this technique was within 5% of the theoretical minimum, provided the input mesh was reasonably fine.

¹L. P. Eisenhart, *Introduction to Differential Geometry*, Princeton University Press, 1940, p. 225.

²H. Lass, *Vector and Tensor Analysis*, McGraw-Hill Book Co., 1950, pp. 77-80.

³M. E. White, private communication.

MULTISPECTRAL VIDICON CAMERA STUDY

By

J. J. DISHLER* AND D. F. LONGCOY

RCA Astro-Electronics Division
Princeton, N. J.

Summary—Multispectral observation of earth and cloud cover via satellite has been accomplished in the past by using vidicon sensors in the visible spectral region and cell scanners in the infrared regions. Available information to date shows that neither sensor has been effective in the near-infrared range from 0.7 to 1.0 micron. A study was conducted to evaluate, in this region, the vidicon sensor surfaces presently used in the AVCS/TOS meteorological satellite. This paper presents the measured results of both the vidicon and the system.

Experimental findings indicate that the near-infrared sensitivity of this sensor is effective in the region from 0.7 to 0.85 micron. The results are presented first as vidicon data obtained by techniques prescribed by the IRIS Image Forming Sensors Specialty Group. Secondly, kinescope recordings of the television system are used to present data on the multispectral mode of chlorophyll detection and identification. Thus, this study shows both the quantitative and qualitative feasibility of using standard (ASOS)† slow-scan vidicon surfaces in the near-infrared spectral region.

INTRODUCTION

THE phrase "remote sensing of environment" has been applied by earth scientists, geographers, oceanographers, meteorologists, agriculturists, ecologists, geologists, and space scientists to their use of imaging information obtained from high-altitude aircraft or space vehicles. An important method of identifying objects or regions of significance is to compare multiple recorded images of the identical scene taken through different restricted bands of the electromagnetic spectrum. By knowing the characteristic reflectivity of a certain object in the multiplicity of bands it is possible to differentiate vegetation from bare soil, wet from arid areas, etc. Multispectral camera systems employing photographic film have been under evaluation for a number of years. The development of a multispectral television camera complex is a logical step for extending this capability to a satellite sensing system.

An important portion of the electromagnetic spectrum for this application lies in the region between 0.7 and 1.0 micron (7,000 and 10,000 Å). Camera-tube photosurfaces of useful efficiency for slow-scan operation have not been available for this portion of the spectrum. This paper reports the assessment of an available vidicon tube for use in this wavelength band.

* Now with RCA Graphic Systems Division, Dayton, N. J.

† Antimony sulfide oxysulfide.

EVALUATION OF THE VIDICONS

Selected for evaluation were three one-inch vidicons of the variety used for the Advanced Vidicon Camera System/Tiros Operational Satellite (AVCS/TOS). These particular vidicons possess the standard antimony trisulfide oxysulfide (ASOS) sensing layer. Of these three vidicons, all had their target surfaces processed in the standard production manner. Testing of the tubes was performed in accordance with the methods and techniques prescribed by the Infrared Information Symposium (IRIS).¹

All the vidicons were measured for their spectral response characteristics in the visible and near-infrared regions, ranging from 0.4 to 1.3 microns. More specifically, the tests were carried out using a tungsten source corrected to 2817°K (equivalent black-body temperature). A Schneider xenon lens was used to image the source on the sensing layer in such a manner that the vidicon area irradiated was at least 10% of the total horizontal raster dimension. Used in conjunction with the source were various spectral band-pass interference filters having approximately 10% bandwidths at the 50% transmission points.

The total irradiance (H_s) on the vidicon was calculated by computer from Planck's black-body radiation law using appropriate correction factors for the physical parameters of the system:

$$H_s = \frac{3.74 \times 10^{-12}}{4f^2 + 1} \int_{\lambda_1}^{\lambda_2} \lambda^{-5} (e^{1.438/(\lambda T)} - 1)^{-1} T_1(\lambda) T_2(\lambda) E(\lambda) d\lambda \quad (1)$$

where

H_s = the incident irradiance in watts/cm²

λ_1 & λ_2 = the 50% bandwidth wavelengths

T = source temperature in °K

$T_1(\lambda)$ = lens transmission factor

$T_2(\lambda)$ = filter transmission factor

$E(\lambda)$ = emissivity factor of the light source

f = lens aperture

¹ IRIS Proceedings, August 1963, Volume 8.

Testing was conducted by selecting convenient wavelengths, i.e., 0.400, 0.500, 0.600 micron, etc., and using spectral filters to limit the bandwidths at each of these points. Then, for each of these specific wavelengths, the lens aperture was varied from $f/2.0$ to $f/22$. For each aperture position, the signal-to-noise ratio (S/N) was measured and plotted against the irradiance, H_s . The result was a family of curves, S/N versus H_s , with spectral wavelength as the parameter. From this family of curves, the irradiance for which the S/N ratio becomes unity is defined as the Noise Equivalent Irradiance (NEH). Using the preceding data, one final curve was plotted; a curve $1/NEH$ versus wavelength (λ). This, in effect, is the spectral-response curve of the vidicons (especially No. Z20078) do appear to have some usable of irradiance required to produce a signal equal to the noise at that wavelength. Relevant data points for all the vidicons are given in Table I.

Table I—Response of the Three Vidicons.

Tube No.	Response at 0.700 micron (% of Max.)	Response at 1.00 micron (% of Max.)	Wavelength at 10% response
Z 20048	31	0.02	0.760 μ
Z 20077	27	0.01	0.750 μ
Z 20078	38	0.02	0.820 μ

For the purposes of this study, the near-infrared region ranging from 0.700 to 1.000 micron was the main consideration. Arbitrarily, the 10% response point was chosen as a comparison point for minimum usable response. As can be seen from Table I, this 10% point varies from 0.750 micron on tube No. Z20077 to 0.820 micron on tube No. Z20078. However, in spite of the variation in the tubes measured, all of the vidicons (especially No. Z20078) do appear to have some usable near-infrared sensitivity. The spectral response of vidicon No. Z20078 is shown in Figure 1.

SLOW-SCAN IR SYSTEM TESTS

On the basis of the above data, vidicon No. Z20078 was selected for further experimentation. Also chosen for the testing was a slow-scan television system of the AVCS variety with the following operating parameters:

Operating Parameters of Test System

Vidicon	one-inch storage type, ASOS surface, No. Z20078
Deflection	electromagnetic
Focus	electromagnetic
Horizontal Rate	7.5 milliseconds, 10% sync
Vertical Rate	6.5 seconds
Video Chain 3-dB bandwidth	60 kHz
Operation	shuttered, 250-millisecond, double- bladed, focal-plane shutter
Lens	17 mm, f/4

A special scene was constructed for this slow-scan system test. Included was a nine-step gray scale, a white magnesium oxide block, and two green leaves. One of the leaves was from an artificial plastic plant, and the other from a living, potted plant. All of the items were attached to a flat black background.

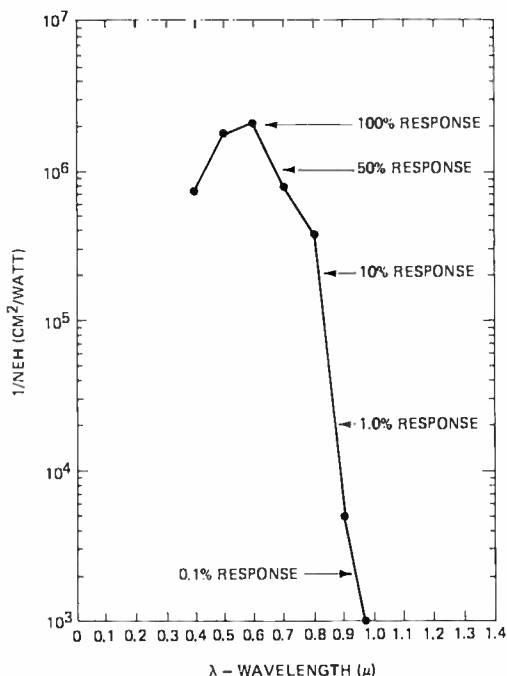


Fig. 1—Spectral response of Vidicon No. Z20078.

Illumination for the scene was provided by a "Sun Gun"† in conjunction with a daylight filter. Hence, the approximate spectral distribution of the source was that of a black-body radiator at 5500°K. Each item in the test scene was measured by a spectra spotmeter that was corrected to read on the standard luminosity curve. Under the previously specified conditions, visible illumination varied from 1200 foot-lamberts on the MgO block to 25 foot-lamberts on the black background. Both of the green leaves (real and artificial) were approximately matched in reflectance (120 foot-lamberts and 110 foot-lamberts, respectively).

The slow-scan camera system was then used to take pictures of the test scene, recording data by two methods. Qualitative data was measured by taking Polaroid pictures from a monitor display; quantitative measurements were made by taking Polaroid pictures from a line-selecting oscilloscope. (The single horizontal data line selected included both of the leaves and objects of peak-black and peak-white reflectance.) Responses of objects other than black or white were then measured and expressed as a percentage of the black-to-white transition of the video. Under these conditions, the real leaf measured 16% relative response and the plastic leaf measured 10% response when presented to the vidicon through a 1.5 neutral-density filter.

Testing was then performed by placing the various Corning "Sharp-Cut"* (high-pass) filters in front of the lens and recording the relative responses of the two leaves compared to the black-to-white transition. In each case, a selected neutral-density filter was used in conjunction with the spectral filter to keep the peak black-to-white video transition constant. In this way, the measurements were normalized by reducing the maximum transmission of each spectral filter to that of the most dense spectral filter. Table II presents data for some of the filters used.

As can be seen from Table II, the response of the plastic leaf remained relatively constant as more and more of the visible region was excluded, while the response of the real leaf constantly increased. The same effect was also clearly seen in the monitor display. As more and more of the visible wavelengths were excluded, the real leaf became whiter and whiter.

To provide additional data, testing was now performed in a manner more directly applicable to a multi-spectral television system. Two Corning band-pass filters were selected instead of the high-pass filters

† Sylvania Corp.,
* Corning Glass Co.

previously described: filter No. CS-4-105, a green band-pass filter with a peak at 0.510 micron and 10% points at 0.495 and 0.530 micron; and filter No. CS-2-113, a slightly wider band-pass filter centered at 0.71 micron with 10% points at 0.690 and 0.750 micron. As before, differences in neutral density of the filters were corrected by using additional neutral-density filters. The results of this test indicated that both leaves (real and artificial) in both spectral bandwidths had approximately the same response. There was almost no perceptible difference between them.

Table II—Filter Data

Filter Type No.	Filter (10% Trans. Pt.) (Microns)	Filter (90% Trans. Pt.) (Microns)	Black-to- White (Volts)	Real Leaf (% Response)	Plastic Leaf (% Response)
1.5 ND	—	—	4.72	16.8	9.5
Corning CS-2-58	0.632	0.678	4.50	31.6	14.3
Corning CS-2-62	0.599	0.633	4.52	33.7	13.2
Corning CS-2-64	0.658	0.720	4.53	38.3	14.0
Corning CS-7-69*	0.725 1.06	0.825	4.61	79.4	16.5

* IR band-pass filter.

From these results, we concluded that the differences recorded previously by using the "Sharp Cut" (high-pass) filter series was due mainly to the extended infrared transmissions of those filters. We therefore substituted for the CS-2-113 infrared band-pass filter various other infrared filters having transmission peaks farther out in the infrared region. It was found that as the band-pass center was moved progressively out, increased contrast differences could be seen between the two leaves. Furthermore, a maximum difference could be measured when the infrared band-pass filter had its peak occurring at approximately 0.830 micron.

A filter such as the Corning CS-7-69 has these approximate characteristics. It is an infrared band-pass filter with peak transmission at 0.825 micron and 10% points at 0.725 and 1.060 microns. A comparison of the results obtained with this filter as the upper band pass and the CS-4-105 as the visible region band pass is given in Table III. Measurements were performed on a line-selecting oscilloscope.

As can be seen, the relative percent response of the two leaves is the same with the green band-pass filter; however, the real leaf gives

Table III—Infrared-Band-Pass Filter Data

Filter	10% Transmission (Micron)	Peak Transmission (Micron)	Black-to- White (%)	Plastic Leaf (% Response)	Real Leaf (% Response)
CS-4-105 (Green)	0.490 0.530	0.510	100	5.4	5.4
CS-7-69 (IR)	0.725 1.06	0.825	100	10.0	55.3

approximately 5.5 times more response with the IR band-pass filter. This fact is even more dramatically emphasized by the two monitor photos included. In Figure 2(a), taken using the green band-pass filter, both leaves are approximately the same shade of grey. In Figure 2(b), taken with the infrared band-pass filter, the plastic leaf is still grey, but the real leaf is white. Thus, here presented is a practical application of the near-infrared sensitivity of ASOS-surface vidicons in a slow-scan, multispectral system.

CORRELATION OF DATA

Although the bulk of this study was experimental in nature, an attempt was made to correlate the experimental and theoretical data. The basic premise of this correlation is that the "white" signal output of the vidicon (i.e., the output obtained when only the white background is observed by the camera) is due to the presence of irradiation on the

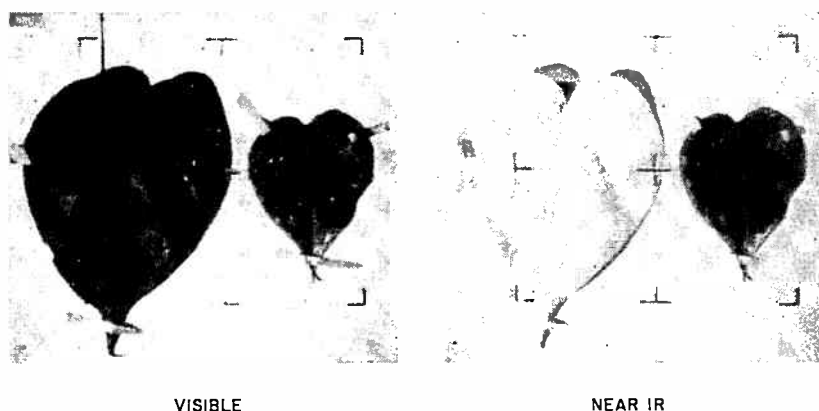


Fig. 2—Monitor photo of real (left) and plastic leaves (a) using green band-pass filter and (b) using infrared band-pass filter.

face plate. Furthermore, this white signal is due to the presence of all wavelengths of radiant energy within the specified optical bandwidth. Since the total black-to-white signal output of the camera system was held constant for the tests performed, it was surmised that the total white energy was the same in each case.

It is known that if a source of radiant energy has any arbitrary spectral characteristics, the total energy emitted is proportional to the area under its spectral distribution curve:

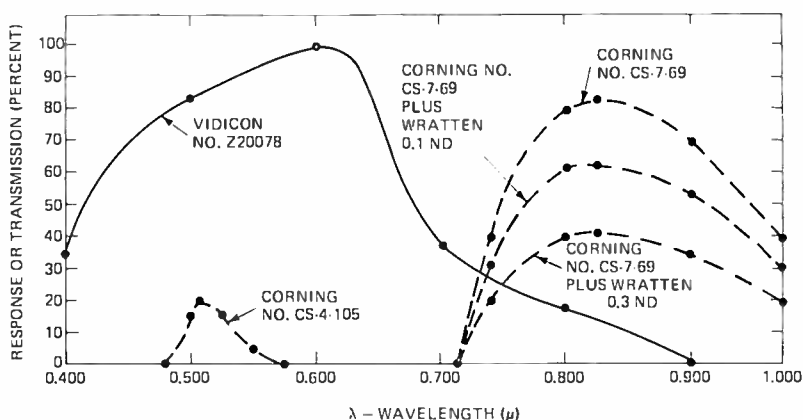


Fig. 3—Spectral response of filters and vidicon used in test.

$$E = K \int_{\lambda_1}^{\lambda_2} E(\lambda) d\lambda, \quad (2)$$

where $E(\lambda)$ is spectral distribution of energy and K is constant of proportionality.

In the process of converting this energy to a video signal, the total energy curve is modified by the system parameters (lens transmission, filter transmission, vidicon response, etc.). In general, these factors are all functions of wavelength. Hence, the total energy converted to a signal is of the form:

$$E_{\text{Total}} = K \int_{\lambda_1}^{\lambda_2} E(\lambda) T_1(\lambda) T_2(\lambda) R(\lambda) d\lambda \quad (3)$$

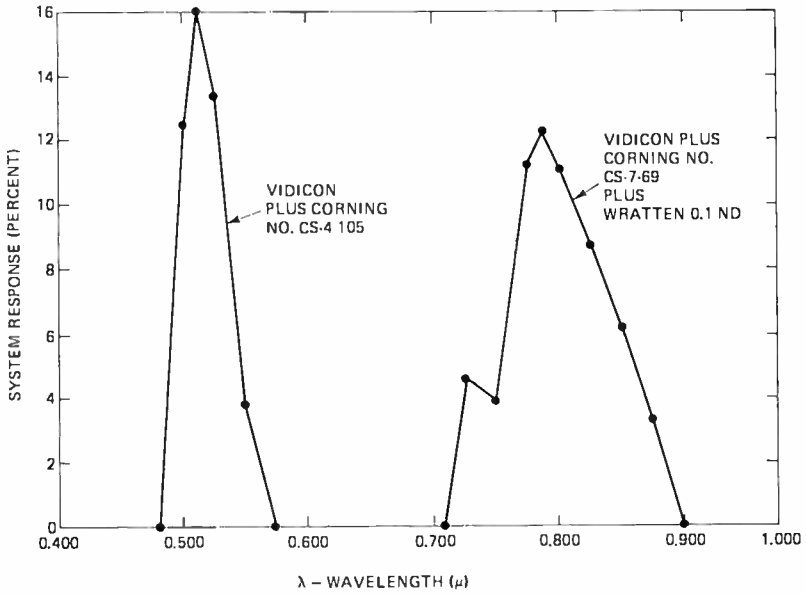


Fig. 4—Composite spectral response of vidicon and optical filters.

In essence, the method of approach was to show that the total spectral energy converted to the video signal was approximately the same for both spectral bandwidths. Since the transmission functions are too complex for convenient analytical integrations, the integration was done graphically as shown in Figures 3 through 6. The factors

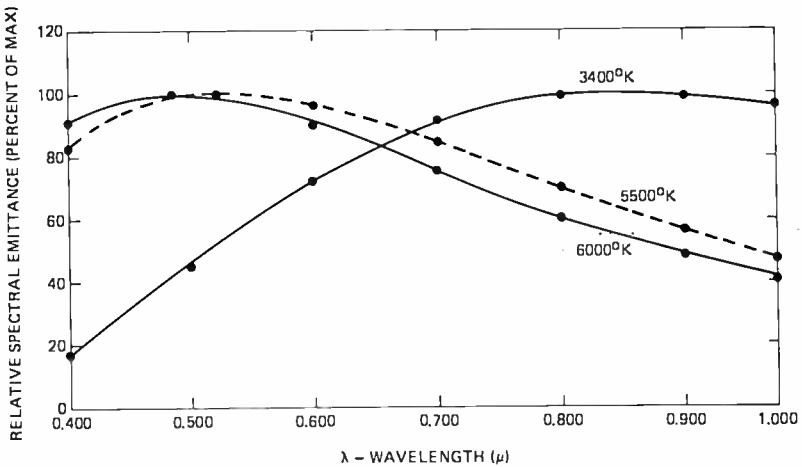


Fig. 5—Black-body radiation at 3400, 5500, and 6000°K (approximations of light sources used in test).

considered were the light source, the optical filters, and the vidicon response. The net result is shown in Figure 6. Areas under these two curves represent a comparison of the total energy conversion of the camera system for the two spectral bandwidths in question. The two areas shown are within 12% of each other; hence, it appears that the measurements taken and the results obtained are reasonable.

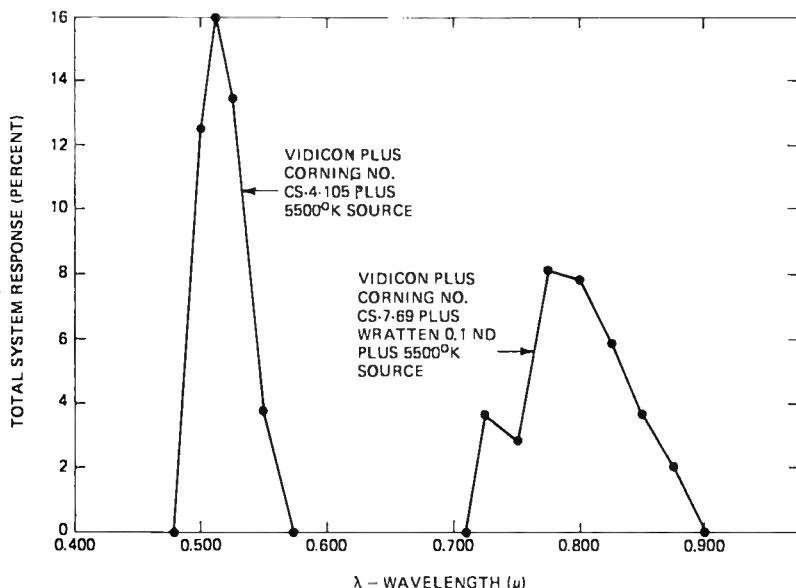


Fig. 6—Composite spectral response of system for the two regions under consideration (vidicon with optical filters and 5500°K source).

CONCLUSION

This preliminary study has shown that selected ASOS vidicons do have sufficient sensitivity to be useful in the near-infrared spectral region from 0.7 to 0.85 micron. Future possibilities for investigation may include such things as development of ASOS surfaces with extended capabilities in the near-infrared region. Also, some of the tests conducted in this study could be performed again outdoors to determine the advantages and/or limitations of such a system under natural lighting and atmospheric conditions.

Also shown in this study was a practical application of ASOS near-infrared response. Since the object was the detection of chlorophyll, maximum contrast was provided between the visible and infrared bands

by placing the spectral centers at 0.51 and 0.83 micron. However, these two spectral centers can be varied according to the system needs.

For future experimentation, the use of ASOS vidicons as spectral sensors could be extended by using four spectral regions (red, green, blue, and IR) to produce color pictures. In this way, the use of these sensors in a true multi-spectral system would be demonstrated.

ACKNOWLEDMENT

Tests to determine spectral response of the vidicon tube were performed by F. D. Marschka, RCA Electronic Components, Lancaster, Pa.

RCA Technical Papers

First Quarter, 1968

Any request for copies of papers listed herein should be addressed to the publication to which credited.

- "Electrical and Optical Properties of GaAs Injection Lasers with Closely Compensated p-Type Region," H. Kressel and F. Z. Hawrylo, *Jour. Appl. Phys.* (January) 1968
- "Electrical Behavior of Copper-Diffused Insulating Layers on CdS Crystals," M. Simhony, R. Williams, and A. Willis, *Jour. Appl. Phys.* (January) 1968
- "A Gyro-Medium Filled Beam Waveguide," W. H. Schaedla and Co-author, *IEEE Trans. AP* (January) 1968
- "Impact Ionization and Charge Transport in GaAs:GaP 50% Alloy," R. Williams, *Jour. Appl. Phys.* (January) 1968
- "Monolithic Linear Integrated Circuits—Yesterday... Today... and Tomorrow...," M. V. Hoover, *Signal* (January) 1968
- "Corrections to 'Precision Measurement of the Microwave Dielectric Constant of Liquids'," P. R. Mason and E. Fatuzzo, *Jour. Appl. Phys.* (Communications) (January) 1968
- "Rejection of Multipath Interference in Satellite Communications by Use of Narrow-Band Filters," S. H. Durrani, *IEEE Trans. AES* (Correspondence) (January) 1968
- "Symmetry Types in Threshold Logic," R. O. Winder, *IEEE Trans. C* (Short Notes) (January) 1968
- "Theory of Nuclear Hyperfine Interactions in Spherical-Top Molecules," C. H. Anderson and Coauthors, *Phys. Rev.* (5 January) 1968
- "Depairing Effect of a Magnetic Field: A Study of Microwave Absorption in the Surface-Sheath Regime of Pure Lead," G. Fischer and R. Klein, *Phys. Rev.* (10 January) 1968
- "Hall Mobility of the Small Polaron. II," L. Friedman and Co-author, *Phys. Rev.* (15 January) 1968
- "Surface Impedance near the Cyclotron Edge for Helicons in Potassium," R. C. Alig, *Phys. Rev.* (15 January) 1968
- "Color Television Standards for Region 2," C. J. Hirsch, *IEEE Spectrum* (February) 1968
- "Critical-Point Behavior of the Susceptibility of Classical Heisenberg Ferrimagnets," S. Freeman and P. J. Wojtowicz, *Jour. Appl. Phys.*, Part I (February) 1968
- "Discussion of Some Flaws in the Classical Theory of Two-Level Minimization of Multiple-Output Switching Networks," T. F. Dwyer and Coauthor, *IEEE Trans. C* (Short Notes) (February) 1968
- "Epitaxial Growth of Metal Oxides," J. J. Hanak and D. Johnson, *Jour. Appl. Phys.*, Part II (February) 1968
- "Ferromagnetic Halo-Chalcogenide Spinel ($\text{CuCr}_2\text{X}_4\text{Y}$) and Some Properties of the Systems $\text{CuCr}_2\text{Se}_4\text{Br}$ - CuCr_2Se_4 and $\text{CuCr}_2\text{Te}_4\text{I}$ - CuCr_2Te_4 ," M. Robbins, P. K. Baltzer, and E. Lopatin, *Jour. Appl. Phys.*, Part I (February) 1968

- "Large-Signal Behavior of Distributed Klystrons," C. Sun and Coauthor, *IEEE Trans. ED* (February) 1968
- "Magnetic and Crystallographic Properties of the System $MnCr_2S_4$," L. Darcy, P. K. Baltzer, and E. Lopatin, *Jour. Appl. Phys.*, Part II (February) 1968
- "Microwave Solid-State Power Sources," F. Sterzer, *Microwave Jour.* (February) 1968
- "Neutron-Diffraction of the Ferromagnetic Mixed-Anion Spinel $CuCr_2Se_3Br$," M. Robbins and Coauthor, *Jour. Appl. Phys.*, Part I (February) 1968
- "NMR of ^{53}Cr and ^{77}Se in Ferromagnetic Chalcogenide Spinel," S. B. Berger and Coauthors, *Jour. Appl. Phys.*, Part I (February) 1968
- "Strain-Sensitive Thin Magnetic Films," L. S. Onyshkevych, *Jour. Appl. Phys.*, Part II (February) 1968
- "Testers for IC's," F. J. Ward, *The Electronic Engineer* (EE Speak Up) (February) 1968
- "Surface Nucleation Field H_{cs} of Pure Lead," G. Fischer, *Phys. Rev. Letters* (5 February) 1968
- "Specific Heat of Niobium-Tin," L. J. Vieland and A. W. Wicklund, *Phys. Rev.* (10 February) 1968
- "A Worthy Challenger for R-F Power Honors," D. R. Carley, *Electronics* (February 19) 1968
- "'Butterfly' VHF Panel Antenna," D. A. Brawn and B. K. Kellom, *Broadcast News* (March) 1968
- "Duc de Chaulnes' Method for Refractive-Index Determination," A. Miller, *Jour. Opt. Soc. Amer.* (Letters to the Editor) (March) 1968
- "Electroluminescent Source with Luminance Greater than 6×10^9 cd/m^2 ," J. I. Pankove and I. J. Hegyi, *Proc. IEEE* (Letters) (March) 1968
- "Experimental Impedance of a Quarter-Wave Monopole in an Isotropic Plasma," D. L. Jassby, *IEEE Trans. AP* (Communications) (March) 1968
- "Fading from Irregular Surfaces for Line-of-Sight Communications," A. B. Glenn, *IEEE Trans. AES* (March) 1968
- "Improved Ferroelectric Field-Effect Devices," J. H. McCusker and S. S. Perlman, *IEEE Trans. ED* (Correspondence) (March) 1968
- "Luminescence in Silicon-Doped GaAs Grown by Liquid-Phase Epitaxy," H. Kressel, J. U. Dunse, H. Nelson, and F. Z. Hawrylo, *Jour. Appl. Phys.* (March) 1968
- "A Maser Saturation Protection Switch," B. R. Feingold, *Proc. IEEE* (Letters) (March) 1968
- "Multipath Problems in Communications between Low-Altitude Spacecraft and Stationary Satellites," S. H. Durrani and H. Staras, *RCA Review* (March) 1968
- "A New Type of Latching Switchable Ferrite Junction Circulator," W. W. Siekanowicz and W. A. Schilling, *IEEE Trans. MTT* (March) 1968
- "A Note on Resistor Temperature Gradients in High Reliability Cordwood Packaging," E. Veilleux and Coauthor, *IEEE Trans. PMP* (Correspondence) (March) 1968
- "Optical Properties of As_2Se_3 , $(As,Sb_{1-x})_2Se_3$, and Sb_2S_3 ," A. Efsthathiou and E. R. Levin, *Jour. Opt. Soc. Amer.* (March) 1968
- "The Physics of Failure of MIS Devices Under Radiation," A. G. Holmes-Siedle and K. H. Zaininger, *IEEE Trans. R* (March) 1968
- "Power Dissipations Limits in Solid-State Oscillator Diodes," A. S. Clorfeine, *Microwave Jour.* (March) 1968
- "Probability Distribution of Time to Phase Lock for a Second-Order Phase-Locked Loop," F. S. Keblawi, *RCA Review* (March) .. 1968
- "Quadrature Detection PSK System and Interference," V. F. Volertas, *RCA Review* (March) 1968

"Return-Beam Vidicon System Achieves 5000 TV Lines Resolution," <i>Broadcast News</i> (March)	1968
"Self and Mutual Inductances of Superconducting Structures," A. R. Sass and W. C. Stewart, <i>Jour. Appl. Phys.</i> (March)	1968
"The Si-SiO ₂ Solid-Solid Interface System," A. G. Revesz and K. H. Zaininger, <i>RCA Review</i> (March)	1968
"A Solid-State Low-Noise Preamplifier and Picture-Tube Drive Am- plifier for a 60-MHz Video System," O. H. Schade, Sr., <i>RCA</i> <i>Review</i> (March)	1968
"Technical Highlights of the 1968 IEEE Convention," E. W. Herold and Coauthor, <i>IEEE Spectrum</i> (March)	1968
"Lighting up in a Group," L. A. Murray, S. Caplan, and R. Klein, <i>Electronics</i> (March 4)	1968
"Semiconductor Gages Make Sense in Most Transducer Applications," R. M. Moore, <i>Electronics</i> (March 18)	1968
"Thin-Film Transistors Don't Have to Be Drifters," A. Waxman, <i>Electronics</i> (March 18)	1968

AUTHORS



JULES J. DISHLER received a BSEE and an MSEE degree from Drexel Institute in 1954 and 1963, respectively. Since joining RCA in 1950, he has been primarily concerned with the research and development of special television tubes, associated electronic circuitry, and various television systems for space programs. From 1950 to 1957 he was with the RCA Surface Communications Division. From 1957 to 1960, he was with the Aerospace Communications and Control Division of RCA where, as an Engineering Leader, he was involved in the design and development of input/output data-conversion devices, the fiber optic line scan-converter television camera, and other television experimental and design programs. From 1960 to 1965, he was with the RCA Defense Communications Systems Division, responsible for the project management of the development of microwave relay equipment, custom television systems, and digital high-density magnetic-tape recorders. He joined the Astro-Electronics Division in 1965 as Engineering Leader, Television Camera Systems, Spacecraft Electronics, where he has been involved in an evaluation program of multispectral video sensors for graphic-material scanner equipment, high-resolution sensors, and meteorological camera systems. Presently he is a member of the RCA Graphic Systems Division. He is a registered Professional Engineer of New Jersey, a member of I.E.E.E. and SMPTE.

JOHN T. FRANKLE received the BSEE degree from the Massachusetts Institute of Technology in June 1958 and the MSEE degree from the Polytechnic Institute of Brooklyn in June 1962. In the summer of 1957 he worked as a Junior Engineer in the Electronics Division of Curtiss-Wright Corporation on the development of an airborne radar simulator. He was appointed a Teaching Fellow at the Polytechnic Institute of Brooklyn in 1958 and a Graduate Research Assistant at the Microwave Research Institute (M.R.I.) of the Polytechnic in 1959. While there, he performed basic research in FM and FM noise. Mr. Frankle joined RCA's Communications Systems Division in 1960 where he has been involved in many diverse programs. Among these are studies of the spectra and extraction of timing information from random digital signals, the RCA Diphase Data Modem, and FM threshold improvement techniques.



Mr. Frankle is a member of the Institute of Electrical and Electronic Engineers.



IRWIN GORDON received the B.S. degree in Ceramics from Rutgers University in 1948, the M.S. degree in 1951, and the Ph.D. degree in 1952 from the same institution. From 1948 to 1952 he held a research assistantship in the School of Ceramics at Rutgers University, working on single crystal synthesis and studies of various silicates and rare earth aluminates. In 1952 Dr. Gordon joined the technical staff of RCA Laboratories where he has worked on the development of magnetic materials for various applications. This has included materials for permanent magnets, multi-function composite materials,

recording tape pigments, small size HF antennas, and nonspinel type magnetic materials for use in the VHF and UHF regions. Most recently he has investigated ferrites for use in laminated computer memories, as well as ferrites for microwave use.

Dr. Gordon is a member of the American Ceramic Society, the N. J. Ceramic Association, Sigma Xi, Keramos, and of the A.S.T.M.

R. L. HARVEY received the B.S. in E.E. from the University of Tennessee in 1928. He has been with RCA since 1930, joining the research staff of RCA Laboratories in 1942. Mr. Harvey has over 25 years experience in magnetic materials for use at radio frequencies, including early work on powdered iron cores and design of the first commercial i-f transformers using cores. He is presently engaged in research on ferrites for application in computers, television, antennas, and high-frequency and microwave devices. His work includes synthesis of the materials, test evaluation, and application of the material to electronic circuitry. Mr. Harvey is a Senior Member of I.E.E.E. and a member of Sigma Xi.



HENRY N. HEINEMANN received the BEE degree from City College of New York in 1962, and is currently enrolled in the graduate program at CCNY pursuing the M.E.E. In 1962, he joined the Western Union Telegraph Company, Facsimile Division, where he worked on many phases of the electronic design of a facsimile transceiver, and performed an experimental study of a communication system using quadrature modulation and synchronous-detection techniques with phase-locked receivers. He joined the RCA Defense Communications Systems Division in 1963. He has since been involved primarily in

analysis and design of low-threshold FM demodulators employing feedback. This work has led to the analysis and design of phase-locked demodulators for single-channel receivers, as well as multiple-loop demodulators that represent a significant advance in the state of the art of low-threshold demodulation. Mr. Heinemann is a member of the Institute of Electrical and Electronic Engineers.



EDWARD P. HELPERT received the B.S.E.E. degree in June 1961 from Rutgers University, and the M.S. Eng. degree in June 1963 from Princeton University. He is currently engaged in thesis research for a Ph.D. degree in Mathematics from the Courant Institute of Mathematical Sciences, New York University. Mr. Helpert joined RCA Laboratories in June 1961 and has worked in the areas of pattern recognition and semiconductor device fabrication. He is presently concerned with mathematical problems associated with numerical control.

Mr. Helpert is a member of Tau Beta Pi, Eta Kappa Nu, and the Society for Industrial and Applied Mathematics.



DENNIS F. LONGCOY received the degree of B.S. in Electrical Engineering from the University of Cincinnati in 1966. From 1962 to 1966, he was employed as a student engineer at RCA Defense Electronic Products in Camden and at RCA Astro-Electronics Division in Hightstown. During this period he participated in the design and development of low-level FM altimeters and slow-scan television camera systems such as Tiros, APT, and AVCS. Since becoming an associate engineer at the RCA Space Center, Mr. Longcoy has had the responsibility for design of sync-lock, remote control, and audio

circuitry for the Manpack portable color-television camera. He is presently working on the development of a high-resolution, multispectral, return-beam television camera system for space applications.

HERBERT I. MOSS received the B.S. degree with honors in chemistry in 1953 from the University of Louisville, and was awarded the Ph.D. degree from Indiana University in 1960. From 1953 to 1956 he served as a Teaching Assistant in chemistry, and from 1956 to 1959 he was a Research Assistant in chemistry at Indiana University. In 1959 he joined the staff of RCA Laboratories, and for his first four years he worked on photovoltaic effects in large area thin films. Since 1963, he has specialized in pressure sintering (hot pressing) of electronic, magnetic, and optically active materials. His research has been concerned with such diverse materials as ferrites, calcium fluoride, gallium arsenide, and more recently, lead telluride alloys for thermoelectric applications. This work has also involved the mechanical characterization of the lead telluride materials. Dr. Moss is a member of the American Chemical Society, American Institute of Chemists, Electrochemical Society, American Ceramic Society, American Vacuum Society, Sigma Xi, and is listed in American Men of Science.





ARNOLD NEWTON received a diploma from the Mathematics-Physics Lyceum, Krakow, Poland in 1941, completed the T-3 course at the RCA Institutes, and did graduate work at the City College of New York in 1963. He joined RCA Industry Service Laboratories in 1944, where he worked on circuits for projection-television receivers until 1947. He subsequently held engineering positions with Polytechnic Research and Development Co., FXR and Polarad Electronics Corp. Mr. Newton returned to RCA, Communications Systems Division, in 1958, where he engaged in the study and development of

Electronic Counter Measures systems. He was appointed Group Leader in 1961 with responsibility for several projects that led to the development of FMFB and phase-locked demodulators for 120 and 600 channels, respectively. He was also in charge of the Lunar-Orbiter Ground Station demodulator program, threshold improvement program for tactical radio and tropo sets, and an Advanced ECCM program for the Signal Corps. He is currently in charge of the 600-channel modulator-demodulator program for the Communication Satellite Corp.

Mr. Newton is a Senior Member of the Institute of Electrical and Electronics Engineers and Member of AAAS.

JOHN J. O'NEILL, JR. joined RCA Laboratories, Princeton, New Jersey in 1956. From 1956 to 1962 he worked on the synthesis of III-V compounds. In 1962 he transferred to the Energy Conversion Group at Princeton and was engaged principally in the development of polycrystalline GaAs solar cells. Mr. O'Neill is presently with the Process Research and Development Laboratory where he is working on r-f sputtering. Mr. O'Neill is currently attending Rutgers University, New Brunswick, N. J.



BRUCE B. ROBINSON received his B.S. degree in physics from Drexel Institute of Technology in 1956 and M.A. and Ph.D. degrees from Princeton University in 1958 and 1961, respectively. His doctoral dissertation was in the field of plasma transport theory. He was a research assistant at the University of Chicago and at the University of California where he worked in the areas of plasma transport, plasma stability, and general relativity. Dr. Robinson joined the staff of RCA Laboratories in 1963 and has since that time worked principally in the areas of atomic physics and plasma stability. He is

a member of the American Physical Society.

ANTHONY D. ROBBI received the B.S., M.S., and Ph.D. degrees in Electrical Engineering from the Carnegie Institute of Technology in 1957, 1958, and 1962, respectively. During the academic year 1960-61 he was an Instructor at Carnegie Tech. He joined the Technical Staff of RCA Laboratories in 1961 where he has conducted research in the area of computer magnetics. Dr. Robbi is a member of Sigma Xi, Tau Beta Pi, and Eta Kappa Nu.



C. SUN received the B.S. degree in electrical engineering from National Taiwan University, Taipei, Taiwan in 1958 and the M.S. degree and Ph.D. degree in electrical engineering from Cornell University in 1962 and 1965, respectively. During 1958-1960, he was a ground radar maintenance officer in the Chinese Air Force. Since September, 1964, he has been with the RCA Microwave Applied Research Laboratories in Princeton. He has worked on low-noise traveling-wave tubes, development of varactors, wide-band and high-power varactor multipliers, and optical demodulators. Dr. Sun is a member of Sigma Xi.

R. SHAHBENDER received the B.E.E. degree from Cairo University, Cairo, Egypt, in 1946, the M.S. degree in Electrical Engineering from Washington University, St. Louis, Mo., in 1949, and the Ph.D. degree in Electrical Engineering from the University of Illinois in 1951. After completing his undergraduate studies, Dr. Shahbender joined the Anglo-Egyptian Oilfields, Ltd. for a period of two years and did work in geophysical oil exploration. In 1951 he joined the staff of Honeywell, Brown Instruments Division, and conducted research in the behavior of nonlinear control systems. In 1955, Dr. Shahbender joined RCA in Camden, N. J., and worked in the areas of adaptive systems, nonlinear filters, electron-beam devices, ultrasonic devices and airborne fire control systems. Dr. Shahbender transferred to RCA Laboratories, Princeton, N. J., in 1959 and has been active in the area of high-speed digital memory systems. He is presently head of the digital devices research group in the Data Processing Research Laboratory. Dr. Shahbender is a Senior member of the I.E.E.E. and a member of the Societies of Sigma Xi, and Eta Kappa Nu.





JAMES W. TUSKA received the B.S. degree in Electrical Engineering from the University of Pennsylvania, Philadelphia, Pa. in 1956. During this period he was a summer trainee at the RCA Laboratories, where he worked with industrial color television and photographic simulation as a means of television bandwidth reduction. After graduation, he joined Electro-Mechanical Research, Inc., where he was engaged in the development of FM telemetry devices, and later joined Data Control Systems, Inc., working in the same field. Since 1959 he has been with the RCA Laboratories as a Member of the Technical Staff, and has been engaged in research on diode memory switching circuits, permalloy magnetic sheet memories, the application of MOS transistor circuits to large capacity laminated-ferrite memories, and, most recently, high speed laminated-ferrite memory research.

and has been engaged in research on diode memory switching circuits, permalloy magnetic sheet memories, the application of MOS transistor circuits to large capacity laminated-ferrite memories, and, most recently, high speed laminated-ferrite memory research.

J. L. VOSSEN joined RCA in 1958 after receiving a B.S. in Physics from St. Joseph's College. He was first associated with the Microelectronics Department of what is now RCA Electronic Components in Somerville, New Jersey. At Somerville his work centered on thick and thin-film passive component processes. In 1962 Mr. Vossen transferred to the Advanced Communications Laboratory of the Defense Communications Systems Division in New York City where he conducted research on precision thin-film resistors and capacitors. In 1965 he joined the Process Research and Development Laboratory of the RCA Laboratories where he has been engaged in process research on sputtering processes. Mr. Vossen is a member of the American Physical Society, the American Vacuum Society and the Electrochemical Society.



B. VURAL obtained the Electrical Engineering degree in 1949 and the Dr. of Technical Sciences degree in 1952 from the Swiss Federal Institute of Technology, Zurich, Switzerland. From 1951 to 1953 he was associated with Brown Boveri and Company, Baden, Switzerland, working on microwave relay communication and on application of a special magnetron as communication transmitter. From 1953 to 1959 he was mainly associated with the Electronic Equipment and Tube Department of Canadian General Electric, Toronto, Ontario, Canada, working mainly on microwave problems in connection

with radar and communication. Dr. Vural joined RCA Laboratories as a Member of the Technical Staff in 1959, where he engaged in research related to microwave tubes and later to solid-state physics. He is now with the Department of Electrical Engineering, the City College of the City University of New York, New York.

Dr. Vural is a Senior Member of I.E.E.E. and a member of the American Physical Society.



J. TORKEL WALLMARK received the degrees of Civilingenjör in electrical engineering in 1944, Teknologie Licentiat in 1947, and Teknologie Doktor in 1953, from the Royal Institute of Technology, Stockholm, Sweden. From 1944 to 1945 he was a vacuum-tube Designer for the A. B. Standard Radiofabrik, Stockholm. He was with the Royal Institute of Technology as a Research Assistant on vacuum-tube problems from 1945 to 1953. At the same time he spent periods at the RCA Laboratories in Princeton, N. J., and at Elektrovärmeinstitutet and Tekniska Forskningsradet, both in Stockholm, engaged in work

on secondary emission tubes, semiconductors, and research administration. In 1953 he joined RCA Laboratories, Princeton, N. J., where he has been engaged in research on magnetrons, color television, semiconductor devices, and integrated electronics. After two years as a professor at Chalmers University in Gothenburg, Sweden, 1963-1966, he is now working on semiconductor devices in memories.

CHANDLER WENTWORTH received a B.S. degree from the Massachusetts Institute of Technology in 1936. He has been with RCA since that time. His work has been in the fields of i-f and audio circuits, plastics, powder metallurgy, ceramic dielectrics, and magnetic ceramics.













RCA REVIEW is regularly abstracted and indexed by *Abstracts of Photographic Science and Engineering Literature*, *Applied Science and Technology Index*, *Bulletin Signalétique des Télécommunications*, *Chemical Abstracts*, *Electronic and Radio Engineer*, *Mathematical Reviews*, and *Science Abstracts* (I.E.E.-Brit.).

The first part of the document discusses the importance of maintaining accurate records of all transactions. It emphasizes that every entry, no matter how small, should be recorded to ensure the integrity of the financial statements. This includes not only sales and purchases but also expenses and income. The text suggests that a systematic approach to record-keeping is essential for identifying trends and making informed decisions.

In the second section, the author addresses the common challenge of reconciling bank statements with the company's ledger. It provides a step-by-step guide to identify discrepancies, such as timing differences or errors in recording. The importance of regular reconciliation is highlighted to prevent small errors from accumulating and causing significant issues at the end of the year.

The third part of the document focuses on budgeting and cost control. It explains how a well-defined budget can serve as a roadmap for the business, helping to allocate resources effectively and avoid overspending. The text offers practical tips for monitoring actual performance against the budget and adjusting as needed to stay on track.

Finally, the document concludes with a section on tax compliance. It stresses the need to understand the current tax laws and regulations that apply to the business. Keeping up-to-date with tax changes is crucial to avoid penalties and ensure that the business is maximizing its tax efficiency. The author encourages consulting with a professional tax advisor for complex situations.